

NASA
TT
F-382
c.1

Akademiya Nauk Ukrainskoi SSR

LOC. 11 COPY 11 RETURN TO
AFWL (WU11-2)
KIRTLAND AFB, N MEX

PHYSICS OF THE MOON AND THE PLANETS

0068785



TECH LIBRARY KAFB, NM

Translated from Russian

Published for the National Aeronautics and Space Administration, U.S.A.
and the National Science Foundation, Washington, D.C.
by the Israel Program for Scientific Translations



AKADEMIYA NAUK UKRAINSKOI SSR. GLAVNAYA ASTRONOMICHESKAYA
OBSERVATORIYA

Academy of Sciences of the Ukrainian SSR. Main Astronomical Observatory

PHYSICS OF THE MOON AND THE PLANETS

(Fizika luny i planet)

I. K. Koval', Chief Editor

Naukova Dumka
Kiev 1964

Translated from Russian

Israel Program for Scientific Translations
Jerusalem 1966

NASA TT F-382
TT 66-51019

Published Pursuant to an Agreement with the
NATIONAL AERONAUTICS AND SPACE ADMINISTRATION, U.S.A.
and
THE NATIONAL SCIENCE FOUNDATION, WASHINGTON, D.C.

Copyright © 1966
Israel Program for Scientific Translations Ltd.
IPST Cat. No. 1548

Translated by Z. Lerman

Printed in Jerusalem by S. Monson
Binding: Wiener Binding Ltd., Jerusalem

Price: \$ 4.00

Available from the
U.S. DEPARTMENT OF COMMERCE
Clearinghouse for Federal Scientific and Technical Information
Springfield, Va. 22151

TABLE OF CONTENTS

Avramchuk, V.V. POLYCHROMATIC POLARIMETRY OF SOME LUNAR REGIONS	1
Mironova, M.N. SPECTROPHOTOMETRY OF SOME LUNAR OBJECTS	11
Sergeeva, A.N. SPECTRAL STUDIES OF THE LUNAR SURFACE	23
Koval', I.K. ON THE STUDY OF THE OPTICAL PROPERTIES OF THE ATMOSPHERE AND SURFACE OF MARS	34
Bugaenko, L.A., O.I. Bugaenko, I.K. Koval', and A.V. Morozhenko. THE BRIGHTNESS DISTRIBUTION IN THE MARGINAL ZONE OF MARS	40
Morozhenko, A.V. RESULTS OF POLARIMETRIC OBSERVATIONS OF MARS IN 1962-1963.	43
Morozhenko, A.V. and E.G. Yanovitskii. DETERMINATION OF OPTICAL PARAMETERS OF THE ATMOSPHERE AND SURFACE OF MARS	61
Yanovitskii, E. G. APPROXIMATE SOLUTION OF THE PROBLEM OF DIFFUSE REFLECTION AND TRANSMISSION OF LIGHT IN PLANETARY ATMOSPHERES WITH AN ARBITRARY SCATTERING INDICATRIX	69
Bugaenko, O.I. DIRECT-READING RECORDING ELECTROPOLARIMETER OF THE MAIN ASTRONOMICAL OBSERVATORY OF THE ACADEMY OF SCIENCES OF THE UKRAINIAN SSR	83
Demenko, A.A. TYPES OF COMETARY TAILS	94
Explanatory List of Abbreviations	104

V. V. Avramchuk
POLYCHROMATIC POLARIMETRY OF SOME LUNAR
REGIONS

The physical meaning of Umov's effect

During recent years several works have been published /1-3/ which give the results of polarimetric observations of lunar objects within narrow spectral regions. These studies have shown that for all the lunar areas investigated the minimum degree of polarization is observed in red light, that is, in the light responsible for the apparent color of the lunar surface, while maximum polarization is observed in blue light. This phenomenon was attributed to Umov's effect /4, 5/ for the colored lunar material. However, since this effect applies to fine-dispersion media, such an explanation inevitably implies that the lunar surface is covered by a dust layer.

The physical meaning of Umov's effect, as Rozenberg /6/ has indicated, is as follows for fine-dispersion media: as the specific absorptivity β of the medium increases, the significance of higher-order scattering is rapidly reduced. The specific absorptivity of a medium is defined as

$$\beta = \frac{\alpha}{\sigma}, \quad (1)$$

where α and σ are, respectively, the coefficients of absorption and scattering of the dispersed medium as a whole. As β increases, the spectral composition and degree of polarization of the reflected light will vary. If we assume that no regular phase interface exists, that is, that the binding medium in which the dispersed phase of the colored material is immersed is identical to the medium above the surface of the scattering medium, then the degree of polarization of the light reflected by the colored material is

$$P = \frac{P_0 + P_\infty \frac{\beta - \beta_0}{(1 + \beta_0)Q}}{1 + \frac{\beta - \beta_0}{(1 + \beta_0)Q}}, \quad (2)$$

where β and β_0 are the specific absorptivities of colored and weakly colored media, P_0 and P_∞ are the degrees of polarization of the reflected light for $\beta = \beta_0 \ll 1$ and $\beta \rightarrow \infty$, and Q is a parameter taking into account the relative contribution of higher-order scattering for $\beta = \beta_0$.

This formula for the degree of polarization of the reflected light as a function of the specific absorptivity β is also essentially a statement of Umov's effect. The degree of polarization varies with wavelength as follows (see /7/):

$$\frac{dP}{d\lambda} \approx \frac{\frac{P_\infty}{P_0} - 1}{(1 + \beta_0)Q + (\beta - \beta_0)} \cdot \frac{\sigma + \alpha}{\sigma^2} \cdot \frac{d\alpha}{d\lambda}. \quad (3)$$

However, in addition to Umov's effect, which is attributable to the varying intensity ratio for scattering of different order, another effect should exist in the presence of a phase interface, as discussed by Toporetz /8/. The other effect consists in a variation of the intensity ratio for the light reflected directly from the interface and the light scattered by the dispersed medium.

Recent photometric investigations of the light scattered by the lunar surface, carried out by Barabashov /9/ and Sharonov /10/ together with their respective co-workers, indicate that no dust is present even at the very surface. This is consistent with Troitskii's radio observations /11/, according to which it is most likely that the lunar material is solid porous.

The results of these observations indicate that the variation of the degree of polarization with wavelength is probably caused by a variation, as β increases, of the relative intensity of light diffusely reflected from the medium interface and scattered in the medium.

Purpose, procedure, and results of observations

According to the preceding theory, polarization observations are suitable for determining the optical characteristics of the lunar material. Moreover, since the lunar surface is a regular furrowed surface, the reflected light must contain a partially polarized component due to diffuse reflection from this surface. The isolation of this component would make possible a quantitative description of the unevenness of the surface layer of the moon.

The authors of articles /1/ through /3/, in which are discussed the polarizing properties of the lunar surface as functions of wavelength, diverge widely in their estimates of the degree of polarization for the very same

lunar details. This makes it difficult to use their data for quantitative calculations. Moreover, the range of light filters used was insufficient to establish the properties of the spectral distribution of the polarization. Therefore, we decided to extend the study of the polarizing properties of the lunar surface details using a greater range of filters.

The wavelength dependence of the degree of polarization during various phases was studied by the author for certain lunar areas in September 1962. Observations were made at the Cassegrainian focus ($F = 10.5$ m) of a 70-cm

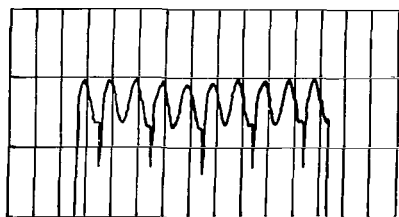


FIGURE 1. Plato Crater, 16-17 September 1962,
0^h05^m (Standard Time), $d = 10''$, PS-11 filter
($\lambda_{\text{eff}} = 390 \text{ m}\mu$)

AZT-2 reflector using an electropolarimeter with a rotating herapathite polaroid. The measured light flux was recorded on an EPP-09 automatic recorder with a natural period of $T_0 = 1$ sec. The transverse dimension of the area accepted by the aperture of the polarimeter mirror scale was $10''$. The degree of polarization was determined using UFS-6, PS-11, SZS-22, ZhS-11, ZhS-16, ZhS-18, OS-13, and KS-11 light filters, which when coupled with our FEU-19M photomultiplier had the following effective wavelengths, respectively: 355, 390, 420, 450, 510, 560, and $600 \text{ m}\mu$. These

filters were also used to determine the instrumental polarization in our telescope + polarimeter system. To do this we observed the star α Lyrae, the light of which is known to be unpolarized, and the results of these observations showed that the parasitic polarization at all wavelengths was below the sensitivity of our apparatus. The observations could thus be regarded as this systematic error.

The degree of polarization of the light reflected by the lunar surface can be calculated from the formula

$$P = \frac{I_{\max} - I_{\min}}{I_{\max} + I_{\min}}, \quad (4)$$

where I_{\max} and I_{\min} are the maximum and minimum deflections of the recorder pen from the zero line.

By adjusting the rotation rate of the polaroid using a ZG-1 sound generator, it was possible to obtain 5 to 10 maximum and minimum pen deflections per minute for each filter, depending on the observation conditions and taking into account the natural period of the recorder. The degree of polarization could thus be calculated as the arithmetic mean of 5 to 10 individual readings. An example of the trace of the polarized light on the recorder strip is shown in Figure 1.

TABLE 1

No.	Name of object	Lunar coordinates		Phase
		φ	λ	
1	Grimaldi (center)	-5.2	-67.0	+12°.0; +39°.0; +55°.0; +68°.0; +92°.0; +104°.5; +117°.0
2	Schickard	-43.8	-55.4	+12°.5; +39°.5; +104°.7; +117°.6; +127°.6; +128°.5
3	Otto Struve	+26.0	-73.6	+13°.7; +40°.0; +54°.0; +66°.8, +104°.5
4	Copernicus	+9.0	-20.0	+40°.5; +52°.8; +68°.6; +104°.7
5	Sinus Iridum	+46.0	-31.6	+12°.0; +40°.0; +52°.5; +67°.0; +92°.5; +104°.3; -20°.3
6	Plato	+51.2	-10.0	+12°.0; +40°.0; +52°.5; +66°.5; +92°.5; +104°.5; -20°.3
7	Archimedes	+29.8	-4.0	+55°.0; +67°.6; +80°.0; +92°.5; -20°.3
8	Mare Imbrium	+30.0	-1.5	+55°.3; +67°.7; +80°.0; +92°.8
9	Aristillus	+33.3	+2.0	+55°.1; -20°.3
10	Tycho	-43.0	-11.1	+40°.3; +53°.0; +68°.5; -20°.3
11	Theophilus	-11.7	+26.6	+53°.2
12	Cyrillus	-13.3	+24.0	+53°.5
13	Catharina	-17.4	+23.0	+53°.6; +67°.0
14	Ridge between Catharina and Cyrillus	-15.0	+24.5	+53°.8
15	Palus Somnii	+16.0	+46.8	+13°.2
16	Visible center of Mare Crisium	+16.0	+60.0	+11°.7
17	Cleomedes	+27.3	+56.0	+13°.5
18	Part of Mare Foecunditatis near Tarantius	+6.0	+46.7	+42°.0.

The final results of the calculations have a relative error of 10 to 15 % for $P = 0.01$ to 0.02 and 2 to 5 % for $P > 0.04$. The actual deviation of the observations on individual nights from the mean values of the phase curve does not exceed $P = 0.003$ to 0.005 .

TABLE 2

Phase	$\lambda_{\text{eff}}, \text{m}\mu$							
	355	390	420	450	475	510	560	600
Grimaldi								
+ 12°.0	—	1.47	1.57	1.39	1.50	1.78	—	2.10
+ 39.0	6.20	4.45	4.40	3.80	3.60	3.35	3.10	3.50
+ 55.0	11.2	9.20	8.20	7.35	7.20	6.30	6.40	6.50
+ 68.0	15.3	12.8	11.1	10.0	10.0	8.70	9.15	9.00
+ 92.0	—	16.8	15.3	14.0	13.7	12.4	11.8	12.2
+ 104.5	—	18.0	15.7	15.4	14.5	12.8	11.6	12.1
+ 117.0	—	18.3	14.9	—	13.1	11.6	11.0	—
Schickard								
+ 12.5	—	1.33	1.16	1.30	1.34	1.44	1.75	—
+ 39.5	4.32	—	3.17	3.02	2.77	3.11	2.85	—
+ 104.7	—	9.44	8.47	8.58	7.69	7.20	6.53	5.98
+ 128.5	—	8.70	7.20	—	7.40	7.00	5.80	—
Otto Struve								
+ 13.7	—	1.21	1.15	1.05	1.02	1.37	1.46	1.64
+ 40.0	6.33	4.86	3.99	4.22	4.13	3.85	3.56	3.40
+ 54.0	—	9.52	8.22	7.87	7.50	6.79	6.77	6.93
+ 66.8	16.0	13.4	11.3	10.7	10.9	9.74	9.11	9.54
+ 104.5	—	19.5	16.4	16.1	14.9	14.4	12.0	12.0
Copernicus								
+ 40.5	3.08	2.38	2.09	2.08	2.14	1.81	1.84	1.82
+ 52.8	4.75	4.40	3.84	3.79	3.66	3.46	3.75	3.22
+ 68.6	8.32	6.27	5.93	5.52	5.21	5.17	4.90	4.90
+ 104.7	—	8.43	7.21	6.63	7.16	6.33	6.30	5.83
Sinus Iridum								
+ 12.0	—	1.30	1.25	1.33	1.32	1.49	1.56	2.42
+ 40.0	6.60	4.80	3.75	3.70	3.70	3.50	3.35	3.20
+ 52.5	10.9	7.80	6.85	6.80	6.80	6.25	5.75	6.00
+ 67.0	15.9	11.4	10.3	9.50	9.70	9.20	8.40	8.40
+ 92.5	—	17.3	14.5	13.4	12.4	12.3	11.1	10.4
+ 104.3	—	17.8	15.1	14.4	13.0	12.7	11.4	10.7
— 20.3	—	0.0	0.0	0.0	0.0	0.0	0.0	0.0
Plato								
+ 12.0	—	1.18	—	1.38	1.58	1.46	1.70	2.01
+ 40.0	6.73	4.60	3.90	3.80	3.71	3.43	3.50	3.20
+ 52.5	13.2	8.45	8.00	7.30	7.20	6.40	6.45	6.30
+ 66.5	18.5	12.7	11.5	11.0	10.4	9.60	9.25	9.30
+ 92.5	—	18.6	16.3	16.1	15.1	14.1	13.2	12.5
+ 104.5	—	19.7	17.9	16.9	16.2	14.3	13.6	—
— 20.3	—	0.0	0.0	0.0	0.0	0.0	0.0	0.0
Archimedes								
+ 55°.0	9.55	7.72	6.60	6.60	6.10	5.90	5.30	5.25
+ 67.6	13.2	10.5	9.20	8.90	8.20	7.90	7.35	7.35
+ 80.0	22.0	13.1	11.5	10.9	10.2	10.0	9.30	9.30
+ 92.5	—	15.2	13.6	12.7	12.2	11.5	11.0	10.3
— 20.3	0.0	0.0	0.0	0.0	0.0	0.0	0.0	0.0
Mare Imbrium								
+ 55.3	9.60	6.74	6.20	5.90	5.45	5.35	4.90	5.30
+ 67.7	11.1	9.90	7.90	7.80	7.55	7.00	6.95	6.20
+ 80.0	—	11.1	9.30	9.30	8.80	8.30	7.65	7.10
+ 92.8	—	13.5	11.4	10.6	—	—	—	—
Aristillus								
+ 55.1	8.97	6.86	5.78	5.62	5.34	4.99	4.64	4.57
— 20.3	0.0	0.0	0.0	0.0	0.0	0.0	0.0	0.0

TABLE 2 (continued)

Phase	$\lambda_{\text{eff}}, \text{ m}\mu$							
	355	390	420	450	475	510	560	600
Tycho								
+ 40 .3	—	2.29	1.85	2.20	2.20	1.92	1.96	2.30
+ 53 .0	—	—	3.50	3.60	3.60	3.15	3.10	3.40
+ 68 .5	7.27	5.54	5.00	4.95	4.65	4.60	4.50	4.55
— 20 .3	0.0	0.0	0.0	0.0	0.0	0.0	0.0	0.0
Theophilus								
+ 53 .2	6.27	4.93	4.29	4.35	3.97	3.80	3.67	—
Cyrillus								
+ 53 .5	5.16	3.70	3.22	3.28	3.71	3.60	3.10	3.75
Catharina								
+ 53 .6	4.88	4.18	3.76	3.71	3.75	3.55	3.61	3.79
+ 67 .0	7.74	6.12	5.66	5.18	5.02	5.06	4.90	5.19
Ridge between Catharina and Cyrillus								
+ 53 .8	5.01	4.26	—	4.09	3.04	—	4.13	—
Palus Somnii								
+ 13 .2	—	—	1.49	1.89	1.55	1.47	1.68	1.71
Visible center of Mare Crisium								
+ 11 .7	—	1.07	0.93	1.19	1.39	1.55	2.03	—
Cleomedes								
+ 13 .5	—	1.52	1.53	1.63	1.51	1.51	—	—
Part of Mare Foecunditatis near Taruntius								
+ 42 .0	—	3.70	3.25	3.32	3.15	3.10	3.49	4.08

Observations were made of various formations which had been investigated by other authors and also of some new formations. The names and coordinates of these formations, and also the phases during which the observations were made, are listed in Table 1. The phases are all topocentric (about $50^{\circ}21'55''\text{N}$., the latitude of the Main Astronomical Observatory of the UkrSSR Academy of Sciences). The phase angle was assumed to be positive after full moon. The data obtained are given in Table 2. Each table gives the topocentric phase angles at the time of observation, the effective wavelengths of the filter+photocathode system, and the final values of the degree of polarization.

A discussion of the results

1. The first significant feature is the variation of the degree of polarization with wavelength at phases of $+12^{\circ}$ to $+13^{\circ}$. According to Lyot [12] and Kokhan [1], the negative-polarization maximum is located near this phase. Kokhan's measurements of polarization with yellow and blue filters showed that both negative and positive polarizations are higher in blue light.

We obtained the spectral distribution of negative polarization for some lunar features at the above phase. The polarization was found to increase toward the red for all features, which contradicts the results of Kokhan.

This effect was noted by us in January 1962 during observations of Sinus Iridum and Plato; the results of the observations made in September 1962 confirm this phenomenon. The discrepancy between our results and those of Kokhan is apparently due to the fact that we worked with a wider range of wavelengths (390–600 m μ) than Kokhan did (460–560 m μ). The wavelength dependence of the negative polarization is shown in Figure 2.

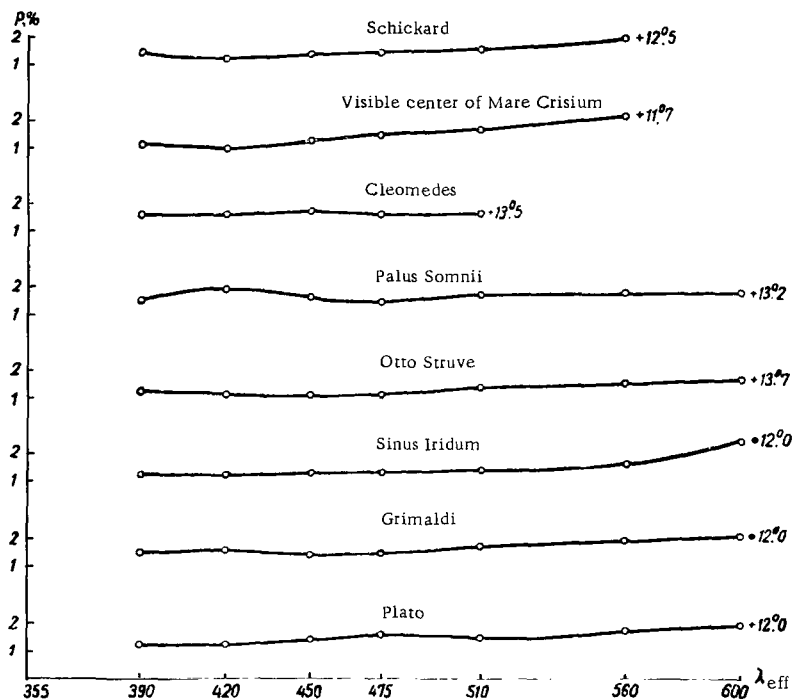


FIGURE 2. Degree of polarization as a function of wavelength for phases near +12° to +13°

If this effect of an increase in negative polarization toward the red is confirmed by subsequent observations of many lunar features over a wider spectral region, then it must imply some special mechanism for creating negative polarization.

As yet no theory has been formulated which would explain satisfactorily the creation of negative polarization during the diffuse reflection of light from a solid body. The familiar hypotheses of Lyot [12] and Ohman [13] dealing with the origin of negative polarization require further elaboration and experimental verification. However, it should be remembered that these hypotheses presuppose the presence of a phase interface between the scattering medium and the medium above it, which would be the case for a solid structure of the lunar material.

2. The wide range of filters with λ_{eff} from 355 to 600 m μ made it possible to carry out a detailed examination of the variation of the degree of polarization with wavelength. The degree of positive polarization varies almost

monotonically and increases sharply in the ultraviolet. This is especially pronounced for Plato, Grimaldi, Otto Struve, and some other lunar formations. The degree of polarization as a function of wavelength for Plato is shown in Figure 3.

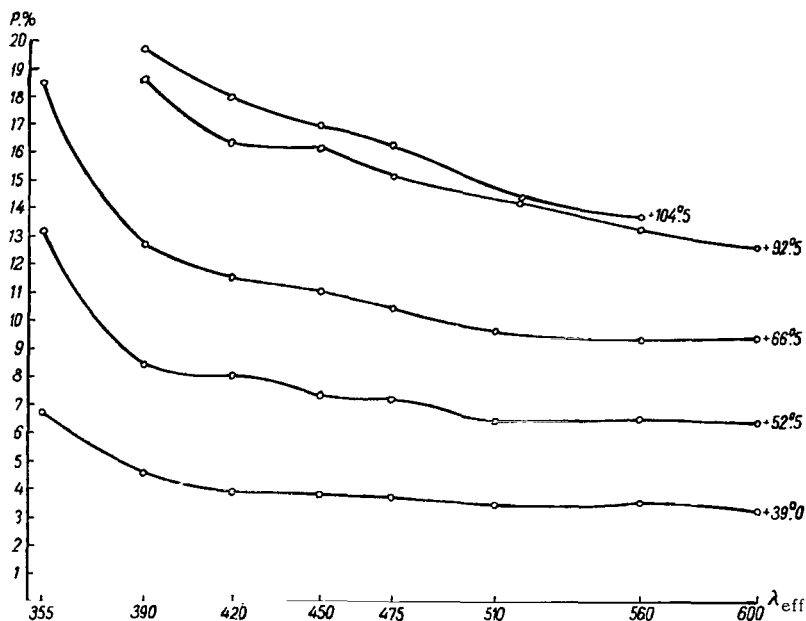


FIGURE 3. Degree of polarization as a function of wavelength for Plato Crater, for various phase angles

On the other hand, craters like Tycho and Copernicus have a degree of polarization which varies negligibly with wavelength in the 420–600 mμ range and increases only in the ultraviolet. This property is illustrated in Figure 4 for Tycho Crater.

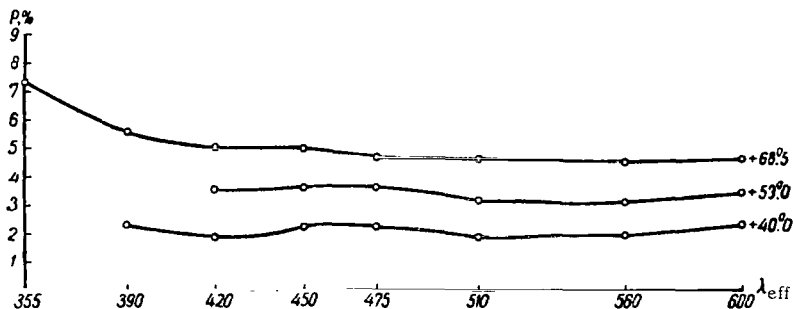


FIGURE 4. Degree of polarization as a function of wavelength for Tycho Crater

A characteristic feature of the spectral distribution of the polarization of moonlight is the slight wave observed in the 420–450 mμ range for almost all formations.

3. Repeated attempts have been made to establish a relation between the maximum degree of polarization and the absolute reflectance. Sytinskaya /14/ compared the maximum polarizations P_{\max} at a phase angle of $+90^\circ$ for 11 lunar objects, according to the data of Lyot, with the values of the visual albedo A_v of the full moon. She obtained the following linear relation:

$$P_{\max} = 0.276 - 1.95 A_v. \quad (5)$$

In addition, Barabashov and Ezerskii /15/ analyzed the correlation between P_{\max} and $\log A_v$ using the data of the polarimetric observations of Dzhapiashvili and Kokhan and the photometric data of Fedorets; they concluded that the relation between P_{\max} and $\log A_v$ is linear.

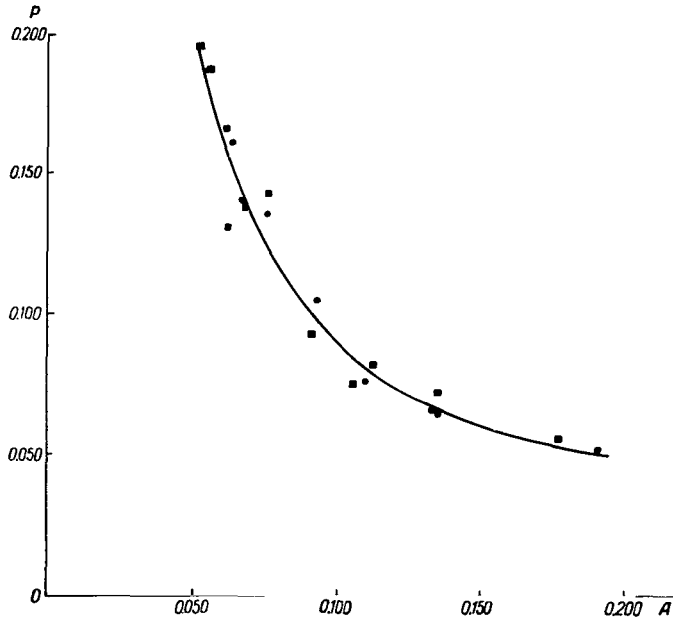


FIGURE 5. Maximum degree of polarization as a function of albedo in two spectral regions ($\lambda_{\text{eff}} = 430$ and $560 \text{ m}\mu$)

■ — albedo and polarization for $\lambda_{\text{eff}} = 430 \text{ m}\mu$; ● — albedo and polarization for $\lambda_{\text{eff}} = 560 \text{ m}\mu$

We have tried to verify the hypothesis that the relation between the maximum polarization and the albedo is linear in narrow spectral regions. To do this, we used the albedos for λ_{eff} values of 430 and $560 \text{ m}\mu$ given by Radlova's catalog /16/ and the maximum degrees of polarization obtained by Kokhan /1/ and in the present work. The resulting curve has been plotted in Figure 5. As we see, in the relevant range of polarization and albedo, the function is hyperbolic. This curve may be represented analytically with sufficient accuracy by the formula

$$P_{\max} = \frac{0.0092}{A}. \quad (6)$$

Empirical formula (6) gives the relation between the maximum degree of polarization and the albedo in narrow spectral regions.

4. For a phase of $-20^\circ.3$ no polarization was detected throughout the entire spectral range studied. This shows that the inversion angle for the lunar surface is independent of wavelength.

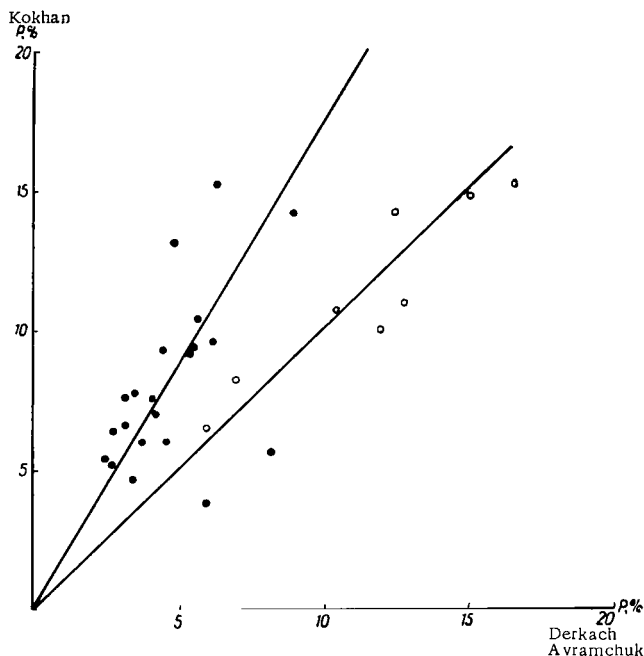


FIGURE 6. Comparison of polarimetric data of Kokhan, Derkach, and the author

●-results of Kokhan and Derkach; ○-results of Kokhan and the author

5. A comparison of the results of observations by various authors shows that their estimates of the degree of polarization for the very same lunar features differ. We compared the results of the observations of Kokhan, Derkach, and ourselves. By plotting Kokhan's results along the y axis and Derkach's results along the x axis, we obtained a systematic deviation of the compared results, relative to a line of symmetry. A comparison of our results with those of Kokhan then shows only a random scatter of points about the axis of symmetry. This indicates that Derkach's observational data are low by a factor of 1.7. There are various possible reasons for such an error, and we shall now indicate some of them. It has been established that in the dust-filled atmosphere of the earth the degree of polarization varies with the air mass. In addition, the results obtained may be influenced strongly by parasitic polarization in the instruments, by poor quality of the polaroid, by the use of photomultipliers with lateral input, etc. All these factors make necessary a very careful approach to the analysis of polarimetric data.

In conclusion, I wish to express my thanks to A. V. Markov and to V. P. Konopleva, whose initiative made this study possible.

REFERENCES

1. KOKHAN, E. K.—Izvestiya komissii po fizike planet, No. 1: 41. 1959.
2. TEIFEL', V. G.—Astronomicheskii Zhurnal, 37(4): 703. 1960.
3. DERKACH, K. N.—Trudy Khar'kovskoi astronomicheskoi observatorii, Vol. 14: 79. 1962.
4. UMOFF, N. A.—Phys. L.S., Vol. 6: 674. 1905.
5. UMOFF, N. A.—Phys. L.S., Vol. 8: 258. 1909.
6. ROZENBERG, G. V.—Uspekhi fizicheskikh nauk, 69(1): 57. 1959.
7. ROZENBERG, G. V.—Sbornik pamyati akademika P. P. Lazareva, p. 132. 1956.
8. TOPORETS, A. S.—Zhurnal eksperimental'noi i teoreticheskoi fiziki, 20(5): 390. 1950.
9. BARABASHOV, N. P. and A. T. CHEKIRDA.—Astronomicheskii Zhurnal, 36(5): 851. 1959.
10. SHARONOV, V. V.—In the collection "Luna", edited by V. V. Markov, p. 331. 1960.
11. TROITSKII, V. S.—Astronomicheskii Zhurnal, 39(1): 73. 1962.
12. LYOT, B.—Ann. d'Obs. de Paris, sect. de Meudon, Vol. 8, part 1. 1929.
13. OHMAN, Y.—Stockh. Obs. Ann. Vol. 18, No. 8. 1950.
14. SYTINSKAYA, N. N.—Astronomicheskii Tsirkulyar, Vol. 168: 18. 1956.
15. BARABASHOV, N. P. and V. I. EZERSKII.—Trudy Khar'kovskoi astronomicheskoi observatorii, Vol. 14: 5. 1962.
16. RADLOVA, L. N.—Astronomicheskii Zhurnal, 20(5-6): 1. 1943.

M. N. Mironova

SPECTROPHOTOMETRY OF SOME LUNAR OBJECTS

The study of selected lunar areas undertaken at the Main Astronomical Observatory of the UkrSSR Academy of Sciences was designed to bring out certain special features in the spectra of the objects observed. Such features might include the presence of emission gas bands, luminescence bands, or, finally, differences in the spectral reflectivities of the lunar formations concerned. In each of the craters chosen for study, selenologists had at some time noticed certain changes which could be indicative of volcanic activity in the given lunar region. The craters studied were Alhazen, Messier, Linné, Hyginus, Plato, Alphonsus, Arzachel, Ptolemaeus, Herodotus, Aristarchus, and Schickard. We made use of two different means of solving the problem: 1) by obtaining the spectral brightness coefficients (in this case, additional observations were required to standardize the lunar spectrograms and to determine the spectral transmission coefficients of the earth's atmosphere; and 2) comparing the spectra of the various lunar objects with one another. In this report we shall present the results obtained using both methods.

Observations

From July 1960 to July 1961, at definite lunation periods, we made a systematic collection of spectrograms of the selected lunar objects using

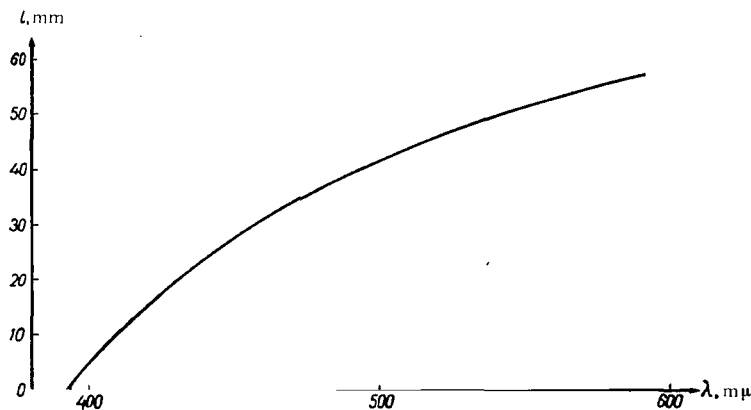


FIGURE 1. Dispersion curve of ASP-5 spectrograph

an ASP-5 spectrograph mounted at the 10.5-m Cassegrainian focus of the 70-cm reflector at the Main Astronomical Observatory. Figure 1 gives the dispersion curve of the spectrograph used. The slit (0.05 mm in width) was aligned parallel to the right ascension. During the repeated observations, in order to ensure that the position of the slit relative to the lunar disk was the same as before the spectrograph was rotated about its axis by means of a positioning bearing.

TABLE 1

Number of plates	Object	Date	Universal time	Exposure time	Plate type
23	Aristarchus and Herodotus	4/5 IX 1960	19 ^h 50 ^m	1 ^m ; 5 ^m ; 10 ^m ; 15 ^m ;	Agfa Rot Rapid
24	Aristarchus	"	20 30	1; 5; 10;	"
25	"	"	21 00	1; 1; 5; 10;	"
26	Plato	"	21 59	1; 1; 5; 15;	"
27	Tycho	4/5 IX 1960	22 30	1; — — 15;	"
28	Aristarchus	"	22 45	1; — 5;	"
31	"	5/6 IX 1960	21 00	1; 1; 5; 10;	"
71	"	28/29 III 1961	18 25	— — 5; 15;	Kodak oaF
73	"	"	19 24	— 3; 5; 15;	"
93	"	29/30 IV 1961	21 15	— 2; 5; —	"
104	Alphonsus	23/24 V 1961	19 50	— — 5; 10;	"
105	"	"	20 51	— — 5; 15;	"
106	"	"	21 28	— — — 10;	"
150	Aristarchus	1 VII 1961	00 45	— — 1; 3;	"
160	"	21/22 VIII 1962	23 37	— — 3; 15;	Agfa Isopan ISS
161	"	"	00 55	— — 3; 15;	"
162	Schickard	"	01 52	— — — 15;	"
163	"	"	02 04	— — 5;	"
163	Aristarchus	"	02 18	— — — 15;	"

The spectrogram scale was 25" per mm. Calibration was performed using a step reducer, in front of which was placed a piece of frosted glass illuminated by scattered skylight. In some cases, a standard light bulb was used for calibration. In order to increase the range of densities, we made several prints of the reducer using various slit widths for the same exposure time.

The prints were developed using D-19 developer. A batch of plates which included the lunar spectrograms, the calibration spectrograms, and the standardization spectrograms were placed simultaneously in the developing tank. The following photographic plates were used: Kodak oaF, Agfa Rot Rapid, and Agfa Isopan ISS. A total of about 500 spectrograms were obtained. Table 1 lists the statistics for the lunar objects observed in this study.

Processing of the spectrograms

The spectrograms were measured on an MF-4 microphotometer with an FEU-19M photomultiplier used as a radiation detector; the plate blackenings were recorded on an automatic recorder. The microphotometer slit took

in only a small portion of the spectrogram (0.03×0.07 mm), which enabled us to measure separately the densities of the walls, floors, and central peaks of the craters studied. The scale of the recorder traces ranged from 30:1 to 100:1. The measurements were made within selected wavelength intervals of the continuous spectrum. A characteristic curve was plotted for each of these intervals ($\Delta\lambda < 0.5$ to $1.0 \text{ m}\mu$).

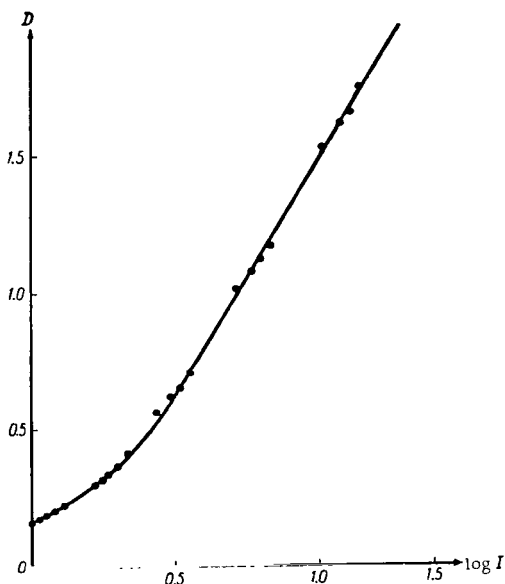


FIGURE 2. Characteristic curve for Agfa Isopan ISS plates, exposure of 5^m

The transmittances of the reducer steps, in units of the transmittance of the densest step, were as follows: I-1.0, II-1.7, III-2.7, IV-5.2, V-10.7, VI-25.1.

Since the steps were close to one another, the Eberhard effect manifested itself when the densities of steps V and VI were considerable. In such cases the characteristic curve was plotted from the measurements of the first four steps only. In order to increase the accuracy with which the characteristic curve was plotted, not one but several close points were taken in the measured wavelength interval. Figure 2 shows a typical characteristic curve for an Agfa Isopan ISS plate, at $\lambda = 564.5 \text{ m}\mu$.

The spectral brightness coefficients

The spectral reflectivities of the rocks lining the floors and walls of lunar craters can be characterized in terms of spectral brightness coefficients. The latter are determined by measuring the ratio between the brightness of the studied object and the brightness of a standard with a known spectral reflecting characteristic.

In our work we used as a standard a barium scattering screen mounted normal to the sun's rays at a height of about 15 m and at a distance of 200 m from the reflector. Table 2 gives the spectral brightness coefficients of the screen, obtained using an SF-2 spectrophotometer.

TABLE 2

$\lambda, \text{m}\mu$	434.6	442.6	456.2	468.4	478.8	494.0	508.8	537.2	562.0	581.6	606.0	623.2
r_s	0.80	0.80	0.82	0.82	0.82	0.82	0.81	0.79	0.78	0.78	0.78	0.78

A focused image of the screen was formed at the spectrograph slit by varying the distance between the main mirror and the hyperbolic mirror. Since the moon and the screen were observed with different equivalent focal lengths, the desired ratio between the brightnesses of the moon and the screen $\left(\frac{b_m}{b_s}\right)$ was not equal to the ratio of the respective illuminations created at the spectrograph slit $\left(\frac{e_m}{e_s}\right)$. In this case the ratios are related by the formula

$$\frac{b_m}{b_s} = \frac{e_m}{e_s} \left(\frac{F}{F + \Delta F} \right)^2,$$

where ΔF is the change in focal length.

This relation can also be written as

$$\frac{b_m}{b_s} = \frac{e_m}{e_s} \left(1 - \frac{\Delta d}{F_1 + F_2 - d_m} \right)^2.$$

Here d is the distance between the main mirror and the hyperbolic mirror, F_2 is the focal length of the hyperbolic mirror, F_1 is the focal length of the main mirror, and $\Delta d = d_s - d_m$.

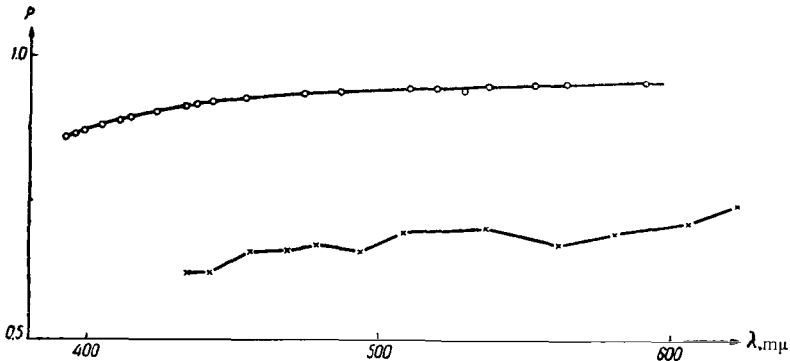


FIGURE 3. Spectral coefficients of atmospheric transmission;

x—for the night of 23-24 May 1961; o—for the night of 21-22 August 1962

A 400-mm-diameter diaphragm set up in front of the main mirror reduced the illumination produced by the screen at the spectrograph slit by a factor of 3.87.

The spectrum of the screen was obtained twice, once when illuminated by the sun and the scattered skylight and once when illuminated by scattered skylight alone. The direct rays of the sun were cut off by placing a 0.4×0.4 m partition at a distance of 1.5 m from the screen. The screen brightness due just to the direct sun rays was then calculated from the formula

$$b(\lambda)_s = b(\lambda)_{s+d} - b(\lambda)_d,$$

where $b(\lambda)_s$ is the monochromatic brightness of the screen illuminated by direct sun rays, $b(\lambda)_{s+d}$ is the monochromatic brightness of the screen illuminated by the sun plus scattered skylight, and $b(\lambda)_d$ is the monochromatic brightness of the screen illuminated just by scattered skylight.

TABLE 3

Date	Moon				Sun
	z_1	z_2	z_3	z_4	z_0
23/24 V 1961	54°33'	56°19'	61°44'	66°52'	49°30'
21/22 VIII 1962	39 12	47 47	58 52	—	44 57

The spectral brightness coefficients were determined using the following formula, which incorporates all the previously mentioned corrections:

$$r(\lambda) = 3.87 \frac{k r_s(\lambda)}{\cos i} \frac{e_m}{e_s} \left(1 - \frac{\Delta d}{F_1 + F_2 - d_m} \right)^3 p(\lambda)^{|M(z_0) - M(z_m)|},$$

where i is the angle of incidence of the sun rays, and k is the coefficient of reduction to zero phase (found from the phase curve obtained by Fedoretts /3/ for the crater in question).

TABLE 4

No.	Description	No. of spectrograms	No. of plates	D
1	Floor of Alphonsus west of central peak	5	104; 105; 106;	0 ^m .11
2	Eastern wall of Alphonsus	5	" " "	0.22
3	Central peak of Alphonsus	5	" " "	0.23
4	Western wall of Alphonsus	5	" " "	0.13
5	Oceanus Procellarum east of Aristarchus	5	160; 161; 163;	0.08
6	Bright halo around Aristarchus	5	" " "	0.12
7	Eastern wall of Aristarchus	5	" " "	0.10
8	Floor of Aristarchus	5	" " "	0.12
9	Western wall of Aristarchus	5	" " "	0.10
10	Western part of bright halo around Aristarchus	5	" " "	0.14
11	Oceanus Procellarum east of Aristarchus	5	" " "	0.01
12	Western wall of Herodotus	3	161; 163;	0.06
13	Eastern wall of Herodotus	3	" " "	0.14
14	Wall of Schickard	2	162; 163;	0.06
15	Area south of Schickard	2	" " "	0.01
16	Floor of Schickard	2	" " "	0.06

The spectral coefficient of atmospheric transmission $p(\lambda)$ was determined from spectrograms of the moon obtained on the night of observation

TABLE 5

λ , m μ	r_1	r_2	r_3	r_4	λ , m μ	r_5	σ_5	r_6	σ_6	r_7	σ_7	r_8	σ_8	r_9	σ_9	r_{10}	σ_{10}	r_{11}	σ_{11}	r_{12}	r_{13}	r_{14}	r_{15}	r_{16}
623	0.070	0.092	0.101	0.109																				
606	.068	.088	.106	.108																				
594	.066	.086	.100	.102	591	0.139	± 0.000	0.267	± 0.003	0.592	± 0.000	0.591	± 0.011	0.497	± 0.017	0.232	—	0.139	± 0.003	0.287	0.259	0.250	0.220	0.253
582	.055	.067	.078	.099	564	.123	.004	.222	.004	.512	.003	.505	.005	.417	.004	.220	± 0.001	.125	.009	.251	.216	.203	.172	.205
576	.057	.070	.084	.101	553	.128	.003	.243	.005	.531	.005	.521	—	.436	.000	.243	.007	.122	.003	.253	.238	.206	.175	.206
570	.058	.071	.085	.101	538	.133	.005	.251	.001	.545	.003	.539	.005	.452	.005	.249	.001	.130	.003	.271	.234	.221	.191	.223
562	.065	.079	.090	.103	529	.112	.004	.207	.003	.482	.004	.485	.013	.391	.008	.213	.007	.106	.000	.227	.196	.191	.163	.190
552	.061	.080	.089	.103	519	.105	.003	.191	.004	.453	.013	.447	.007	.352	.004	.190	.000	.103	.000	.208	.185	.173	.148	.173
537	.067	.074	.087	.098	510	.106	.003	.197	.000	.427	.003	.430	.004	.354	.003	.194	.000	.104	.000	.213	.186	.174	.151	.175
519	.060	.070	.084	.097	487	.098	.000	.185	.003	.422	.001	.407	.001	.332	.011	.184	.000	.095	.004	.194	.166	.163	.138	.161
513	.057	.064	.080	.094	474	.114	.003	.207	.001	.443	.004	.439	.003	.364	.004	.207	.005	.110	.001	.223	.196	.172	.156	.182
509	.054	.062	.069	.088	454	.112	.001	.209	.000	.467	.014	.446	.017	.370	.003	.210	.001	.111	.000	.228	.195	.185	.160	.182
494	.052	.058	.068	.086	443	.119	.001	.217	.000	.484	.003	.468	.000	.395	.016	.214	.001	.121	.001	.239	.209	.194	.173	.195
479	.049	.058	.071	.086	437	.112	.000	.209	—	.436	.009	.430	.004	.351	.008	.206	.003	.098	—	.220	.196	.179	.163	.177
468	.050	.062	.069	.089	433	.113	.001	.208	.000	.427	.000	.428	.000	.356	.014	.204	.001	.115	—	.224	.204	.184	.164	.192
456	.055	.061	.072	.095	423	.097	.005	.187	.015	.390	.013	.474	.017	.322	.003	.183	.004	.103	—	.209	.177	.167	.152	.163
443	.055	.065	.072	.091	415	.083	.004	.176	.005	.368	.001	.355	.011	.297	.001	.172	.005	.099	—	.187	.161	.156	.138	.152
435	.053	.060	.062	.079	411	.085	.005	.176	.011	.374	.011	.367	.008	.306	.013	.173	.001	.098	—	.103	.172	.161	.145	.152
433	.068	—	.068	.079	405	.073	.004	.150	.000	.307	.008	.312	.004	.265	.007	.153	.003	.081	—	.171	.139	.130	.120	.135

for various zenith distances z_k . The calculations were made by the method of least squares, using the formula

$$\log p(\lambda) = \frac{\sum_{i,j} [M(z_i) - M(z_j)] [\log I(z_i) - \log I(z_j)]}{\sum_{i,j} [M(z_i) - M(z_j)]^2},$$

where $M(z_k)$ is the air mass and $I(z_k)$ is the luminous intensity of the moon for a zenith distance z_k .

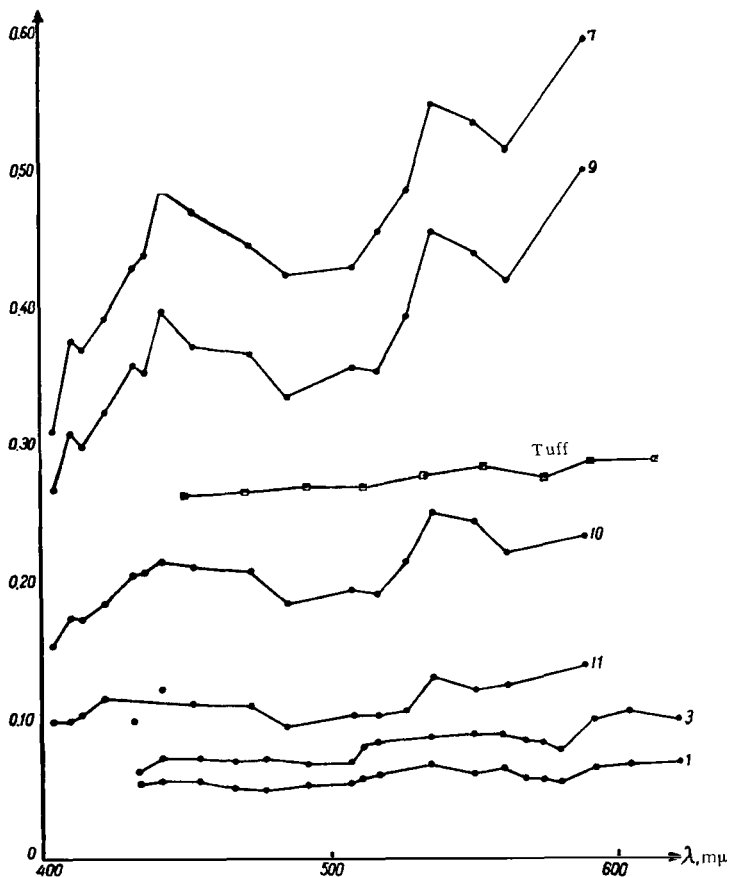


FIGURE 4. Curves of spectral brightness coefficients

Each lunar spectrogram is a combination of a multitude of spectra of different details of the lunar surface. The differences $[\log I(z_i) - \log I(z_j)]$ can therefore be obtained as the averages of the measurements of several such spectra, which increases the accuracy of determining $p(\lambda)$. Figure 3 shows the spectral coefficients of atmospheric transmission for the nights of 23-24 May 1961 and 21-22 August 1962.

The daytime and nighttime atmospheric transmissions were assumed to be the same. The zenith distances of the moon and sun at the time of observation are given in Table 3.

Table 4 gives a description of the measured parts of the craters studied. The yellowness index was determined from the formula

$$D = -2.5 \log \frac{r_{\lambda=443}}{r_{\lambda=553}}.$$

The spectral brightness coefficients and the rms error $\sigma(\lambda)$ for a single measurement are listed in Table 5. Figure 4 shows the $r(\lambda)$ curves for some of the lunar features described in Table 4.

An analysis of the results leads to the following conclusions:

1. The $r(\lambda)$ curves for most of the lunar features measured have a local maximum near $\lambda = 550 \text{ m}\mu$. A slight wave is also observed at about $\lambda = 450 \text{ m}\mu$. A similar curve was obtained by Sharonov /7/ (from the measurements of Wilsing and Scheiner) for the bright spot in the northwestern part of Mare Tranquillitatis.
2. The curves of the spectral brightness coefficients can be classified according to Krinov's spectrophotometric system /4/ as Class I, Type 2. Such curves correspond to taluses and cliffs, rock debris, slopes, etc.
3. Of the numerous rock types studied by Barabashov and Chekirda /5/, the one which is closest in spectral reflectivity to the lunar areas investigated by us is lava tuff.
4. Figure 4 shows the $r(\lambda)$ curve obtained by Sharonov /7/ (from the measurements of Wilsing and Scheiner) for basalt tuff. Although the spectral coefficients for basalt tuff are higher than those for the lunar material, the spectral distribution of $r(\lambda)$ is very similar to that obtained for the details of Alphonsus.
5. The difference in the color indexes obtained by us for the craters investigated does not exceed $0^m.18$.

Relative measurements

If a sufficiently wide slit is used, a lunar spectrogram will contain not only the spectrum of the central peak of a crater but also spectra of the floor, the walls, and even the area surrounding the crater. By comparing the spectra for such small areas of the lunar surface we can obtain interesting information concerning differences in the spectral reflectivities of these areas. Since the spectra compared are obtained for the same zenith distance, it is unnecessary to take into account absorption in the earth's atmosphere, and this simplifies the processing considerably.

Table 6 describes the lunar areas being compared. The results are represented in the form of color contrasts for two compared areas x and y . The following formula was used:

$$CE(\lambda)_x y = -2.5 \left[\log \left(\frac{I_x}{I_y} \right)_{\lambda_i} - \log \left(\frac{I_x}{I_y} \right)_{\lambda_0=550} \right].$$

Figure 5 gives the color-contrast curves plotted after averaging 3 or 4 spectrograms obtained with different exposure times. On each spectrogram

only those regions were measured whose photometric densities corresponded to the linear portion of the characteristic curve. The color-contrast curves for individual areas of Plato and Tycho indicate a considerable difference

TABLE 6

No.	Description	No. of plates	No. of spectrograms	No.	Description	No. of plates	No. of spectrograms
1	Aristarchus (northern wall)	24	4	9	Oceanus Procellarum	25	4
2	Oceanus Procellarum	24	4	10	Tycho (eastern wall)	27	2
3	Herodotus (northern wall)	24	4	11	Tycho (western wall)	27	2
4	Oceanus Procellarum	24	4	12	Tycho (central peak)	27	2
5	Aristarchus (southern wall)	23	4	13	Tycho (floor)	27	2
6	Oceanus Procellarum	23	4	14	Plato (western wall)	26	4
7	Aristarchus (eastern wall)	25	4	15	Plato (floor)	26	4
8	Aristarchus (western wall)	25	4				

in the spectral reflectivities of the walls and the floors. For Aristarchus, however, the picture is entirely different. The western (8-9 in Figure 6), eastern (7-9), northern (1-2), and southern (5-6) parts of the wall of Aristarchus show an increase in reflectivity at two wavelengths: $\lambda = 505$ and 425μ .

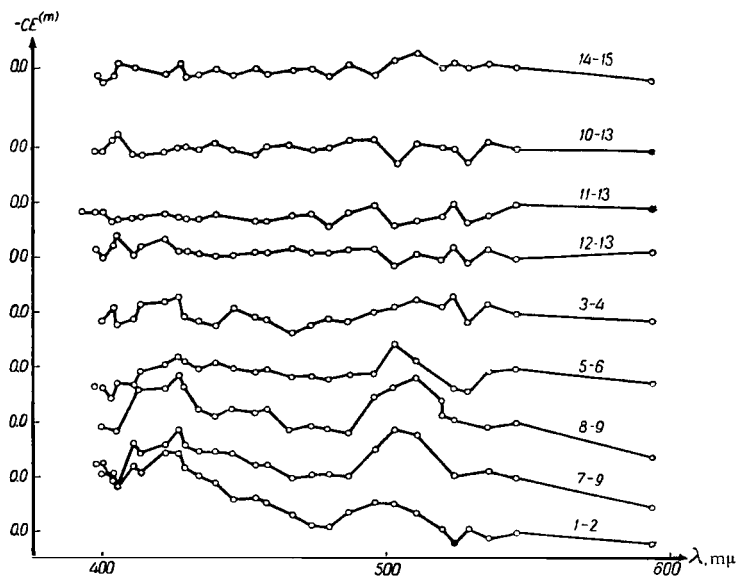


FIGURE 5. Color-contrast curves for two compared lunar areas:

northern (1-2), southern (5-6), and western (8-9) parts of wall of Aristarchus; eastern (10-13) and western (11-13) walls of Tycho; central peak of Tycho (12-13); western wall of Plato (14-15)

In order to establish the nature of the rise in the color-contrast curves, we proceeded with additional detailed measurements of plates 25, 28, and 31.

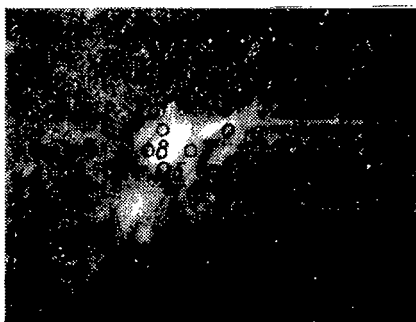


FIGURE 6. Aristarchus Crater

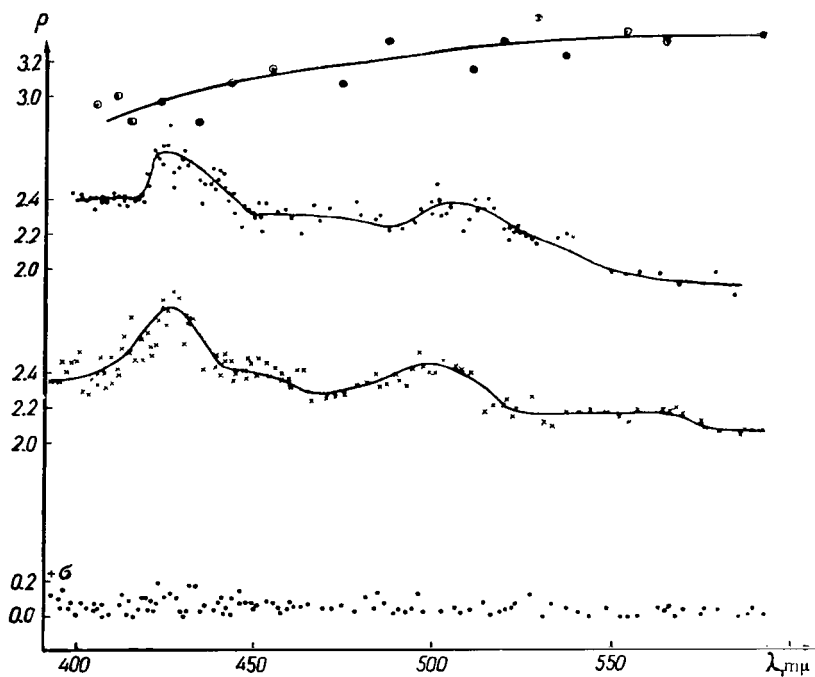


FIGURE 7. Relative spectral characteristic of Aristarchus

○ - phase angle $\phi = +84^\circ$; ● - $\phi = +5^\circ.4$; × - $\phi = -8^\circ.0$; ◊ - rms error of a single measurement for plates 25 and 28 ($\phi = -8^\circ.0$)

The results were represented in the form

$$\rho(\lambda) = \frac{I(\lambda)_x}{I(\lambda)_0},$$

where $I(\lambda)_x$ is the monochromatic brightness of Aristarchus (in these

measurements the slit width was increased to take in the entire crater), and $I(\lambda)_0$ is the monochromatic brightness of the area in Oceanus Procellarum to the east of Herodotus.

Figure 7 shows the $\rho(\lambda)$ curves for Aristarchus during three different phases of the moon, and also the $\sigma(\lambda)$ values characterizing the variation of the rms error of a single measurement for plates 25 and 28.

The rise in brightness near $\lambda = 425 \text{ m}\mu$ for Aristarchus is reminiscent of the luminescence band observed for this crater by Kozyrev /8/ and Dubois /9/. Let us now estimate the intensity of this luminescencelike emission in terms of a quantity ε , defined as

$$\varepsilon = \frac{\rho_{\lambda=425} - \rho_{\lambda=550}}{\rho_{\lambda=550}}.$$

Although ε was measured for a few phases only, Figure 8 shows that this parameter definitely varies with the phase.

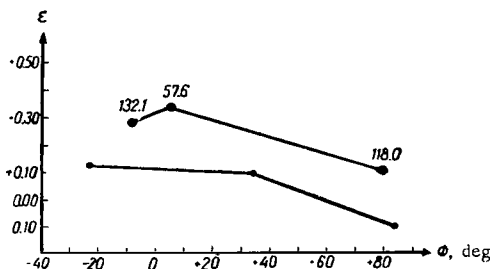


FIGURE 8. Radiation intensity as a function of phase angle for Aristarchus, at $\lambda = 425 \text{ m}\mu$

It would be interesting, too, to establish the relation between ε and the intensity of the corpuscular radiation of the sun. The double circle surrounding some of the points in Figure 8 indicates that the spectrogram was obtained during the active period of a magnetic storm. The numbers on the curve give the amplitude of the horizontal component of the geomagnetic field, according to the data of the Demidov Magnetic Station of the Institute of Geological Sciences of the UkrSSR Academy of Sciences. It would seem that the corpuscular flux responsible for the magnetic storm also produced a rise in the brightness of Aristarchus in the $425\text{-m}\mu$ wavelength region.

This phenomenon is apparently due to luminescence of the rocks covering the floor and walls of Aristarchus. The luminescence increases as full moon approaches. In addition, there is a correlation between the luminescence intensity and the corpuscular radiation of the sun. The observed luminescence bands are about $20 \text{ m}\mu$ wide, with intensity maxima near $\lambda = 425$ and $505 \text{ m}\mu$.

It should be noted that many terrestrial minerals luminesce when exposed to ultraviolet radiation. Irradiation of these by an electron flux increases the luminescence intensity. The luminescence band of scheelite (CaWO_4 , calcium tungstate) is very similar to the $\lambda = 425 \text{ m}\mu$ luminescence band obtained by us for Aristarchus. It is possible that this mineral is one of the component parts of the rocks covering the surface of this crater.

Some conclusions can now be drawn.

1. An examination of our spectrograms (about 500 were obtained) showed that no gas efflux was observed in the Alhazen, Alphonsus, Arzachel, Ptolemaeus, Messier, Linné, Hyginus, Plato, Tycho, Aristarchus, Herodotus, and Schickard Craters.

2. The similarity between the curves of the spectral brightness coefficients for lunar objects and for basalt tuff leads to the conclusion that the surfaces of the craters studied are covered with rocks which are close in their spectral characteristics to basalt tuff.

3. The individual features of the craters (floor, central peak, and walls) do not differ much in spectral reflectivity. The greatest difference is observed for Alphonsus, where the difference between the yellowness indexes for the central peak and the floor is as high as $0^m.12$.

4. The surface of Aristarchus is composed of rocks capable of luminescence. Two luminescence bands were identified, with intensity maxima near $\lambda = 425$ and $505 \text{ m}\mu$. It should be noted that the mineral scheelite (CaWO_4) has a similar luminescence band near $\lambda = 430 \text{ m}\mu$.

5. It is likely that the luminescence of Aristarchus is caused by the ultraviolet radiation of the sun, which follows from the dependence of the luminescence intensity on the phase angle. A second agent causing the luminescence of lunar rocks may be the solar corpuscular flux. The intensity of emission is increased considerably by corpuscular streams.

In conclusion, let me express gratitude to my scientific mentor, Academician N. P. Barabashov, for the valuable advice which he rendered during the course of this work.

REFERENCES

1. SYTINSKAYA, N. N. Absolyutnaya fotometriya protyazhennykh nebesnykh ob'ektov (Absolute Photometry of Extended Celestial Objects).—Izdatel'stvo Leningradskogo universiteta. 1948.
2. BARABASHOV, N. P. and V. I. EZERSKII.—Izvestiya komissii po fizike planet, No. 3:50–55. 1961.
3. FEDORETS, V. A.—Trudy Astronomicheskoi observatorii pri Khar'kovskom Gosudarstvennom universitete, 2(10). 1952.
4. KRINOV, E. L. Spektral'naya otrazhatel'naya sposobnost' prirodnykh obrazovaniy (Spectral Reflectivity of Natural Formations).—Izdatel'stvo Akademii Nauk SSSR. 1947.
5. BARABASHOV, N. P. and A. T. CHEKIRDA.—Izvestiya komissii po fizike planet, No. 1:5–39. 1959.
6. WILSING, J. and J. SCHEINER.—Publ. Astr. Obs. Potsdam, Vol. 24, No. 77. 1921.
7. SHARONOV, V. V.—Vestnik Leningradskogo universiteta, seriya matematiki, No. 1, p. 155–167. 1956.
8. KOZYREV, N. A.—Izvestiya Krymskoi astrofizicheskoi observatorii, Vol. 16:148–158. 1956.
9. DUBOIS, J.—Rospravy Ceskoslovenske akademie, Vol. 6, 16. 1959.

A.N. Sergeeva

SPECTRAL STUDIES OF THE LUNAR SURFACE

This article presents the results of spectral studies of some lunar objects. The apparatus and procedure used have been described in a previous paper /1/.

The observations were made using an ISP-22 spectrograph mounted at the focus of a spherical mirror and supplied through a precision coelostat. The dispersion of the spectrograph was $6.5 \text{ m}\mu/\text{mm}$ at $\lambda = 500 \text{ m}\mu$, and the photographs were taken on Agfa Spectral Platten Rot Rapid with exposures of 15 to 30 sec and on Astro Agfa plates with exposures of 2 min, for a spectrograph-slit width of 0.75 mm.

One $9 \times 12 \text{ cm}$ plate contained four spectra of lunar features and the spectrum of the moon obtained through a step reducer. While photographing the spectrum through the step reducer, the lunar image was continually moved back and forth across the slit by shifting the key parallel to the declination. This ensured a uniform illumination of all the steps.

TABLE 1

Section no.	$\lambda, \text{m}\mu$	Section no.	$\lambda, \text{m}\mu$	Section no.	$\lambda, \text{m}\mu$
1	650	10	525	19	425
2	620	11	514	20	420
3	615	12	493	21	411
4	605	13	480	22	406
5	592	14	472	23	392
6	580	15	464	24	379
7	568	16	456	25	369
8	563	17	449	26	354
9	545	18	436	27	343

For a comparison of the intensities of different lunar formations, the spectrum of one selected lunar feature was photographed on each exposure of each plate; the feature chosen was Menelaus Crater plus the adjacent part of Mare Serenitatis. The photometry was carried out by scanning the plates transversely with respect to the spectrum dispersion. An MF-4 microphotometer was used, at 15 to 27 different wavelengths.

Table 1 lists the numbers and wavelengths of the spectrogram cross sections. Each cross section was scanned with the microphotometer over the entire plate, that is, over three spectra: 1) the spectrum of the lunar details studied, 2) the standard-area spectrum, and 3) the step-reducer spectrum of the moon. A characteristic curve was plotted for each cross section, and then this curve was used to convert the microphotogram into an intensity curve.

TABLE 2

No.	Lunar formation	Plate number and type	Date and time of observation (UT)	Lunar phase
1	Menelaus (1, 2, 3, 4, 5)	{ No. 1 Rot Rapid	1958, Oct. 28-29 9 ^h 10 ^m —11 ^h 00 ^m	0.99
2	Aristarchus (1, 2)			
3	Grimaldi (1, 2, 3, 4, 5, 6)			
4	Tycho (1, 2, 3)	{ No. 2 Rot Rapid	The same	"
5	Plato (1, 2, 3, 4)			
6	Area between Vieta and Gassendi (1, 2, 3)			
7	Menelaus (1, 2, 3, 4)	{ No. 3 Rot Rapid	The same	"
8	Mare Imbrium (1, 2, 3, 4)			
9	Copernicus (1, 2, 3, 4)			
10	The Apennines (1, 2, 3)	{ No. 4 Rot Rapid	The same	"
11	Menelaus (1, 2, 3, 4)			
12	Sinus Iridum (1, 2)			
13	Area northwest of Mare Nectaris (1, 2, 3)	{ No. 5 Rot Rapid	The same	"
14	Mare Vaporum (1, 2)			
15	Menelaus (1, 2, 3, 4, 5)			
16	Walter (1, 2)	{ No. 6 Rot Rapid	The same	"
17	Ray of Tycho (1, 2, 3)			
18	Mountaineous region in south (1, 2, 3)			
19	Menelaus (1)	{ No. 7 Astro Agfa	1959, Oct. 18 8 ^h 40 ^m —8 ^h 50 ^m	0.96
20	Mare Crisium (1)			
21	Area north of Mare Nectaris (1, 2, 3)			
22	Mare Serenitatis and Lacus Somniorum (1, 2, 3)	{ No. 8 Astro Agfa	1959, May 23 10 ^h 05 ^m —10 ^h 15 ^m	0.98
23	Menelaus (1, 2, 3, 4, 5)			
24	Grimaldi (1, 2, 3, 4, 5, 6)			
25	Copernicus (1, 2, 3, 4, 5, 6)	{ No. 9 Astro Agfa	1959, May 23 10 ^h 20 ^m —10 ^h 30 ^m	"
26	Kepler (1, 2, 3, 4)			
27	Menelaus (1, 2, 3, 4, 5, 6)			
28	Tycho (1, 2)	{ No. 10 Rot Rapid	1959, Oct. 18 9 ^h 10 ^m —9 ^h 15 ^m	0.96
29	Mare Serenitatis (1, 2)			
30	Mare Nubium (1, 2)			
31	Mare Crisium (1, 2)	{ No. 11 Rot Rapid	1959, Oct. 18 9 ^h 20 ^m —9 ^h 30 ^m	0.96
32	Aristarchus (1, 2, 3, 4)			
33	Grimaldi (1, 2, 3, 4)			
34	Copernicus (1, 2, 3, 4)	{ No. 12 Rot Rapid	1959, Oct. 18 9 ^h 00 ^m —9 ^h 05 ^m	"
35	Kepler (1, 2, 3)			
36	Tycho (1, 2, 3, 4, 5)			
37	Ray of Tycho (1, 2, 3, 4, 5)	{ No. 1 Rot Rapid	The same	"
38	Mare Vaporum (1, 2, 3, 4, 5, 6, 7)			
39	Menelaus (1, 2, 3, 4, 5)			
40	Mare Humorum (1, 2, 3, 4, 5)	{ No. 2 Rot Rapid	The same	"
41	Mare Imbrium (1, 2, 3)			
42	Mare Tranquillitatis (1, 2, 3, 4)			
43	Mare Crisium (1, 2)	{ No. 3 Rot Rapid	The same	"
44	Aristarchus (1, 2)			
45	The Apennines (1, 2)			
46	Plato (1, 2, 3, 4)	{ No. 4 Rot Rapid	The same	"
47	Menelaus (1, 2, 3)			

TABLE 2 (continued)

No.	Lunar formation	Plate number and type	Date and time of observation (UT)	Lunar phase
48	Mare Crisium (1, 2, 3, 4, 5)	{ No. 13 Rot	1960, Oct. 5 7 ^h 45 ^m —7 ^h 55 ^m	1.00
49	Aristarchus (1, 2, 3, 4, 5)			
50	Plato (1, 2, 3, 4, 5, 6, 7, 8, 9, 10)	{ No. 14 Rot	1960, Oct. 5 8 ^h 10 ^m —8 ^h 20 ^m	"
51	Grimaldi (1, 2, 3, 4, 5, 6)			
52	The Apennines (1, 2, 3, 4, 5)	{ No. 15 Astro	1960, Sept. 5 10 ^h 05 ^m —10 ^h 15 ^m	"
53	Menelaus (1, 2, 3, 4, 5, 6, 7, 8)			
54	Mare Crisium (1, 2, 3, 4)	{ No. 15 Agfa	1960, Sept. 5 10 ^h 05 ^m —10 ^h 15 ^m	"
55	Aristarchus (1, 2, 3)			
56	Menelaus (1, 2, 3)			

From the 15 to 27 intensity cross sections we plotted curves of the spectral brightness distribution for selected lunar features. Then, at a wavelength of 545 m μ for the Rot Rapid plates and at $\lambda = 407$ m μ for the Astro Agfa plates, the intensities of all the curves were reduced to a common value. As a standard brightness distribution we chose the distribution in the spectrum of the Mare Serenitatis region near the edge of Menelaus.

We wish to emphasize that the requirements for precision photographic photometry were observed during photography of the spectra and during the photometric processing. The step-reducer spectrum of the moon was photographed under the same conditions and on the same plate as the lunar features studied. This eliminated completely any possible errors due to parasitic polarization of light in the instruments [2]. All the subsequent photographic and photometric processing was identical for the spectra of the lunar formations and for the step-reducer spectrum of the moon, since the photometric cross sections at each wavelength were made simultaneously over all the spectra present on the given plate.

A total of 56 spectrograms of various lunar formations were processed, and two hundred lunar features were identified on these spectrograms. Table 2 lists these lunar features, the number and type of plate, the date and time of observation, and the lunar phase. The serial numbers of the lunar features on the given spectrum are given in parentheses following the name of the region photographed. This numeration coincides with that in Table 3.

Figures 1 and 2 show photographs of the moon on which the positions of the spectrograph slit for the various cases are marked. The numbers near each slit position correspond to the serial numbers in Table 2.

This investigation was designed to detect the color contrasts for different lunar features. To do this, at each wavelength we calculated the deviations (in percent) of the intensities of the lunar features studied from the intensity of the standard area. When the spectrum of the standard area did not appear on the plate, the deviation was calculated relative to the arithmetic mean intensity of all the lunar features at each wavelength on the given plate. The intensity of the standard area or the mean intensity for all the features on the plate at the same wavelength was taken as 100 % in every case.

The results of these calculations are collected in Table 3, which contains data for 15 plates. The first column gives the wavelengths of the micro-photometric sections, and subsequent columns show the color shadings of

the different lunar formations expressed as percentages of the intensity of the standard area. Four spectra appear on each plate, and from 2 to 7 or 9 lunar features can be distinguished in one spectrum.

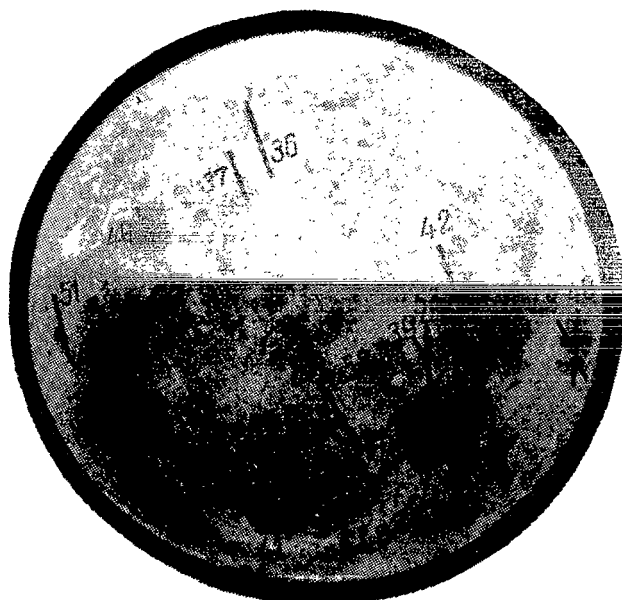


FIGURE 1

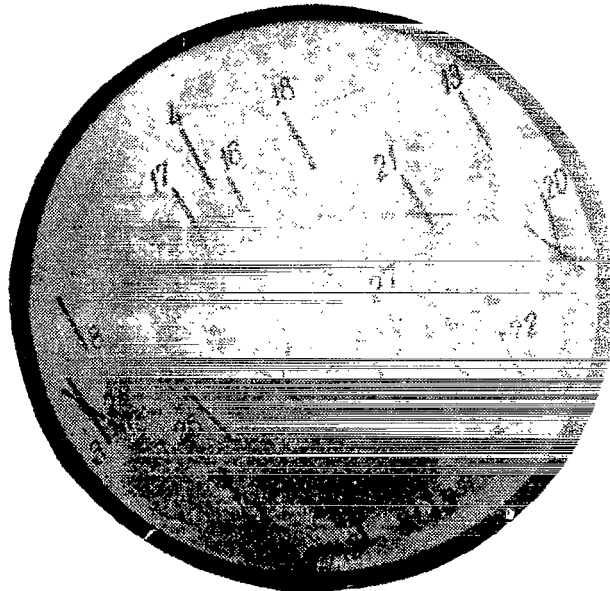


FIGURE 2

TABLE 3
Plate No. 1

Lunar features $\lambda, m\mu$	1	2	3	4	5	1	2	1	2	3	4	5	6
650	-1	-3	+6	0	0	-12	-14	+3	+3	+9	+5	+4	+4
620	+5	-2	-7	0	+5	-11	-15	+11	+7	+8	+9	+9	+7
605	+3	-3	+3	0	+3	+4	-10	+12	+8	+12	+12	+16	+14
580	-4	-2	-2	0	+2	+5	-4	+3	-5	-4	-4	-4	-3
563	-2	-1	-2	0	+2	+5	0	+1	-3	0	-3	-1	-1
545	0	0	0	0	0	0	0	0	0	0	0	0	0
514	0	-2	-1	0	-3	-1	-4	-2	-1	-1	-6	-2	-5
493	0	0	-1	0	-4	-3	-10	-2	0	-1	-6	-2	-5
480	+1	0	0	0	-5	-2	-10	-1	+1	-4	-6	-3	-8
464	-3	+3	+2	0	0	+2	-8	+1	+2	-1	+3	-1	-1
449	-2	-1	-2	0	-2	0	-10	-3	-2	-7	-7	-6	-8
436	-1	0	+2	0	-3	+2	-7	+2	-1	-3	-2	-1	-1
420	+1	0	0	0	-3	+4	-5	+3	+3	-2	-2	-1	-1
406	-1	0	0	0	-4	+2	-6	0	0	-6	-3	-3	-3
392	+3	+6	+3	0	-4	+8	-4	+6	+6	-1	+2	+1	+1
379	+4	+3	+3	0	-2	0	8	-7	-11	-10	-10	-10	-10
369	-1	-2	-1	0	-6								

Plate No. 2

Lunar features $\lambda, m\mu$	1	2	3	1	2	3	4	1	2	3	1	2	3	4
650	+11	+2	+2	+3	+1	-3	-6	+8	0	+1	0	+2	+3	+1
620	-6	-7	-6	-8	-8	-7	-6	+1	-6	+8	0	+1	+1	-4
605	+1	-6	-2	0	-4	-3	+1	+12	-9	+4	0	+4	+8	-8
580	-3	-2	-4	-1	-8	-4	-3	+2	-4	+1	0	+1	+2	-2
563	+5	+3	+3	+5	-3	-2	+1	+2	+3	-3	0	+2	-1	+2
545	0	0	0	0	0	0	0	0	0	0	0	0	0	0
514	-2	-6	-3	+1	-1	0	+5	-1	-1	+4	0	+3	+5	+1
493	-2	+1	+1	+3	+1	0	+5	+1	0	+3	0	+1	+3	-1
480	+1	-4	-4	-4	-5	-2	+1	-2	-2	+5	0	-2	0	-3
464	-6	+6	+7	+6	-2	-2	+1	+5	+1	-1	0	1	0	-1
449	-2	+1	0	+1	-6	-2	-3	+8	-1	+2	0	+1	0	+1
436	-5	+3	+3	+1	-12	8	-7	+6	-2	+4	0	-2	-2	-4
420	+1	+3	+2	+3	-9	-6	-4	+4	0	+2	0	-5	-4	-6
406	+5	+3	+5	+3	-5	-3	-2	+5	+2	+2	0	-5	-3	-7
392	+9	+5	+5	+7	-2	0	+5	+10	+5	-5	0	+2	0	-3
379	+9	+6	+6	+8	-3	+4	+5	+10	+6	-4	0	0	+5	-2

Plate No. 3

Lunar features $\lambda, m\mu$	1	2	3	4	1	2	3	4	1	2	1	2	3	4
650	+6	+2	+5	+5	-4	-2	-4	0	+4	-8	0	-6	0	-6
620	+3	+4	+10	+9	-3	+3	-5	-3	+2	+1	0	-2	0	-3
605	-	-	-	-	-	-	-	-	-	-	-	-	-	-
580	-1	+3	+1	-2	+2	+2	+4	0	+2	+4	0	+4	+2	+1
563	-1	+2	+1	0	+2	+3	+2	+1	-1	-1	0	-8	-4	-5
545	0	0	0	0	0	0	0	0	0	0	0	0	0	0
514	+5	+3	+5	+2	+3	+4	+3	+6	+3	+5	0	+5	+2	+3
493	+2	+3	+5	+6	+4	+3	+6	+5	+1	+2	0	+4	+1	+4
480	+4	0	+5	+2	+7	+5	+4	+2	-4	-9	0	0	0	-4
464	-5	+2	-1	+1	-3	+6	+4	+2	-1	+2	0	+5	+5	+6
449	-7	0	-1	+1	+2	+4	+2	+1	-1	-1	0	-1	+1	+3
436	-5	-4	-4	0	+4	+4	+1	-2	-1	+2	0	+4	+4	+6
420	+2	+10	0	0	-2	-2	+2	0	-3	+2	0	+2	+2	+2
406	+5	+2	+2	+7	+2	+4	0	0	-1	-2	0	+4	+4	-1
392	+6	+6	+1	+3	+5	+6	+1	+1	+5	+3	0	+2	+6	+5
379	+1	-1	-2	+4	0	-1	-7	-2	+3	-7	0	-2	+2	-4

Plate No. 4

Lunar features $\lambda, m\mu$	1		1		2	3	1	2	1	2	3	4	5
	1	2	1	2	3	1	2	1	2	3	4	5	
650	+13	0	-1	-8	0	-7	-1	0	-6	-3	+2	+1	
620	+4	+2	0	-2	0	+2	-1	0	-7	-3	-1	-3	
605	-4	+2	+3	+4	+2	+8	+3	0	+2	+2	+3	-2	
580	+6	-3	0	-1	+3	+2	-1	0	+1	0	+5	+3	
563	+7	+2	+2	-1	+2	0	+2	0	+1	+2	+5	+2	
545	0	0	0	0	0	0	0	0	0	0	0	0	
514	+2	-1	-1	0	+6	+2	+3	0	+3	+3	-8	-1	
493	+2	+1	0	-1	+1	-1	+3	0	+3	+1	-5	-6	
480	0	+2	+3	0	-7	-2	-5	0	-2	-1	+4	+3	
464	-6	-5	-3	-4	0	+5	-1	0	-2	+1	+1	-1	
449	0	-4	-1	-1	-2	+2	-6	0	+4	+2	+7	+4	
436	-6	-6	-3	-1	0	+2	-4	0	+4	+3	+3	+5	
420	+2	-1	+5	+2	+2	+3	-6	0	+3	+2	+2	0	
406	+2	0	+5	0	+3	+4	-6	0	+3	0	-2	-4	
392	+2	+2	+4	+2	+4	0	-7	0	+2	0	0	-4	
379	+5	0	+5	+5	+2	+6	+10	0	+4	0	0	-6	

Plate No. 5

Lunar features $\lambda, m\mu$	1	2	1	2	3	1	2	3	1
	1	2	1	2	3	1	2	3	1
650	-1	0	-8	-2	-1	+2	+2	0	+8
620	-	-	-	-	-	-	-	-	-
605	+2	0	-2	+3	-2	-1	-3	0	-
580	+2	0	+4	+7	-1	+5	+4	0	-
563	-2	0	+1	+3	0	+2	+3	-4	+1
545	0	0	0	0	0	0	0	0	0
514	+6	0	-2	-2	0	-7	-1	+1	-6
493	-2	0	-2	-1	0	+2	+2	0	-1
480	-5	0	-1	+5	+2	0	+2	-5	+1
464	-3	0	-2	+2	0	-4	-3	-1	-2
449	-4	0	-2	+7	-1	+2	+4	-3	0
436	-5	0	-4	+2	-5	-3	-1	-8	-2
420	-2	0	+1	+7	+2	+1	+4	+1	+2
406	-1	0	-2	+5	+5	-1	+3	-1	+3
392	-3	0	0	+7	+4	0	+5	-4	+2
379	-4	0	-4	+5	-1	+7	+4	-4	0

Plate No. 6

Lunar features $\lambda, m\mu$	1	1	2	3	1	2	3	1	2	3	4	5
	1	1	2	3	1	2	3	1	2	3	4	5
650	-4	+12	+10	-	-1	0	+12	-9	-10	-8	-16	-
620	+6	+11	+5	+13	0	+2	+1	-1	-9	-7	-7	-16
615	+5	+11	+9	+11	+2	+1	+4	-3	-6	-8	-13	-12
605	+3	+10	+2	+9	+2	0	-1	-1	-6	-5	-13	-12
592	+4	+4	+2	+11	+2	+2	+4	-2	-4	-4	-8	-12
580	+1	-2	+2	+1	-1	+1	+4	+1	0	0	-2	-3
568	+3	-1	-2	+1	-3	-1	+1	+3	+1	0	+1	-2
563	0	-2	0	-2	0	+2	-2	-2	+2	+2	+1	+4
545	0	0	0	0	0	0	0	0	0	0	0	0
525	-4	+4	+1	+1	-1	+1	-2	-4	-1	0	+3	+3
514	+1	+3	-1	0	0	-1	-1	0	-1	+4	-1	+1
493	+2	+1	+1	+2	-4	-1	-1	0	-1	+4	+1	0
480	0	-5	-5	-4	-3	-4	+1	0	-2	-3	0	-1
464	-5	-3	-3	-3	-4	0	-1	0	-2	+3	0	-1
449	-9	-6	-11	-6	-7	-8	-4	0	-1	+2	+3	+5
436	-12	-3	-5	-1	-5	-5	-7	0	-3	-4	-4	-5
420	-2	+3	+5	+2	+3	+3	-2	0	0	-3	-1	-2
406	+2	+6	+8	+7	+3	+2	-1	0	+3	+5	+3	-2
392	+2	+12	+10	+12	+6	+5	-3	0	+4	-2	+3	+1
379	0	+14	+15	+14	+2	+3	-7	0	+7	+5	+4	0
369	-10	+3	0	-5	-2	-2	-8	0	+3	-1	-4	-

Plate No. 7

Lunar features $\lambda, m\mu$																									Mean 1	% of mean 1
	1	2	3	4	5	6	1	2	3	4	5	6	1	2	3	4	1	2	3	4	5	6				
620	-5	-11	-3	-12	-11	-5	0	-6	+2	0	+6	+4	+11	-3	+4	+6	+7	+6	+9	0	+11	+13	40	± 7.8		
615	-9	-9	-8	-7	-	-1	-1	-6	-	-	+10	+6	+8	+9	+2	+3	+8	0	-7	0	+10	+7	42.5	± 7.0		
605	-1	-3	-1	-3	0	+2	0	-8	-	-	0	+1	+9	-7	+1	-3	+3	+6	+5	-1	+1	+1	45.5	± 4.0		
592	+2	+3	+2	+2	+3	+4	+3	+3	-1	-	-4	-4	+5	+4	+3	-9	-5	-4	-4	-7	-10	-3	51	± 4.5		
580	+2	+3	0	0	0	-2	-2	-1	-2	-3	0	+8	+4	0	+2	+6	+6	+1	+3	-1	0	+4	46	± 3.8		
568	-3	+4	+5	+6	-2	+3	+3	-5	+1	+1	+4	+3	+5	-4	+4	+6	+1	+3	0	-3	-4	+2	50.5	± 4.0		
563	-4	+2	+1	0	0	-2	+3	-1	0	-1	+4	-2	0	-4	+1	-2	+1	0	0	-6	+4	+6	48	± 3.1		
545	0	0	0	0	0	0	0	0	0	0	0	0	0	0	0	0	0	0	0	0	0	0	50	0		
525	+1	-2	+2	+1	+1	-5	-1	-2	-2	-3	+4	+1	0	-4	+1	+4	+3	+1	+1	-1	+3	-1	50.5	± 2.6		
514	+6	+4	+6	+1	0	+4	+1	-1	-4	-	0	+4	-4	-6	+1	0	-5	-2	-5	-5	-4	-3	55	± 3.8		
493	+3	-3	-2	-5	-4	0	+1	-4	+2	-	+7	+3	0	+6	+2	+5	+1	+3	0	-2	+3	0	57	± 3.3		
480	+1	-1	+5	-2	+1	+3	-2	-5	+1	+1	+3	+10	+1	-5	0	+4	-4	-4	-5	-4	-3	55.5	± 3.8			
472	+2	0	-3	-1	+2	+2	-1	-3	-	+1	+5	+6	+1	-7	-	0	-2	-4	-4	-4	0	52	± 3.3			
464	0	-4	+3	-2	-5	-4	+2	-5	-	-	+2	+3	-2	-5	+4	0	-4	-4	-4	-2	+2	0	52	± 3.3		
456	-1	-2	-1	-4	-6	-4	-3	-4	-1	-1	+3	+13	+4	-6	+2	+3	-2	-8	-1	-2	0	+1	54	± 4.3		
449	-2	-2	-6	-4	-2	0	-7	-1	-	-	+5	+4	0	-6	-2	-2	+1	+3	-2	+1	+5	+7	53	± 4.0		
436	-4	-4	-3	-4	-4	0	-2	-1	-1	-1	+4	+8	+1	-3	+2	+3	-4	+7	+2	+1	0	+5	56	± 3.4		
425	-3	-4	-4	-4	-4	-2	+1	-3	-	-	+4	+1	+4	-2	+4	+2	-3	+7	+3	+1	-1	+8	56.5	± 3.7		
420	-4	-8	0	-4	-3	+2	-4	-2	-	-	+3	0	+2	-1	+8	-9	-4	0	-3	+4	+1	58	± 4.1			
411	+1	-1	0	-10	-9	-8	+4	-2	-	-	+4	-2	0	+3	+12	+3	-1	-3	-2	-4	+1	+3	57	± 5.0		
406	-6	-4	0	+2	0	+2	-4	-1	-	-	-	-	0	-4	+4	+6	-7	-5	-3	0	-4	+3	67	± 3.9		
392	-4	-3	+2	+3	-1	0	-3	-1	+6	-	-	-	+1	-2	+4	+7	-3	+2	0	-3	-8	-	58.5	± 3.4		

Note: Column 23 gives the mean intensity for 22 lunar details. Column 24 gives the rms error, in percent of the mean intensity.

Plate No. 8

Lunar features $\lambda, m\mu$	1		2		1		2		1		2		1		2	
	1	2	1	2	1	2	1	2	1	2	1	2	1	2	1	2
480	-	-	-	-	-	-	-	-	-	-	-	-	-	-	-	-
464	+12	+14	0	0	-3	-3	-4	+1	-	-	-	-	-	-	-	-
456	-8	0	0	+2	-2	+1	-5	-3	-	-	-	-	-	-	-	-
449	-2	0	0	0	-5	-4	-4	-2	-	-	-	-	-	-	-	-
436	0	0	0	+5	+6	-2	+4	-1	-	-	-	-	-	-	-	-
425	-5	0	0	0	+4	0	+4	0	-	-	-	-	-	-	-	-
420	0	-3	0	0	+3	-1	+3	0	-	-	-	-	-	-	-	-
406	-8	-5	0	-4	-4	-8	-5	-8	-	-	-	-	-	-	-	-
392	+2	+4	0	+1	+6	-1	-1	-3	-	-	-	-	-	-	-	-
379	-4	+6	0	-2	-4	-6	-7	-7	-	-	-	-	-	-	-	-
369	+13	+14	0	-3	+7	-2	+4	+4	-	-	-	-	-	-	-	-
354	+8	+19	0	+3	+17	+17	+14	+17	-	-	-	-	-	-	-	-
343	-	-	0	+2	+11	+10	+7	+9	-	-	-	-	-	-	-	-

Plate No. 9

Lunar features $\lambda, m\mu$	1				2				3				4				5			
	1	2	3	4	1	2	3	4	1	2	3	4	1	2	3	4	1	2	3	4
480	0	0	0	-7	-10	-4	-14	-11	-10	0	-4	-18	-18	+3	-7					
464	+17	+19	0	+17	+11	+6	+7	+9	-2	+2	+1	-2	0	0	+2					
456	+5	+8	0	+6	+1	-1	0	+1	-7	-3	-2	-10	-4	-5	-5					
449	-4	-4	0	-2	-3	-3	-4	0	-7	-8	-3	10	-8	-7	-7					
436	+10	+11	0	+5	+9	+3	+2	+5	+2	+4	+8	-2	+1	+6	+3					
425	0	0	0	0	0	0	0	0	0	0	0	0	0	0	0					
420	+8	+7	0	+6	+6	+4	+1	+3	+5	+9	+8	-2	+1	+6	+2					
406	+11	+10	0	+14	+6	+5	+2	+4	+8	+9	+23	-1	+1	+10	0					
392	-3	-1	0	+5	+5	+11	+7	+10	-3	-3	+4	-10	-9	-5	-9					
379	+6	+11	0	+10	+6	+1	-2	0	+4	+2	+9	-3	+1	+1	-3					
369	+13	+7	0	+8	+9	+4	-2	0	+9	+4	+8	-4	+2	+2	+2					
354	-	-	0	+26	+11	+2	+2	0	+4	+4	+8	-2	-1	+1	+2					

Plate No. 10

Lunar features $\lambda, m\mu$	1	2	3	4	5	1	2	3	4	5	1	2	3	4	5	6	7	1	2	3	4	5
	1	2	3	4	5	1	2	3	4	5	1	2	3	4	5	6	7	1	2	3	4	5
650	-8	-7	-1	-8	+1	-5	+1	+10	+8	-2	-3	-5	-5	-7	-5	-2	+5	-2	+2	-8	-12	-8
620	-15	-5	+2	-4	+4	-2	+5	-1	-	-	-1	-3	-3	0	0	-1	+1	+4	-11	-3	-6	-7
615	-7	-4	-1	-4	-2	-2	-4	-11	-5	-8	0	-3	-4	-1	0	+3	+1	+5	-12	-5	-5	-3
605	-2	-1	-1	-3	-1	-1	-4	-8	-2	-3	+3	+1	-2	-2	+2	+4	+2	+2	-4	-3	-5	-8
592	-8	-1	-4	3	0	-4	-4	-1	-3	-3	-2	-1	-2	-2	+2	+4	+2	0	-4	-4	-7	-6
580	-3	-1	0	+1	+1	-4	-3	-6	-1	-7	+2	+1	-3	0	0	0	-2	0	-6	-4	-5	-8
568	-4	-8	-4	-5	-4	-7	-4	-6	-	-2	-1	-5	-5	+2	-1	0	0	0	-2	-9	-5	-6
563	+1	-8	-2	-1	-3	-1	-2	+1	-2	-	+3	+2	+3	+5	+6	+3	+1	0	+1	-6	-1	0
545	0	0	0	0	0	0	0	0	0	0	0	0	0	0	0	0	0	0	0	0	0	0
493	-8	-10	-9	-8	-6	+1	-1	+3	0	-2	+5	+4	0	+4	+1	+4	+4	+2	-4	+2	+3	+5
480	-3	-11	-6	-8	-5	0	-1	-2	+5	+4	-4	0	-5	-4	-5	-1	0	0	+1	-2	0	+2
472	-8	-10	-10	-10	-6	-3	0	+1	+2	+1	-1	-1	-3	-3	-4	+1	0	0	+5	-1	+1	+5
464	0	-6	-8	-2	-1	-3	+3	+5	+4	+4	+6	-6	-7	-1	0	+2	-1	0	+3	+6	-8	+6
456	-1	-8	-8	-4	-5	-4	0	0	-1	-1	+1	-1	-3	-2	-4	-2	-3	0	+4	-1	0	+4
449	-5	-8	-7	-1	-1	+2	-1	-5	+2	-1	0	+2	-6	-1	+2	+6	+6	0	-1	0	+3	+4
436	+1	-1	-1	+10	+2	+2	+5	+2	+4	+4	-2	+1	+2	+2	+2	+7	-2	0	+4	+3	+7	+7
425	-5	-11	-9	-6	-5	-2	-6	-5	-5	-8	-8	-2	-6	-7	-2	-4	-4	+2	-2	+1	-6	+4
420	-4	-9	-12	-5	-3	-2	-4	-1	-2	-4	-	-4	-6	-3	-3	-4	-1	0	+2	+1	+4	+3
411	-5	-2	-4	0	-1	+1	-2	-5	-2	-5	-4	-2	-5	-3	+4	+7	+2	0	+2	0	+1	+4
406	+4	+2	+7	+6	+9	+4	+4	+7	+7	+5	-6	-1	-4	-4	-4	-1	0	0	+3	+1	+4	+7
392	-1	+2	+3	-2	+3	-2	+3	-2	+3	+8	+1	+1	-3	-2	-1	+5	+2	0	+7	+3	-8	+8
379	+10	+4	+2	-3	-2	+3	+3	+10	+4	+2	0	-	-	-5	+1	-1	+2	0	+3	0	-1	-2
369	-4	+1	+1	+2	+3	+9	+1	+8	+3	+2	+2	+4	-1	0	+1	-2	-1	0	+1	+7	+5	+2
354	0	-5	+7	+1	+2	-	+8	+11	+5	+5	-8	-4	-	-1	-8	-6	+1	0	0	+4	+1	-4
343	+5	-	-	-	-	-	-	-	-	-	-	-	-	-	-	-	-	0	0	-	-	-

Plate No. 11

Lunar features $\lambda, m\mu$																	
	1	2	3	4	5	1	2	3	1	2	3	4	1	2			
650	+3	+6	+8	+1	+12	-	-	+6	0	-4	-2	-9	-10	-11			
620	-5	-2	-1	+3	+3	-4	+1	-3	+2	+4	+2	-3	+5	+1			
615	+2	+4	+2	+2	+4	+3	+5	0	+4	+1	+2	-1	-7	+1			
605	+6	-1	-1	-1	+1	+1	+2	-6	-2	0	+3	-3	+3	+3			
592	+3	-6	+4	+1	+4	-3	0	-5	+2	-3	-2	-5	+3	+2			
580	-5	+4	-1	0	-6	-6	0	-8	-1	-2	+1	-6	+1	+6			
568	+2	-5	-3	+2	-7	-4	+1	-3	0	-4	-1	-4	-1	+2			
563	+3	+4	+4	+3	-5	-4	+1	-3	0	0	0	-7	0	+3			
545	0	0	0	0	0	0	0	0	0	0	0	0	0	0			
525	-1	-1	0	+2	-3	-3	-3	-3	+2	-2	0	-2	0	+3			
514	+4	+5	+6	+4	+4	+5	+3	0	+4	+3	0	-2	-2	+3			
493	-6	-4	-4	0	-5	-3	-3	+2	+2	+1	+2	-2	+4	0			
480	-4	-5	-1	-1	-3	0	+4	0	-3	0	0	-2	+5	+3			
472	-1	-2	0	-2	-3	+4	-2	0	+2	-2	+8	0	+6	+6			
464	-3	-3	-1	0	-3	-1	+4	-3	-3	-1	-6	-2	-3	-1			
456	-3	-4	0	0	-5	-5	+1	+1	+2	-1	-7	0	0	-1	-5		
449	-4	-8	-4	-3	-1	-1	-2	0	+4	-3	-6	-1	+8	+2			
436	-4	-5	-5	-4	0	0	-3	-1	+4	-3	-6	+1	+5	+3			
425	-5	-3	-1	-3	+4	0	+1	+3	-4	-2	+12	+4	-1	-1			
420	-6	-5	-3	-1	+4	-2	0	-3	+2	-2	+11	+5	-2	-2			
411	-4	-6	-4	-4	0	+4	-1	0	-3	-5	-9	-2	+4	+2			
406	-2	-7	-4	-4	-2	+1	0	+1	-3	-3	+13	-1	-2	-5			
392	+1	-2	-3	-5	+5	-6	+4	-3	+6	-6	+15	+5	-5	-5			
379	-6	-5	-4	-5	+2	-5	-2	-3	-4	-9	+16	+5	-5	-5			
369	+4	-3	-7	-5	-3	-7	0	-2	+2	+2	+4	-1	-1	-9			

Plate No. 12

Lunar features $\lambda, m\mu$												
	1	2	1	2	1	2	3	4	1	2	3	
650	+8	-6	-	+10	-1	-3	-5	-6	-11	-6	-3	
620	+6	+2	+13	+5	-3	-2	-2	-3	-10	-5	-3	
615	+9	-5	+10	-7	-2	0	+1	-2	-12	-4	-1	
605	+5	-9	-2	-4	-2	0	-2	-2	-10	-1	-2	
592	-4	-4	-3	-1	-1	-1	+1	-3	-2	-2	-1	
580	+4	-1	-2	-1	-4	+1	-1	-1	-2	0	+1	
568	+2	+5	-2	+3	-4	+3	+1	-1	-5	+2	+2	
563	0	0	+1	+1	-4	-1	+1	-1	-4	+1	+1	
545	0	0	0	0	0	0	0	0	0	0	0	
525	-2	+1	0	-1	-3	+3	+2	+1	-2	+2	+3	
514	-5	0	-2	-1	-2	-5	+3	+1	-4	+3	0	
493	-4	0	0	+4	-2	-4	+2	0	-6	+1	+2	
480	-5	+1	-1	+3	-1	-5	-1	0	-4	+4	+2	
472	-6	-2	-1	0	-1	-4	0	-1	-1	+5	+4	
464	-8	-3	-1	0	-3	+5	-1	-2	-3	+7	+5	
456	-7	-6	-3	+3	-5	-1	+2	0	-1	+8	+9	
449	-9	-8	-1	0	0	-1	+2	0	+1	+8	+3	
436	-8	-4	-6	-4	-2	-4	-4	-1	0	+8	+5	
430	-11	-9	-5	+3	-2	-6	-3	0	-3	+6	+6	
425	-6	-7	-3	0	+2	-3	-5	-3	-3	+5	+3	
411	-9	-8	-4	+2	-3	-4	-4	-1	0	+4	0	
406	-	-7	-2	+5	-4	-6	-6	-3	-2	+7	+2	
392	-	-11	-6	+1	-3	-5	+4	-3	-4	+2	+2	
379	-	-	+1	+1	-5	-2	+5	+1	-1	+5	-3	
369	-	-	+3	-3	-2	+2	-2	-3	-6	0	-5	
354	-	-	0	+5	-6	+3	0	-2	0	-2	-2	
343	-	-	+2	+4	-6	-1	+2	0	-2	-2	0	

Plate No. 13

Lunar features $\lambda, m\mu$	1	2	3	4	5	1	2	3	4	5
650	+1	+2	+2	+3	+5	-2	-2	-2	-4	-4
620	+1	+2	+3	+4	-	-2	-2	-4	-2	-1
615	0	-1	+6	+7	+1	-1	-2	-1	-1	-5
605	+2	0	+4	-2	-2	-2	-1	-10	-2	-
592	+3	+1	+2	+3	0	0	0	+4	-3	-2
580	+1	0	-2	+2	0	+3	+3	0	-4	-2
568	-1	-2	+1	0	+7	+1	0	+3	0	-
563	-2	0	+3	+3	+3	0	-1	+2	-3	0
545	0	0	0	0	0	0	0	0	0	0
525	-1	+4	+1	-7	+4	0	-2	+4	-3	-3
514	+1	+3	+1	+1	+1	0	-1	+3	-3	-3
493	0	0	0	0	0	-1	+1	-1	0	0
480	0	-	-3	0	+6	-2	0	-3	+3	-1
472	+2	+1	-1	-1	+4	-3	-2	+2	0	-2
464	-2	0	+3	+1	+3	-3	+1	-2	-1	-2
456	+1	+2	-2	+1	+4	-1	-2	-2	-4	+1
449	+2	+2	-2	-4	+1	0	-3	+1	+2	-1
436	+1	+5	+2	-2	-2	+2	0	-1	-2	-
425	+1	+4	0	0	+3	-1	-5	+6	-5	+1
420	-4	+2	+4	-1	+2	0	-2	+4	-3	-3
411	-2	0	+1	+1	-2	0	0	-1	-8	-8
406	+5	+7	+4	-2	-2	-3	-4	-4	-	-

Plate No. 14

Lunar feat- ures																																																							
	1	2	3	4	5	6	7	8	9	1	2	3	4	5	6	1	2	3	4	5	1	2	3	4	5	6	7	8																											
$\lambda, m\mu$																																																							
650	+	1	+	5	+	7	+	4	+	1	+	1	-	4	+	1	+	3	0	+	1	-	3	-	2	-	4	0	-	2	+	2	+	4	+	2	+	1	0	0	0	+	5	-	1	-	5	-	3	-	2				
620	+	4	+	4	+	5	+	2	+	1	-	3	-	1	+	2	+	5	+	4	+	3	-	3	+	1	-	1	-	2	-	1	+	3	+	2	+	2	+	3	+	3	+	5	0	+	6	+	2	-	1	-	2	+	3
615	+	1	-	2	+	1	-	4	-	2	0	-	3	0	-	2	+	1	-	1	-	3	-	2	-	7	-	-	-	-	-	4	+	1	+	2	+	3	+	6	0	+	2	0	+	5	+	4	+	1	-	1	-		
605	+	1	+	2	+	1	-	3	-	2	0	-	5	-	1	-	3	+	2	-	1	-	7	-	4	-	10	-	11	0	+	3	+	-	1	+	2	0	-	1	+	1	0	+	3	0	+	3	+	1	-	-			
592	+	1	+	6	+	1	+	1	+	1	+	2	-	9	-	2	-	1	0	-	1	-	3	-	4	-	7	-	3	-	1	+	2	0	-	1	-	2	-	2	-	1	0	+	4	0	-	1	-	2	0	-			
580	-	1	-	1	+	2	-	1	-	+	3	-	1	+	2	+	1	-	4	-	2	-	3	-	5	-	6	-	3	-	1	0	-	1	-	1	+	1	-	3	0	0	+	1	+	1	-	3	0	+	3	0			
568	-	1	-	2	+	7	-	3	-	2	+3	-	3	-	5	+3	-	3	-	3	-	2	-	3	-	5	-	5	0	+	2	+	4	+	5	+	5	0	+	5	0	+	5	+	6	+	2	+	4	-					
563	-	2	-	6	-	2	-	4	-	3	+	1	-	6	-	2	+3	-	3	-	1	-	6	-	7	-	7	-	6	-	3	+	3	+	1	-	1	-	2	-	5	0	0	0	0	-	3	-	6	-	6				
545	0	0	0	0	0	0	0	0	0	0	0	0	0	0	0	0	0	0	0	0	0	0	0	0	0	0	0	0	0	0	0	0	0	0	0	0	0	0	0	0	0	0	0	0	0	0	0	0	0						
525	+	4	+	1	+	3	+	3	+	1	+	1	-	5	-	3	-	1	-	7	+	1	0	+	2	-	1	+	1	+	4	+	3	+	1	-	9	-	4	+	3	+	3	0	+	5	+	3	-	4	-	2	+	2	
514	+	2	+	4	+	2	-	2	-	+	7	0	0	0	+	2	-	2	+	2	+	2	+	2	+	2	-	5	+	3	+	1	-	7	-	2	+	6	+	1	0	-	2	-	+	1	-	2	-	1	-				
493	+	1	0	0	0	0	+	2	+	5	-	1	-	1	0	+	5	+	1	+	4	+	3	+	1	+	3	-	5	+	6	+	4	-	4	+	1	+	5	+	2	0	-	4	-	0	-	6	0	-					
480	-	10	-	6	-	1	-	3	-	7	0	-	4	0	-	2	0	+	1	-	3	+	3	-	6	-	5	-	-	-	1	-	1	-	3	-	1	0	+	2	0	-	5	-	3	-	4	-							
472	-	6	-	7	-	1	-	3	-	+	5	-	4	-	1	+	2	0	+	3	-	5	-	3	-	4	-	7	-	-	+	1	+	2	+	3	-	2	+	2	0	-	2	-	1	-	1	-	6	-	4				
464	0	-	4	0	-	1	+	1	+3	-	2	+	7	+3	+8	+8	+4	+2	0	0	-	7	-	1	+	4	-	3	0	-	7	-	1	+	4	-	3	0	+	4	+	3	0	+	5	+	5	-	3	+	1	+	1		
456	-	8	-	2	-	1	0	-	+	6	-	2	+3	0	0	+	3	-	5	+	3	-	7	-	4	-	11	+	6	+	4	+	7	+	9	0	0	+	2	0	+	5	+	1	-	2	0	-	1	-					
449	-	10	-	7	-	4	-	5	-	+	2	-	5	+	2	+3	-	1	+	4	-	7	-	5	-	8	-	6	-	8	-	-	-	+	3	+	4	0	+	5	+	5	+	1	+	1	-	-	-						
436	-	7	-	5	-	2	-	8	-	+	5	-	3	+	2	+	1	+	1	+	5	-	2	-	1	-	7	-	3	-	9	+	6	+	4	+	4	-	6	+	2	+	3	0	+	8	+	3	+	5	+	2	+	1	
425	-	9	-	6	-	3	-	6	-	8	-	3	-	8	0	+	1	+	8	+	5	-	1	-	3	-	6	-	3	-	9	+	8	-	-	2	+	1	+	1	+	6	0	+	6	+	9	+	2	-	7	+	3		
420	-	8	-	7	-	4	-	7	+	6	+3	-	5	+	4	+	2	+3	+10	-	2	-	2	+	1	+	2	-	6	+	9	-	-	4	-	3	+	5	+	1	0	+	10	+	10	+	1	+	3	0	-				
411	-	6	-	7	-	7	-	8	-	+	2	-	7	-	5	-	2	0	+	4	-	10	0	-	-	-	-	-	-	7	-	5	+	5	+	7	-	3	-	+	5	+	7	0	+	1	-	5	0	-					
406	-	8	-	5	-	2	-	5	-	7	-	2	-	6	+	9	-	-	2	+	7	-	7	-	4	-	4	-	4	-	5	-	1	+	3	-	3	+	10	+	5	+	10	0	+	7	+	5	+	2	-	-			

$\lambda, m\mu$	Lunar features											
	1	2	3	1	2	3	1	2	3	4		
486	+6	-6	-4	+1	-	+2	-3	+1	-	-1		
477	+6	-	-2	-	-	+2	-4	-2	-	-1		
467	0	+1	+1	+1	-4	+1	-	-	+3	+1		
456	-4	-1	-6	+7	-5	+5	-	-	+9	+7		
445	0	-1	-2	+2	-2	+1	-	-	+2	0		
437	-8	+7	-2	-6	+2	+2	-	-	0	+4		
422	-1	+11	-4	-6	-9	0	-12	-4	0	+2		
415	-3	-9	-5	-4	-5	+7	-7	-3	+13	+9		
406	0	0	0	0	0	0	0	0	0	0		
403	+1	+4	-	+2	+1	+3	-3	-3	+3	+2		
390	+8	-1	-4	+1	-4	-6	-4	-4	+6	-4		
385	-2	-3	-4	+5	-2	-3	-2	-2	+10	-2		
381	-3	-2	-8	0	-4	0	0	0	-	+2		
378	-3	-1	-7	-7	+2	-	+7	+7	+5	+3		
372	-3	-2	+3	+7	-9	-3	-2	+4	+6	-1		
368	+2	-2	-2	+6	-3	-3	-2	+2	+6	-6		
360	+3	0	-3	+3	-8	-9	+1	-1	+2	-6		
355	+3	+1	-1	+4	-6	0	+1	0	+1	+3		
350	-3	+3	-4	-2	+2	-2	+3	+3	+1	-3		
343	+1	+4	-1	+8	0	-2	+5	+3	-3	-4		
340	0	-2	-3	+2	-2	-3	+1	+2	+5	+2		
338	-5	+4	-2	-2	-2	-6	+5	+3	+2	-3		
335	+3	-6	+1	+7	-	+7	-4	-2	-	0		
332	0	0	-7	-2	-	+1	-4	-2	+2	-		

We see from these tables that the relative intensity deviations are not large. As a rule, for λ from 590 to 390 $m\mu$ they are less than 10%. For some lunar features at λ from 650 to 605 $m\mu$, however (red region), the relative deviations are as high as 15 to 18%.

The rms errors of the results in these tables are around 3%. In the red part of the spectrum this error is greater due to the low dispersion, the considerable blackening, and the rapid drop in plate sensitivity with wavelength in the H_α region. This error was calculated from spectra of Mene-la-us and the adjoining area of Mare Serenitatis photographed onto six plates during the night of 28-29 October 1958 (see Table 3). On each of the six spectrograms four or five lunar features were chosen, and their intensity deviations relative to the aforementioned standard feature (appearing in the same spectra) were calculated at all wavelengths.

The color differences obtained for some lunar features were in many cases aggravated by random errors due both to the accuracy of the procedure employed and to fluctuations in the atmospheric transparency, which are particularly pronounced in the red part of the spectrum. Consequently, since the relative deviations obtained were comparatively small, we are inclined to think that the actual color contrasts of the lunar features were too slight to be detected with any confidence using the method of photographic photometry.

In conclusion, the author extends her deepest gratitude to N. A. Yakovkin for his advice during the course of the work.

REFERENCES

1. SERGEEVA, A. N. — Byulleten' komissii po issledovaniyu Luny i planet, No. 1. 1959.
2. LIPSKII, Yu. N. — Astronomicheskii Zhurnal, Vol. 36:2. 1959.

I. K. Koval'

**ON THE STUDY OF THE OPTICAL PROPERTIES OF
THE ATMOSPHERE AND SURFACE OF MARS**

Numerous investigations of the brightness distribution along the apparent radius of Mars have led to the familiar conclusion that the continental regions of the planet are very flat spaces devoid of any relief. Therefore, various authors tried to determine the optical parameters of the Martian atmosphere and surface using formulas from the theory of light scattering in a planetary atmosphere which were derived assuming that the reflection from the underlying surface obeys Lambert's law. The observational materials used were data on the brightness distribution along the radius of the visible disk of Mars, these data having been obtained photographically with the aid of color filters.

TABLE 1

Year of observation	Author	$\lambda_{\text{eff}},$ m μ	m	Remarks
1939	Sytinskaya /5/	630	0.508	Normal astrograph, Tashkent Astr. Obs. (filter)
1950	Barabashov /6/	640	0.558	27-cm reflector, Kharkov Astr. Obs. (filter)
1952	Barabashov /7/	640	0.550	27-cm reflector, Kharkov Astr. Obs. (filter)
1954	Koval' /8/	640	0.562	20-cm reflector, Kharkov Astr. Obs. (filter)
1956	Barabashov and Koval' /3/	647	0.526	27-cm reflector, Kharkov Astr. Obs. (filter)
1961	Koval', Morozhenko, and Didychenko /9/	655	0.495	70-cm reflector, Main UkrSSR Acad. Sci. (continuum)
1963	L. Bugaenko, O. Bugaenko, Koval', and Morozhenko (see following article)	600	0.527	70-cm reflector, Main Abstr. Obs. UkrSSR Acad. Sci. (filter and photocathode)

Table 1 gives such data for several oppositions of Mars, according to measurements made by various authors in red light. Measurements in red light are used to study the Martian surface proper, since it is generally assumed that such measurements are distorted least by the Martian atmosphere. The limb darkening may be characterized by the ratio of the measured brightnesses at points with 60° and 0° angles of incidence of the light ($m = \frac{\rho_{60}}{\rho_0}$).

The considerable discrepancies between the various measurements listed in Table 1 may be due, in our opinion, to the following factors.

1. Inaccurate determination of the angles of incidence of light at the relevant points of the photographic image, particularly at the limb. This shortcoming is due to errors in determining the scale of the image.
2. The considerable influence of the photographic effect, which cannot be taken into consideration with due accuracy at the edge of the image.
3. Dilatation of the image diameter due to turbulent vibration, resulting in a substantial distortion of the measured brightness at the limb.

In addition, the method of photographic photometry of planetary disks, one stage of which entails a conversion of plate blackenings into intensities with the aid of a characteristic curve, is inherently inaccurate for our purposes.

TABLE 2

$\lambda, m\mu$	630	560	—	420	—	1939, Sytinskaya
m	0.508	0.622	—	0.900	—	
$\lambda, m\mu$	640	580	520	460	—	1950, Barabashov
m	0.558	0.580	0.544	0.711	—	
$\lambda, m\mu$	640	580	520	460	—	1952, Barabashov
m	0.550	0.590	0.660	0.730	—	
$\lambda, m\mu$	640	580	520	460	—	1954, Koval'
m	0.562	0.569	0.688	0.833	—	
$\lambda, m\mu$	647	—	530	429	—	1956, Barabashov
m	0.521	—	0.714	0.752	—	and Koval'
$\lambda, m\mu$	680	—	530	470	—	1958, Barabashov,
m	0.620	—	0.705	0.770	—	Koval' and
						Chekirda /10/
$\lambda, m\mu$	655	583	510	446	400	1961, Koval', Moro-
m	0.449	0.558	0.610	0.715	0.870	zhenko, and
						Didychenko
$\lambda, m\mu$	600	560	510	450	390	1963, L. Bugaenko
m	0.526	0.530	0.632	0.713	0.783	et al.

As an average, we have

$\lambda, m\mu$	650	600	550	500	450	400
m	0.51	0.55	0.60	0.69	0.79	0.85

It was shown in articles /1, 2/ that the variation of brightness along the apparent radius of Mars in red light is also influenced considerably by the dustiness of the Martian atmosphere; greater dustiness corresponds to higher m . At present there is no doubt that the Martian atmosphere always contains some amount of dust particles, so that the average value $m = 0.532$ for $\lambda = 640 m\mu$ given by Table 1 is not less than the true ratio for the actual surface of the planet.

Thus, according to measurements for incidence angles of $0^\circ < i < 60^\circ$, photographic photometry gives $m \approx 0.5$ for the actual surface of Mars, from which it follows that, with respect to the limb darkening at opposition, this surface is close to orthotropic. However, it is important to establish beyond doubt whether the observations made using red filters really represent the actual surface of Mars.

Investigations of the brightness distribution along the Martian intensity equator, carried out by Barabashov, Sytinskaya, Koval' and others using

light filters, produced the results in the $\lambda = 400\text{--}650\text{ m}\mu$ interval as shown in Table 2.

Thus, for Mars the steepness of the curves giving the variation of brightness with the angle of incidence decreases toward the violet end of the spectrum. This has led some authors to the familiar conclusion that the atmosphere of Mars possesses scattering properties and has a low optical thickness in this wavelength range.

Finally, let us consider the radial variation of brightness for $\lambda > 650\text{ m}\mu$. It is to be expected that the influence of the Martian atmosphere on the steepness of the limb-darkening curves for these wavelengths will be negligible, and that as a result we should be able to observe the true surface of the planet in this light. In other words, for $\lambda > 650\text{ m}\mu$ the ratio m_λ should be constant.

The large volume of observational data obtained in 1956 at Kharkov /3/ enables us to determine m for λ_{eff} values of 647, 750, and 840 $\text{m}\mu$. As observed in a previous article /2/, the ratio m for September-October 1956 increased with rising λ , and was equal to 0.642, 0.778, and 0.847 for the values of λ_{eff} studied. This result was attributed to the high dustiness of the Martian atmosphere at that time. An approximate estimate of the size of the particles gave a radius of $1.45\text{ }\mu$.

During the June-August 1956 period, the continent-mare contrast at the given λ_{eff} remained quite distinct, indicating a low dust content of the Martian atmosphere; however, in this case the condition of constant m_λ was not satisfied either. This is obvious from the average values of m given in Table 3. The table also lists the average values of the continent-mare contrast k near the center of Mars. If we assume that during true opposition $\rho_i = \rho_0 \cos^q i$, then the parameter q characterizing the observed limb darkening for Mars has the values listed in column 4 of Table 3.

TABLE 3

$\lambda, \text{ m}\mu$	m	k	q
360	0.800	0.05	0.33
429	0.725	0.09	0.47
530	0.679	0.15	0.57
647	0.578	0.28	0.81
750	0.610	0.31	0.73
840	0.649	0.31	0.63

We see that as the wavelength increases up to 647 $\text{m}\mu$ q increases, after which it drops considerably, at least up to 840 $\text{m}\mu$. At the same time, the contrast k for this period increases smoothly with wavelength and then remains constant for $\lambda \geq 750\text{ m}\mu$. Let us now attempt to explain the spectral variation of the parameters m (or q) and k .

In our opinion, two alternatives should be considered here.

1. For the actual surface of Mars the limb darkening is characterized by the values $m \approx 0.58$ or $q \approx 0.81$ (measured at $\lambda_{\text{eff}} = 647\text{ m}\mu$). The rise in m for $\lambda < 647\text{ m}\mu$ is caused on the atmosphere of Mars, which possesses such scattering properties that its optical thickness increases toward the violet. The increase in λ_m for $\lambda > 647\text{ m}\mu$ is due to the presence of a small amount of large scattering particles in the atmosphere, which are not, however, abundant enough to produce a substantial blurring of the continent-mare contrast

for $\lambda \geq 750 \text{ m}\mu$. The optical thickness of a "cloud" of these particles increases with increasing wavelength.

2. The Martian atmosphere both scatters and absorbs. The effect of the scattering component of the atmosphere decreases with an increase in wavelength and becomes negligible for $\lambda > 647 \text{ m}\mu$, while the absorbing component continues to influence the limb darkening up to $840 \text{ m}\mu$ and possibly even farther. In this case, we should take $m = 0.65$ or $q = 0.63$ for the true surface of Mars.

Let us now consider the arguments which support each of the two hypotheses. First, we shall list the observational data which must be kept in mind while examining the two alternatives.

1. The visual albedo ρ of the continents near the apparent center of Mars decreases smoothly from 0.30 at $650 \text{ m}\mu$ to 0.06 at $400 \text{ m}\mu$.

2. The continent-mare contrast near the apparent center of Mars drops from 0.40 at $650 \text{ m}\mu$ to 0.05 at $400 \text{ m}\mu$.

3. The ratio m increases smoothly with decreasing wavelength in the $400\text{--}650 \text{ m}\mu$ interval.

4. When the Martian atmosphere is clear, $\rho > 0.04$ for the maria at $400 \text{ m}\mu$.

5. The Martian atmosphere contains a suspension of coarse particles which are good scattering agents for long-wave radiation. The variation of optical thickness with wavelength for these particles is opposite in sign to that for Rayleigh scattering.

Two more important factors should be mentioned.

1. A scattering medium lowers the true contrast at the surface of the planet, since a veil blurring the surface contrast forms due to the scattering of light by atmospheric particles. Absorption, on the other hand, leads to an attenuation of the luminous intensity only. In relation to this we should define more precisely the commonly used term "violet layer." If this "layer" is regarded as a medium mainly absorbing (but not scattering) violet light, then the expression "clearing of the violet layer," which is intended to describe periods of greater contrast on Mars for observations near $400 \text{ m}\mu$, is meaningless. Actually, a "clearing" in this case would mean a local or global increase in the transparency of the "absorbing layer." For a high albedo of the true surface of Mars (0.2–0.3), the "clear" regions would appear as bright spots, whereas in the event of low albedo they would be hardly discernible. An increase in the continent-mare contrast with a constant visual albedo of the continents could be only due to a decrease (and not an increase) in the transparency of the "absorbing layer" above the maria.

If the "violet layer" is regarded as a scattering medium, then an increase in the continent-mare contrast may indeed be due to a clearing of this layer, that is, due to a temporary decrease in the density of the atmospheric haze blurring the surface contrast.

2. For a given optical thickness τ (in this case, $\tau < 1$), a scattering medium will have less influence on the steepness of the limb darkening than an absorbing medium will, since in the former case, in addition to the attenuation of light, we must consider the substantial role played by the luminosity of the atmospheric column, whose height increases toward the limb. Consequently, it follows that if the Martian atmosphere both scatters and absorbs, and if its total optical thickness increases toward the

violet while the steepness of the limb darkening decreases toward the violet, then scattering will prevail over absorption in this atmosphere.

From the preceding data the following conclusions may be drawn.

1. In order to explain the rise of the limb-darkening curves at lower wavelengths (starting with $650\text{ m}\mu$), we must assume that at any rate for $\lambda \geq 400\text{ m}\mu$ scattering prevails over absorption. The observed steep drop in the visual albedo of Mars in the violet region cannot be attributed to atmospheric effects only.

2. The assumption that the atmosphere of Mars is responsible for considerable true absorption near $400\text{ m}\mu$ is difficult to reconcile with the temporary enhancement of the continent-mare contrast at these wavelengths. The clearing of the scattering "violet layer" over dark regions of the Martian surface is easily explained by thermal factors [11].

3. The wavy variation of the visual albedo of Mars observed by Kozyrev [12], a factor which is offered as an argument in favor of the hypothesis being considered, has not been corroborated by the numerous recent measurements carried out at the Main Astronomical Observatory of the UkrSSR Academy of Sciences in 1960-1961. The latter observations also show that the ratio m_λ characterizing the steepness of the limb darkening of Mars increases smoothly (without any waviness) toward the violet. It follows from the preceding that the Martian atmosphere possesses mainly scattering properties in the visible part of the spectrum, and therefore the following points are true.

1. The distribution of energy in the visible spectrum of Mars depends mainly on the distribution of energy in the spectrum of the surface of the actual planet. In other words, the color of Mars is mainly attributable to its surface, which according to Dollfus may be covered by a powdered limonite which is orange in color. In this case, the visual albedo of Mars and the albedo A of the true surface, in the presence of a scattering atmosphere of optical thickness $\tau \ll 1$, may differ slightly from each other, since as τ_λ increases toward the violet the brightness B_λ of the atmospheric column also increases. This can be illustrated by the approximate formula

$$p_\lambda = A_\lambda e^{-2\tau_\lambda} + B_\lambda.$$

Therefore, during clear periods fluctuations of the visual albedo of the continents in the violet region may pass unnoticed.

2. The true continent-mare contrast at $\lambda = 400\text{ m}\mu$ is, as a rule, entirely blurred by an atmospheric veil produced by the scattering of light in the Martian atmosphere.

3. In the $400\text{--}650\text{ m}\mu$ range, the Martian atmosphere scatters light in the same sense as Rayleigh scattering, so that toward lower wavelengths the rate of limb darkening of the apparent disk is more gradual.

4. Coarse particles float in the Martian atmosphere, scattering light of various wavelengths in a sense opposite to the Rayleigh scattering. The presence of such particles in the Martian atmosphere has been established in observations with $\lambda \geq 650\text{ m}\mu$, and it results in a decrease in the limb darkening to the infrared. Thus, in the $400\text{--}840\text{ m}\mu$ interval, the influence of the Martian atmosphere on the limb darkening increases on either side of the $650\text{ m}\mu$ wavelength value. Consequently, for studies of the light reflection from the true surface of Mars, observations should in our opinion be made at $\lambda \approx 650\text{ m}\mu$.

REFERENCES

1. BARABASHOV, N. P. — *Astronomicheskii Tsirkulyar Astronomicheskoi observatorii pri Khar'kovskom gosudarstvennom universitete*, No. 8, 1951.
2. KOVAL', I. K. and A. V. MOROZHENKO. — *Astronomicheskii Zhurnal*, Vol. 39: 65-72, 1962.
3. BARABASHOV, N. P. and I. K. KOVAL'. *Fotograficheskaya fotometriya Marsa so svetofil' trami* (Photographic Photometry of Mars Using Filters). — *Izdatel'stvo Khar'kovskogo gosudarstvennogo universiteta*, 1959.
4. BARABASHOV, N. P. and I. K. KOVAL' — *Astronomicheskii Zhurnal*, Vol. 37, No. 2, 1960.
5. SYTINSKAYA, N. N. — *Uchenye zapiski Leningradskogo universiteta*, Vol. 116: 125-137, 1949.
6. BARABASHOV, N. P. — *Astronomicheskii Tsirkulyar Astronomicheskoi observatorii pri Khar'kovskom gosudarstvennom universitete*, No. 9, 1952.
7. BARABASHOV, N. P. — *Astronomicheskii Tsirkulyar Astronomicheskoi observatorii pri Khar'kovskom gosudarstvennom universitete*, No. 11, 1953.
8. KOVAL', I. K. — *Astronomicheskii Zhurnal*, Vol. 34: 412-418, 1957.
9. DIDYCHENKO, E. I., I. K. KOVAL', and A. V. MOROZHENKO. — *Izvestiya Glavnoi Astronomicheskoi Observatorii Akademii Nauk UkrSSR*, Vol. 5, No. 1, 1963.
10. BARABASHOV, N. P., I. K. KOVAL', and A. T. CHEKIRDA. — *Izvestiya komissii po fizike planet*, No. 3: 3-15, 1961.
11. KUIPER, D. P. [Editor]. *The Atmospheres of the Earth and Planets*. [Russian translation, 1952.]
12. KOZYREV, N. A. — *Izvestiya Krymskoi Astrofizicheskoi Observatorii*, Vol. 15: 147, *Izdatel'stvo AN SSSR*, 1955.

*L.A. Bugaenko, O.I. Bugaenko, I.K. Koval', and
A. V. Morozhenko*

THE BRIGHTNESS DISTRIBUTION IN THE MARGINAL ZONE OF MARS

Photographic-photometry studies of the variation of brightness with angle of light incidence along the radius of the disk of Mars cannot give the desired information, since such observations are limited to distances of $r \leq 0.85 R_{\odot}$ from the center of the image.

Thus it was necessary to find an alternative method for investigating the radial brightness distribution of the planet. This method would have to, first, make it possible to obtain data on the brightness variation at the edge of the image and, second, raise considerably the measurement accuracy. It is our opinion that the method of obtaining photoelectric cross sections of the apparent planetary disk meets these requirements. Moreover, if the diurnal motion of the planet is used as the mechanism for displacing the electrophotometer diaphragm, then we automatically eliminate the necessity for measuring the scale of the image. In processing the observational results, it suffices just to know the ephemeris diameter of the planet. At the same time, electrophotometric measurements have a high accuracy.

$\lambda, m\mu$ r/R_{\odot}	355	390	420	450	475	510	560	600	760	900
0.00	1.000	1.000	1.000	1.000	1.000	1.000	1.000	1.000	1.000	1.000
.40	0.965	0.981	0.983	0.977	0.971	0.960	0.951	0.943	0.951	0.958
.60	.892	.950	.951	.927	.906	.889	.874	.866	.870	.880
.80	.690	.842	.850	.801	.753	.710	.673	.652	.668	.679
.85	.589	.791	.794	.719	.682	.638	.550	.558	.581	.602
.90	.450	.702	.711	.637	.570	.519	.476	.447	.460	.470
.92	.369	.650	.659	.585	.526	.472	.420	.394	.403	.417
.94	.301	.569	.575	.511	.465	.406	.355	.336	.341	.349
.96	.208	.470	.475	.431	.388	.310	.275	.204	.261	.285
.97	.097	.331	.335	.299	.274	.250	.161	.107	.132	.148

During the 1963 opposition of Mars we applied the above method to study the brightness distribution along the apparent diameter of the planet. The observations were made at the Cassegrainian focus of the 70-cm reflector at the Main Astronomical Observatory of the UkrSSR Academy of Sciences. The electrophotometer diaphragm accepted a circle $0''.35$ in diameter on the celestial sphere. An EMI-9502 photomultiplier (355–600 $m\mu$) and an infra-red photomultiplier (450–900 $m\mu$) were used as radiation pickups, and the recordings were made on a loop oscillograph. Seconds of time were marked off in a parallel fashion using a contact chronometer, in order to control

the scale of the trace. The observations were made with light filters, whose effective wavelengths in combination with an FEU photocathode are listed in the table.

Since the errors in these observations are mainly due to turbulent vibration of the image, only the results of observations made under the most favorable atmospheric conditions were given a final processing. By coincidence, 4 February 1963, the date of actual opposition, was one of the "favorable" days. During that night we obtained 40 to 50 cross sections for each filter, during a two-hour period in which the zenith distance of Mars did not exceed 35° . The effective amplitude of image vibration σ was estimated visually in parallel with the recording of the cross sections (on 4 February 1963, $\sigma = 0''.4$). The cross sections obtained for each filter were averaged, and then the resulting mean curves were corrected for image vibration and for the finite dimension of the diaphragm. Here a normal law of turbulent vibration was assumed. Such an assumption is justified since, for the mean curve, the effective observation time for each point on the apparent disk is much greater than the effective period of image vibration. The true brightness distribution along the diameter of Mars was obtained from the formula

$$F(t) = \frac{1}{A} \int_{-\infty}^{+\infty} S(t-x) F(x) dx, \quad (1)$$

where $F(t)$ and $F(x)$ are, respectively, the observed and true distributions. Physically, the kernel $S(t-x) = S(t')$ of integral equation (1) may be interpreted as the brightness distribution for a point source under the given experimental conditions (diaphragm radius R and effective vibration amplitude σ). The function $S(t-x)$ may be found from the expression

$$S(t') = A \int_{-\infty}^{+\infty} \sqrt{R^2 - (t' - y)^2} \cdot e^{-\frac{y^2}{2\sigma^2}} dy, \quad (2)$$

where the first factor in the integrand takes into account blurring of the brightness-distribution pattern due to the finite size of the diaphragm, and the second factor takes into account blurring due to the turbulent vibration; A is determined from the normalization conditions.

In practice the problem is solved as follows. $S(t')$ is determined from (2) once R and σ are known, and then equation (1) is solved by successive approximations. The observed brightness distribution is taken as a zero approximation, $F(t) = F_0(t)$, and the following auxiliary function is defined:

$$f_1(t) = \frac{1}{A} \int_{-\infty}^{+\infty} S(t-y) F(y) dy.$$

As the first approximation we take the distribution

$$F_1(t) = F_0(t) + [F(t) - f_1(t)].$$

For the n -approximation we have

$$F_n(t) = F_{n-1}(t) + [F(t) - f_n(t)].$$

Then, this procedure is continued until we obtain $f_n(t) \equiv F(t)$. In order to reconstruct the actual distribution in our case, we did not have to go beyond the second approximation.

It should be noted that during the observations the diaphragm moved parallel to the Martian equator. The measurements carried out on

4 February 1963 refer to equatorial continental regions between longitudes of 310° and 180° . The results obtained for the brightness distribution along the radius of the disk of Mars are given in the table.

First of all we observe that at $600\text{ m}\mu$ the variation of brightness with the angle of incidence i is close to a Lambert-type variation. Toward lower λ the steepness of the corresponding curves decreases, reaching a minimum at $420\text{ m}\mu$ and then slowly increasing again to $390\text{ m}\mu$. At $355\text{ m}\mu$ the steepness rises sharply and at the limb it exceeds the steepness for $600\text{ m}\mu$ somewhat. Consequently, it follows that for $355\text{ m}\mu$ the Martian atmosphere has a considerable true absorption. The curve steepness gradually decreases from 600 to $900\text{ m}\mu$. Seeing that an analogous trend was also obtained for 23 January and 28 February 1963, we may conclude that the Martian atmosphere constantly carries scattering dust particles with radii of about one micron (as we noted previously in /1/). The data on the radial brightness distribution for Mars given in the table can be further applied, using the appropriate theoretical formulas, to determine its atmospheric parameters.

In conclusion, let us note that if for each wavelength starting at $420\text{ m}\mu$ we take the values of the visual albedo ρ at the center of the Martian disk obtained in 1961 /2/, then we find for the limb ($r = 0.97R_\odot$ or $i = 76^\circ$) the following values:

$\lambda, \text{ m}\mu$	420	450	475	510	560	600
ρ	0.020	0.021	0.023	0.028	0.029	0.030

Although the measurements apply to the limb of Mars, still at $600\text{ m}\mu$ for probable optical thickness $\tau \leq 0.1$ the true surface will have a noticeable influence on the measured value of ρ . The first term on the right side of the equation

$$\rho_i = Af(i)e^{-2\tau \sec i} + B_i$$

for $A \approx 0.3$; $f(i) \approx 0.1$; $\tau \leq 0.1$ and $i = 76^\circ$ will be not less than 0.014, and at the same time $B_i \leq 0.016$. At $420\text{ m}\mu$ $B_i \approx \rho_i$, from which it follows that the brightness of the atmospheric column in the $420\text{--}600\text{ m}\mu$ range increases considerably at shorter wavelengths. Consequently, in the visible part of the spectrum scattering prevails over absorption in the Martian atmosphere.

REFERENCES

1. KOVAL', I.K. and A.V. MOROZHENKO.—Astronomicheskii Zhurnal, Vol.39; 65-72, 1962.
2. DIDYCHENKO, E.I., I.K.KOVAL', and A.V. MOROZHENKO.—Izvestiya Glavnoi astronomicheskoi observatorii Akademii Nauk UkrSSR, 5(1): 47-67, 1963.

A. V. Morozhenko

RESULTS OF POLARIMETRIC OBSERVATIONS OF
MARS IN 1962-1963

In polarimetric observations of Mars, we examine light polarized at the surface as well as in traversing the atmosphere of the planet. If we assume that these two components have the same plane of polarization, then the total degree of polarization, P , will equal the weighted mean of the two components,

$$P = \frac{I_a P_a + I_s P_s}{I_a + I_s}, \quad (1)$$

where P_a is the polarization of the light scattered by the atmosphere; and P_s the polarization of that reflected by the surface; I_a is the atmosphere brightness, and I_s the surface brightness.

Let us consider the properties of light polarized owing to diffuse reflection from the surface and owing to scattering in the atmosphere.

Natural light is partially polarized upon reflection at a surface. The degree of polarization of the reflected light depends on the physical properties of the surface,* and also on its relief, or texture. In 1905-1912, N. A. Umov established a definite relation between the degree of polarization and the absorptivity of a surface /1, 2, 3/. In his papers on this "Umov effect," Umov suggested that the dependence can be useful in investigating the spectral properties of planetary surfaces. In 1956, G. V. Rozenberg /4/ placed the "Umov effect" on a physical basis, by working out the behavior of a homogeneous isotropic turbid medium with volume coefficient of absorption α and scattering σ . Solving a system of four integrodifferential equations, he derived the following expression which relates the reflectivity of a turbid half-space to the polarization of the light reflected from it and its absorptive properties:

$$c_i R \equiv \sum_t \frac{a_{tt}}{(1+\beta)^t}, \quad (2)$$

where R is the reflective power, c_i a parameter characterizing the polarization of the reflected light, β the ratio of the absorptivity to the coefficient of scattering, a_{tt} a coefficient depending on the angle of incidence, the angle of reflection, and the form of the scattering matrix, and t the scattering order. We see from (2) that as β increases (absorption rises), high-order scattering rapidly becomes insignificant. Taking into consideration only first- and second-order scattering, Rozenberg obtained for the

* In general on the complex refractive index ($m = n - i\kappa$), where n is the real part of the refractive index and κ the absorption coefficient.

degree of polarization of the reflected light the expression

$$P = \frac{1 + \frac{P_{\infty}}{P_0} \frac{\beta - \beta_0}{(1 + \beta_0)Q}}{1 + \frac{\beta - \beta_0}{(1 + \beta_0)Q}}, \quad (3)$$

where P_{∞} is the limiting polarization for $\beta \rightarrow \infty$, P_0 the polarization for a certain $\beta_0 \ll 1$, Q a parameter depending on the angles of incidence and reflection which governs the relative contribution of high-order scattering for $\beta = \beta_0$. It follows from this expression that as β increases and, consequently, the contribution from multiple scattering (which is less polarized) decreases, P increases, approaching the value P_{∞} , corresponding to once-scattered light in a given direction. The relation (3) is thus a quantitative expression of the Umov effect.

Moreover, there is a definite relation between the degree of polarization of light diffusely reflected from a surface and the phase angle. The polarization is greatest at the Brewster angle, which satisfies the equality

$$\tan \varphi = m. \quad (4)$$

Hence, for bodies with different values of m we shall have different polarization-phase curves, peaking at different phase angles. From such a curve, obtained observationally, we can thus determine the refractive index m of the material.

Lyot and Dollfus studied in detail the properties of light polarized owing to diffuse reflection from various surfaces. We shall only cite those results of theirs which, in our opinion, are relevant to the polarimetric study of Mars. Of greatest importance in this respect are surfaces covered with opaque particles (volcanic rocks, sand, etc.) /5, 6/. Dollfus and Lyot showed that for such surfaces (i) polarization-phase curves have a negative branch for phase angles under $10-25^\circ$ (depending on the material and the type of the surface); (ii) the degree of negative polarization depends on multiple scattering among the surface grains; (iii) no negative polarization is observed for a single isolated particle; (iv) increasing the absorption in the powdered medium raises the negative polarization; (v) the degree of polarization depends on particle size, positive polarization being higher for large particles, and negative polarization higher for small particles (here the smallest particles are still much larger than the wavelength); (vi) a particularly deep negative branch is obtained for a combination of coarse and fine particles.

In addition to the integrated-light research of Lyot and Dollfus, we should mention the interesting polarimetric results obtained for the moon at the Main Astronomical Observatory of the Ukrainian Academy of Sciences by V. V. Avramchuk in eight spectral regions in the $355-600 m\mu$ range (see his paper in this volume). According to these measurements, the inversion points for the various lunar features in all spectral regions correspond to the same phase angle (22°), and the negative polarization slightly increases toward the red (from 1.2 % at $355 m\mu$ to 2.0 % at $600 m\mu$).

Let us now consider the properties of the light scattered in the atmosphere. We shall distinguish between two atmospheres: pure (Rayleigh) atmosphere and real atmosphere (with aerosol particles).

For a pure atmosphere, Prof. I. I. Tikhanovskij in 1927 published a theory of light polarization taking into consideration the underlying surface. This theory considers scattering of light by anisotropic gas molecules of

the earth's atmosphere and diffuse reflection at the earth's surface of direct solar radiation, and of diffuse skylight. Triple scattering and absorption were allowed for. He obtained the following expression for the degree of polarization /7/:

$$P = \frac{(1-a) \sin^2 \varphi + \frac{6\pi^3 (n_0^2 - 1) h H_e}{\lambda^4 L_0 (6 - 7a) \bar{H}_0} (K_1 - K_2) -}{(1+a) \sin^2 \varphi + 2 \cos^2 \varphi + \frac{6\pi^3 (n_0^2 - 1) h H_e}{\lambda^4 L_0 (6 - 7a) \bar{H}_0} (K_1 - K_2) +} - \frac{\frac{\mu}{8h} (\sin \alpha + 0.055) (F_1 - 2F_2) \cos^2 (\varphi + \alpha)}{+ \frac{\mu}{8h} (\sin \alpha + 0.055) [2(F_1 + F_2) + (F_1 - 2F_2) \cos^2 (\varphi + \alpha)]} \dots, \quad (5)$$

where α is the sun's elevation, φ the angular distance of the sun from the celestial point observed, a the coefficient of optical anisotropy of air, n_0 the refractive index of air at sea level at 0°C , λ the wavelength in cm, L_0 the number of air molecules in 1 cm^3 under standard conditions, h the scale height, H_e and \bar{H}_0 the air pressure at the point of observation and at sea level, F_1 and F_2 integrals which can be computed numerically, and K_1 , K_2 are certain functions of the angles α and φ .

Much later, in 1951, Chandrasekhar published his theory of light polarization in a pure atmosphere with multiple scattering /8/. The theoretical formulas of Tikhanovskii and Chandrasekhar were applied by Lange /9/ and Coulson /10/ in calculations of degree of polarization. They showed that, although Tikhanovskii's theory allows for just up to triple scattering, it gives results close to those obtained by Chandrasekhar's exact formulas. These results briefly amount to the following:

For a Rayleigh atmosphere, the degree of polarization increases with wavelength, i. e., with decreasing optical thickness of the atmosphere, and rises as the albedo of the underlying surface diminishes.

However, Tikhanovskii's and Chandrasekhar's formulas may clearly be at variance with the results of polarimetric measurements in a real atmosphere containing aerosol particles. Indeed, the study of polarization of the earth's atmosphere by many authors /11, 12, 13/ showed that (i) in most cases the spectral variation of polarization is opposed to the theoretical prediction; (ii) in individual cases the spectral polarization curve is saddle-shaped, with peaks in the red and the violet regions; (iii) the degree of polarization increases with the transparency of the atmosphere. The divergence between the spectral variation of polarization and the theoretical results is attributed to the presence of large particles of various sizes in the atmosphere. In 1961, T. P. Toropova /14/ showed that the presence of aerosol particles of various sizes in the earth's atmosphere may reverse the spectral variation of polarization as compared with the theoretical results.

Toropova investigated the polarization by fog /15/ and obtained on certain days negative polarization at definite phase angles, while no negative polarization was observed in a clear atmosphere. The degree of polarization for a Rayleigh atmosphere, neglecting the influence of the underlying surface, is calculated from

$$P = \frac{\sin^2 \alpha}{1 + \cos^2 \alpha},$$

where α is the phase angle.

Hence it follows that in a Rayleigh atmosphere polarization is always positive. The possibility of negative polarization in case of scattering by large transparent particles was theoretically proved by K. E. Shifrin /16/. Negative polarization is attributable to double refraction within the particle. Since the contribution of doubly reflected light decreases as the refractive index (the real or the imaginary part) increases, negative polarization should also diminish then. The polarimetric investigation of physical characteristics of the Martian surface and atmosphere is complicated by the fact that its phase angle never exceeds 47° . However, in our opinion, valuable information on the properties of the Martian atmosphere and surface can be obtained by studying the spectral polarization-phase curves in a wide spectral range, and also the spectral variation of polarization.

For Mars, the degree of polarization is determined as the weighted average of the surface and the atmospheric polarization components. The surface component P_s is negative at certain phase angles. As regards the atmospheric component P_a , numerous spectrophotometric observations of Mars show that (i) the optical thickness of the atmosphere increases toward the ultraviolet; (ii) the brightness of the Martian atmosphere increases in the same direction. Hence it follows that scattering occurs by small particles which, as we have said, do not cause negative polarization. Thus, at all phase angles we shall have $P_a \geq 0$. In (1), $I_a P_a$ increases toward the violet (mainly due to increase of I_a), while remaining positive. Assuming that the surface component has the same inversion angle for all λ , in the general case we should expect a displacement of the inversion point with decreasing λ . It follows from the preceding that plotting polarization vs. phase curves for Mars in various spectral regions may help in reaching some conclusions on the physical properties of its atmosphere, and also in tracing the changes occurring in the Martian atmosphere as a whole.

Until recently, comparatively few observers were concerned with a study of polarization properties of the visible surface of Mars. We shall therefore summarize the results obtained by each author in turn.

Earliest was the great work of Lyot /6/, carried out during the oppositions of 1922, 1924, 1926. Observations were made with a visual polarimeter, without filters. Lyot studied the polarization of various areas of the Martian surface. His main results amount to the following:

1. Polarization-phase curves have a negative branch for a phase angle $\alpha = 24-27^\circ$ (differing for different oppositions), with the negative polarization reaching a maximum of 1%.
2. The form of the curve varies from one opposition to another (the degree of polarization at $\alpha = 40^\circ$ was 3.0% in 1922, 2.0% in 1924, and 1.6% in 1926).
3. Comparison of the curves of Mars, with those of volcanic ash, sand, red sandstone, and the lunar surface reveal a resemblance between the surfaces of Mars and Moon.
4. The Martian seas have a higher degree of polarization than the plains.
5. The degree of polarization of the southern polar cap fluctuates from one observation to the next.
6. In 1924-1925 (November-January), Lyot observed a sharp decrease of polarization which fell below the usual level (0.85% against the ordinary 2.55%). At that time the Martian atmosphere was seen to become highly turbid, apparently due to raging sandstorms.

The most comprehensive Martian polarimetry was carried out by Dollfus in 1948, 1950, 1952, and 1954 /17/. His main results confirm those of Lyot, but we also find some new conclusions:

1. The least polarization is observed during the Martian spring in each hemisphere.

2. The polarization-phase curve of Mars fits very well the curve of powdered limonite.

3. Observations with filters at $\alpha = 35^\circ$, 25° , 12° show that at $\alpha = 35^\circ$ the polarization is positive over the entire spectral range (400–800 $m\mu$), at $\alpha = 25^\circ$ the polarization is negative in the 550–800 $m\mu$ range, and at $\alpha = 12^\circ$ it is negative throughout.

4. It follows from the same data that the degree of polarization strongly varies with wavelength.

We should also mention two lesser studies of the spectral polarization of Mars. In 1959, Gehrels and Teska /18/ measured the degree of polarization of Mars and obtained the following result. At $\alpha = 33^\circ$ the degree of polarization in the ultraviolet is 6.7%; in the visible spectrum the polarization is close to Lyot's figure (the effective wavelengths are not given).

In 1960–1961, Sobieski /19/ measured the degree of polarization and showed it to be the same at $\lambda = 535 m\mu$ and at $\lambda = 1670 m\mu$. He too observed an increased polarization toward the ultraviolet.

This brief survey of work done on Martian polarimetry shows that more or less reliable data are now available only on the dependence of the degree of polarization on phase in integrated light: no systematic observations were attempted in limited spectral regions. The few existing observations of this kind are unrelated to each other and merely stress the importance of this approach to the study of the physical properties of the Martian atmosphere and surface.

During the 1962–1963 opposition, the polarization of Mars was studied at the Main Astronomical Observatory of the Academy of Sciences of the Ukrainian SSR in eight spectral regions in the 355–600 $m\mu$ range. Observations were made at the 10 meter Cassegrain focus of the 70-cm reflector of the Observatory, using a recording electropolarimeter of our design. A herapatite polaroid was used as an analyzer: its polarizing properties were as follows: degree of polarization in the 420–600 $m\mu$ range, 100%, at 390 $m\mu$ 99%, and at 355 $m\mu$ 98%. An EMI-9502 photomultiplier with an antimony-cesium photocathode was used as detector. The electropolarimeter output (traced on paper by an EPP-09 recorder) gave the degree of polarization directly, so that no tiresome processing was necessary. A special unit in the electropolarimeter simultaneously measured the orientation of the plane of polarization. To improve the accuracy of reading for small degrees of polarization, different recording scales were used, namely 100, 50, 20, 10, and 5%. The analyzer rotated at a rate of 37 r.p.s. The degrees of polarization recorded for each revolution of the analyzer were smoothed by the apparatus which averaged them over several seconds. Observations with each light filter were made for a few minutes, so that the recorder tapes gave degrees of polarization averaged over several hundred measurements.

For small degrees of polarization, the recorder reading (R) is distorted by the instrument noise (N). Since this noise is uncorrelated with the

effective signal (E), the total signal (i. e., the reading) is found from the relation

$$R^2 = E^2 + N^2.$$

To eliminate the noise, two recordings are made during observations. When recording with a rotating polaroid, we obtain R, while recording without polaroid gives N. The noise level determines the threshold sensitivity of the apparatus, i. e., the minimum measurable polarization. Since

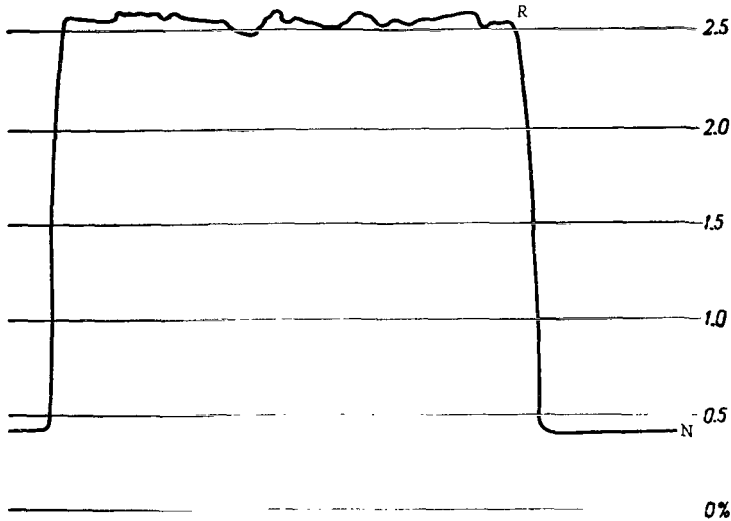


FIGURE 1. Sample recording of polarization magnitude on recorder tape

the noise level increases as the brightness of the object decreases, the threshold sensitivity is lower for faint objects. For Mars in the 390–600 $m\mu$ range the minimum measurable polarization is 0.10–0.20%, while at 355 $m\mu$ the minimum is 0.50%. As regards the intrinsic accuracy of measurements, it is determined by the quality of the recording, and thus by the functional stability of the apparatus. Before the observations, the apparatus is calibrated using a 100% polarized source (light passing through a stationary polaroid). Measurements showed that the apparatus calibrated after two hours of heating up functioned with sufficient stability during the entire night. Figure 1 gives an example of a recording of a 2.51% degree of polarization recorded in 5% scale. Repeated observations of stars whose light is unpolarized (α Lyrae and others) detected no specious polarization in the instrument above threshold level. During the night, several series of measurements were generally made, from which the nightly average was then determined. Deviation of individual measurements from the mean did not exceed 2–3% of the degree of polarization.

Observations were made using a set of circular diaphragms defining circles 1, 2, 4, 10, 20, and 60" in diameter in the sky. We could thus examine the entire planetary disk or selected portions of it. The effective wavelengths of the glass filters in combination with the photomultiplier photocathode were 355, 390, 420, 450, 475, 510, 560, and 600 $m\mu$.

TABLE 1

No.	Date of observation	L	λ, μ α	355	390	420	450	475	510	560	600
1	11.IX 1962	45°	37.40	+9.20%	+4.16%	+2.65%	+2.34%	+2.20%	+1.85%	+1.61%	+1.47%
2	14.	23	37.60	8.20	4.50	2.85	2.45	2.20	1.91	1.53	1.35
3	15.	16	37.70	9.90	4.80	3.37	2.89	2.76	2.40	1.91	1.78
4	25.	257	38.35	9.12	5.19	3.91	3.22	3.22	2.39	2.46	2.72
5	5.X	168	38.85	8.91	5.28	3.95	3.54	3.23	2.99	2.78	2.82
6	6.X	155	38.90	8.73	5.03	3.84	3.43	3.08	2.47	2.21	3.31
7	14.	86	39.14	9.23	5.36	3.27	2.83	2.49	1.96	1.54	1.26
8	16.	84	39.18	9.03	5.09	3.28	2.77	2.37	2.08	1.57	1.40
9	5.XI	240	38.92	8.86	5.32	3.92	3.54	2.98	3.06	2.68	3.37
10	7.XI	227	38.81	9.75	6.24	4.50	3.99	3.68	3.50	3.20	3.56
11	9.	213	38.70	10.00	6.25	4.52	3.90	3.63	3.43	3.20	3.59
12	28.XII	95	27.00	3.40	1.78	1.16	0.74	0.49	0.34	0.12	0.00
13	3.I 1963	11	24.00	2.60	1.72	0.74	0.75	-0.50	-0.40	-0.60	-0.74
14	20.	190	12.90	0.00	-0.50	-0.90			1.13	1.00	0.90
15	21.	233	12.15	0.00	0.70	1.10	0.96	1.30	1.35	1.55	1.38
16	23.	163	10.65	0.00	0.90	1.70	1.50	1.17	1.17	1.20	1.13
17	11.II	349	6.00	0.00	0.49	0.70	0.61	0.69	0.58	0.55	0.55
18	12.	349	6.80	0.00	0.70	0.88	0.85	0.86	0.83	0.73	0.60
19	23.	312	14.90	0.00	0.72	0.90	0.92	0.99	0.91	0.80	0.65
20	24.	200	15.30	0.00	0.70	0.86	0.86	0.85	0.94	0.87	0.80
21	25.	225	16.30		0.45	0.82	0.88	0.90	0.87	0.81	0.70
22	28.	200	18.90	1.00	0.28	0.72	0.80	0.82	0.85	0.87	0.72
23	5.III	65	21.20	1.58	+0.47	0.47	0.59	0.72	0.71	0.73	0.68
24	9.	112	24.00	2.48	1.01	+0.42	+0.24	0.00	0.19	0.33	0.41
25	10.	110	24.50	2.90	1.20	0.61	0.35	+0.16	0.13	0.19	0.27
26	20.	27	29.00	4.55	2.33	1.40	1.11	0.98	+0.83	+0.70	+0.68
27	21.	23	29.50	4.50	2.41	1.50	1.18	1.06	0.95	0.84	0.80
28	24.	307	30.50	5.20	2.72	1.72	1.36	2.20	1.04	0.75	0.70
29	4.IV	212	33.50	7.00	3.90	2.50	1.90	1.60	1.40	1.08	0.98
30	6.	191	34.00	6.90	4.00	2.60	2.00	1.65	1.50	1.15	0.95
31	18.	84	35.95	6.94	4.60	3.31	2.74	2.51	2.26	1.96	1.64
32	10.V	240	37.60		4.90	3.67	2.93	2.56	2.31	1.90	1.73
33	11	200	37.60	8.34	5.02	3.60	2.82	2.51	2.26	1.85	1.58

TABLE 2

No.	Date of observation	α	λ, μ	390	420	450	475	510	560	600
Northern (summer) polar region										
1	11.II 1963	6.0		-0.84%	-0.95%	-1.01%	-0.92%	-0.99%	-1.04%	-0.96%
2	23	14.9		0.73	0.98	1.06	1.20	1.26	1.45	0.95
3	28	18.9		1.16	0.75		1.35	0.90	1.44	0.55
4	5.III	21.2		+0.73	0.46	0.58	0.69	0.68	0.61	0.60
5	20	29.0		1.68	+0.88	+0.60	+0.38	+0.46	+0.51	0.00
6	21	29.5		2.15	1.18	1.04	0.85	0.70	0.54	+0.69
7	24	30.5		2.93	1.83	1.56	1.32	1.26	1.22	0.99
Southern (winter) polar region										
1	11.II 1963	6.0		-0.98	-1.06	-1.12	-1.09	-1.04	-0.99	-1.10
2	23	14.9		1.28	1.36	1.35	1.46	1.56	1.48	1.45
3	28	18.9		1.90	2.72		2.96	3.35	2.86	2.12
4	5.III	21.2		0.00	0.48	0.82	0.97	0.95	1.05	1.01
5	20	29.0		+1.25	+1.60	+1.37	+1.07	+1.07	+0.51	0.00
6	21	29.5		2.85	1.89	1.58	1.48	1.41	1.34	+1.51
7	24	30.5		3.00	2.00	1.54	1.37	1.30	1.16	0.90
Eastern region										
1	11.II 1963	6.0		-1.46	-1.44	-1.50	-1.36	-1.47	-1.42	-1.55
2	23	14.9		0.96	0.52	1.10	1.10	0.96	0.90	0.95
3	28	18.9		0.56	0.43		0.60	0.55	0.38	0.84
4	5.III	21.2		+0.51	0.43	0.39	0.47	0.47	0.33	0.53
5	20	29.0		2.35	+1.33	+0.92	+0.69	+0.67	+0.87	+0.76
6	21	29.5		2.57	1.66	1.37	1.23	0.98	0.92	0.89
7	24	30.5		2.95	2.13	1.72	1.57	1.33	1.12	1.19
Western region										
1	11.II 1963	6.0		-0.72	-1.03	-1.13	-1.06	-1.03	-1.07	-0.92
2	23	14.9		0.57	0.90	0.95	1.00	1.00	1.10	1.18
3	28	18.9		1.75	1.19		2.52	1.46	2.75	3.40
4	5.III	21.2		+0.69	+1.02	+0.62	+0.72	+0.66	+0.53	+0.72
5	20	29.0		1.76	1.20	0.82		0.69	0.46	1.08
6	21	29.5		2.18	1.29	1.04	0.87	0.81	0.78	1.74
7	24	30.5		2.68	1.78	1.44	1.29	1.04	0.98	1.02

Observations were made on clear nights with satisfactory visibility. Before starting the observations, the amplitude of the turbulent image fluctuation was estimated visually. Most of the material was obtained for the entire visible disk and for the central portion, while on nights with particularly stable image, when the fluctuation amplitude did not exceed $1''$ (near opposition), various individual features were observed (the polar caps, Wright clouds). Since the observations were made at zenith distances not greater than 50° , the image on the whole was fairly stable.

From September 1962 to May 1963 observations were made on 33 nights, both before and after the opposition. The results of these observations are given in Tables 1 and 2. In Table 1, L is the central meridian during observation, α the phase angle.

During the first two months of observation, from 11 September to 9 November 1962, the Martian phase angle changed but little ($37.4-39.2-38^\circ.7$). These slight changes of the phase angle could not essentially influence the degree of polarization, had the Martian atmosphere and surface remained unchanged. Therefore, the changes in the degree of polarization obtained during this period can mainly be attributed to real changes occurring on the planet.

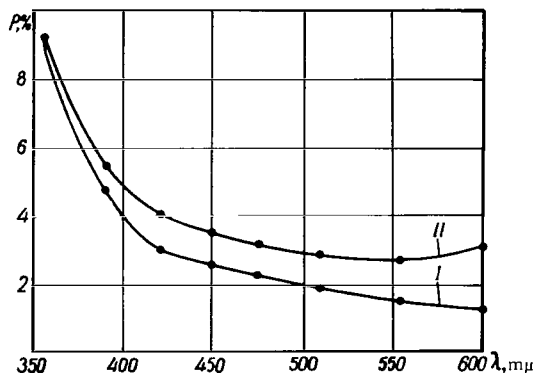


FIGURE 2. Spectral variation of polarization for groups I and II

Let us dwell in detail on the results obtained for this period. Consider the spectral variation of the degree of polarization on various dates. We see from Table 1 (Nos. 1-11) that the degree of polarization at 600μ varied greatly. The observations can be subdivided into two groups so far as polarization is concerned. The first group (11-15 September and 14-16 October) is characterized by low polarization (P_1) at 600μ , equal on the average to 1.42%; the second group (25 September-6 October and 5-9 November) is characterized by high polarization (P_2), equal on the average to 3.25%.

The spectral variation of polarization for the two groups is shown in Figure 2. Note that the scatter of the individual measurements within each group does not exceed 10% in the long-wave region, dropping to 5% at short wavelengths. We see from Figure 2 that for the first group the degree of polarization slowly increases with decreasing wavelength to 3% at 420μ , and then mounts steeply to 9.1% at 355μ . For the second group, the observed polarization at 600μ is 3.25%, dropping to 2.70% at 560μ , then

slowly rising to 4.10% at 420 μ , and again sharply rising to 9.2% at 355 μ . As we see, the polarization behaves differently in the two groups in the 475-600 μ range. Subsequent observations showed that the spectral variation of polarization as found for group I is characteristic of Mars. The results of the second group are apparently associated with some anomalous phenomena on Mars. It is noteworthy that while at long wavelengths the degrees of polarization fluctuate greatly, in the ultraviolet region they remain constant. Let us try to establish the cause of this anomalous, temporary rise in polarization in the red region of the spectrum. We see from Table 1 that the observations of group I correspond to central meridians between 16 and 86°, while those of group II, to central meridians from 155 to 257°. It would therefore seem possible to attribute the differences in polarization to alternation of areas with different polarizing properties. The light and the dark regions on Mars would appear to meet the requirements. According to Dollfus's work mentioned above, the Martian seas have a higher degree of polarization than the highlands. However, he gives for the seas an average polarization excess over the highlands of not more than 50%, while we found a deviation of 150% from the average polarization as obtained from the phase curve at 600 μ . If we moreover remember that in our measurements the diaphragm always delimited areas containing both seas and highlands, we see that the anomalous variation of the degree of polarization cannot be due to surface formations. We should therefore seek an explanation in the Martian atmosphere, mainly in its lower layers, since at 355 μ the degree of polarization remained constant during the two months of observations.

TABLE 3

$\lambda, m\mu$	355	390	420	450	475	510	560	600
α°								
39	+9.50%	+5.30%	+3.95%	+2.90%	+2.80%	+2.50%	+2.10%	+2.00%
37	8.45	4.50	3.40	2.55	2.40	2.15	1.80	1.70
35	7.40	3.90	2.90	2.15	2.05	1.80	1.45	1.35
33	6.45	3.30	2.40	1.80	1.70	1.40	1.12	1.00
31	5.40	2.75	1.85	1.45	1.30	1.10	0.80	0.70
29	4.55	2.20	1.40	1.10	0.90	0.75	0.45	0.35
27	3.70	1.70	1.00	0.70	0.57	0.30	0.12	0.00
25	3.00	1.20	0.60	0.35	0.20	0.00	-0.20	-0.30
23	2.30	0.75	0.22	0.00	-0.15	-0.40	-0.50	-0.55
21	1.50	0.30	-0.22	-0.35	0.50	0.70	0.75	0.75
19	0.80	-0.10	0.50	0.70	0.80	0.90	0.90	0.85
17	0.30	0.43	0.80	0.95	1.00	1.05	1.00	0.95
15	0.00	0.70	0.95	1.10	1.10	1.05	1.05	0.95
13	0.00	0.85	1.00	1.15	1.15	1.10	1.05	0.90
11	0.00	0.90	1.05	1.15	1.15	1.12	1.00	0.85
9	0.00	0.80	0.95	1.05	1.00	1.10	0.90	0.75
7	0.00	0.70	0.82	0.85	0.82	0.85	0.75	0.65
6	0.00	0.60	0.75	0.75	0.70	0.75	0.65	0.55

In view of existing results on the polarization in the earth's atmosphere, our result can be interpreted as follows. The Martian atmosphere, as a rule, is laden with large particles (whose presence is sometimes detectable in red light) with depolarizing properties. Therefore, in most cases, in red light we obtain a low degree of polarization. The anomalously high degree of polarization can be explained by an abrupt decrease in the amount

of depolarizing particles. The constancy of the degree of polarization at $355\text{ m}\mu$ during the two months of observations indicates that the "ultraviolet atmosphere" of Mars has a fairly large optical density, so that all changes occurring in the lower layers of the Martian atmosphere cannot essentially influence its state.

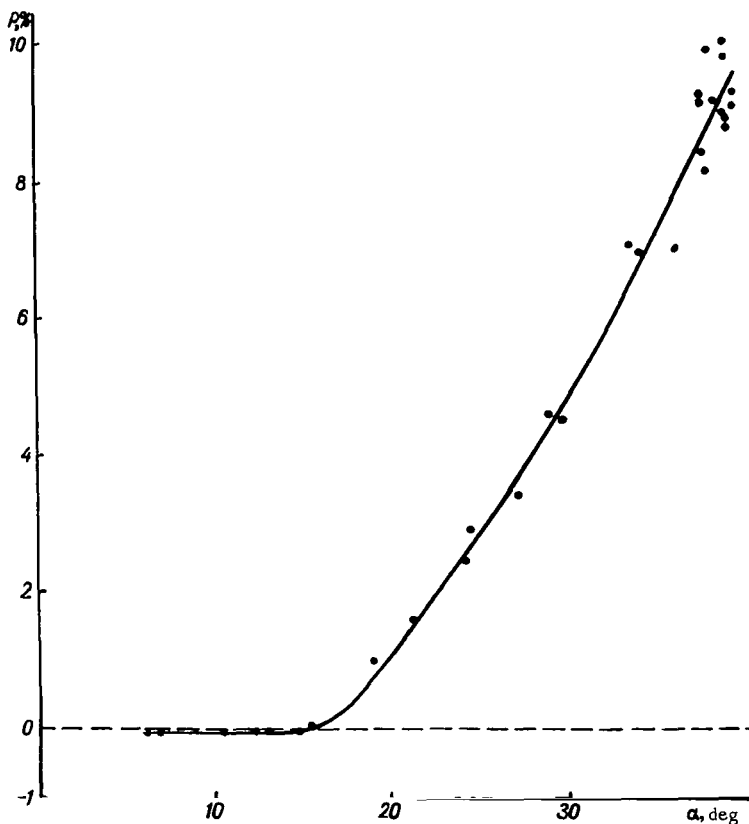


FIGURE 3a. Polarization-phase curve for $\lambda = 355\text{ m}\mu$

Let us now consider the dependence of the degree of polarization on phase angle. The data of Table 1 were used to plot phase curves for all the eight spectral regions. These curves are shown in Figure 3 (a-h). Moreover, since this material may be used in further research, we give in a separate table the data obtained from the averaged phase curves (see Table 3).

The curves for the different wavelengths are given with varying accuracy. At $600\text{ m}\mu$, a considerable scatter of points is observed, reaching up to 30% relative to the mean curve. This scatter diminishes toward the ultraviolet. At $355\text{ m}\mu$ the scatter was as low as 10%. The scatter at long wavelengths is mainly due to surface formations on Mars differing in their polarizing properties, and also to slight variations of the aerosol component of the atmosphere. The low scatter at $355\text{ m}\mu$ indicates that the results of observations at this wavelength are not affected by the changes on the surface and in the lower atmospheric layers of Mars.

It follows from Figure 3 (a-h) that the polarization-phase curves at each wavelength have a characteristic inversion at an angle which decreases with the wavelength.

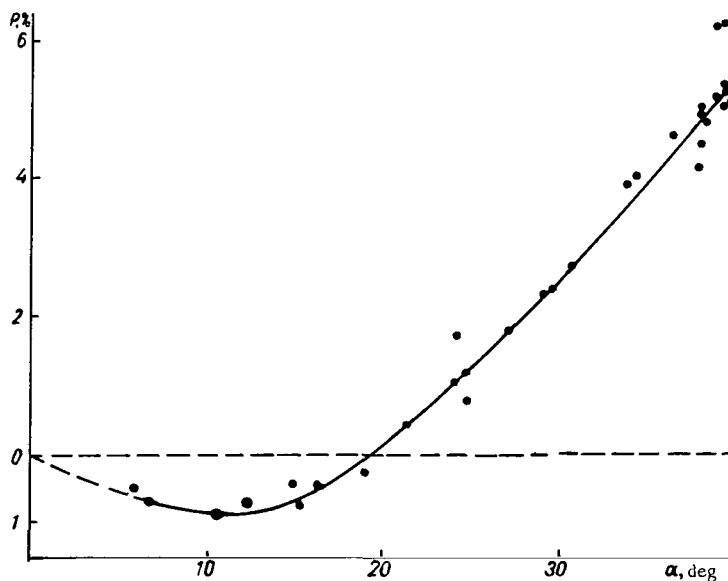


FIGURE 3b. Polarization-phase curve for $\lambda = 390 \text{ m}\mu$

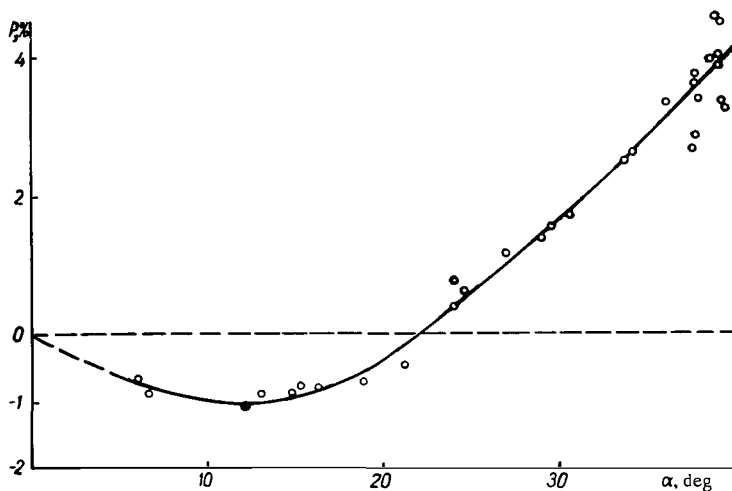


FIGURE 3c. Polarization-phase curve for $\lambda = 420 \text{ m}\mu$

The phase curves have a negative branch with a negative-polarization maximum at $\alpha = 11-13^\circ$. In Figure 3 (a-h) the curve in the $0-6^\circ$ range of phase angles is dashed. No observations were made in this range of phase angles. At $355 \text{ m}\mu$, no negative polarization was observed. Since the

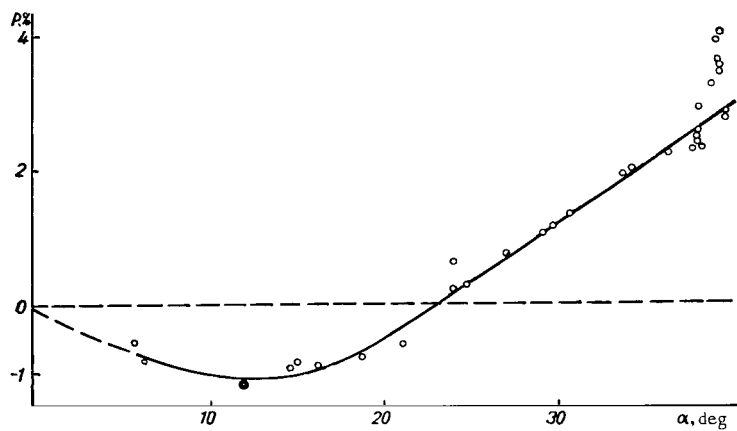


FIGURE 3d. Polarization-phase curve for $\lambda = 450 \text{ m}\mu$

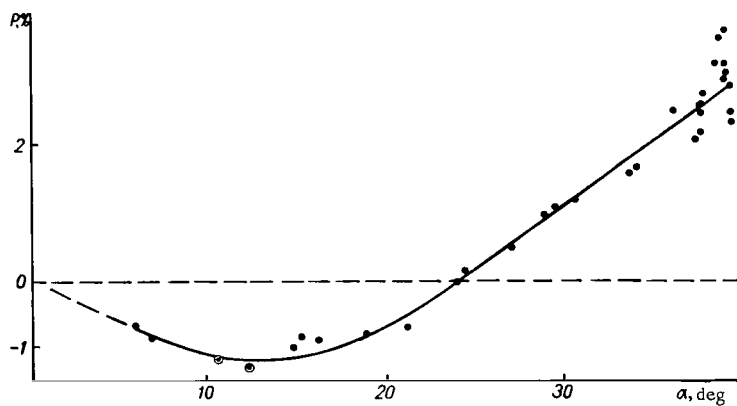


FIGURE 3e. Polarization-phase curve for $\lambda = 475 \text{ m}\mu$

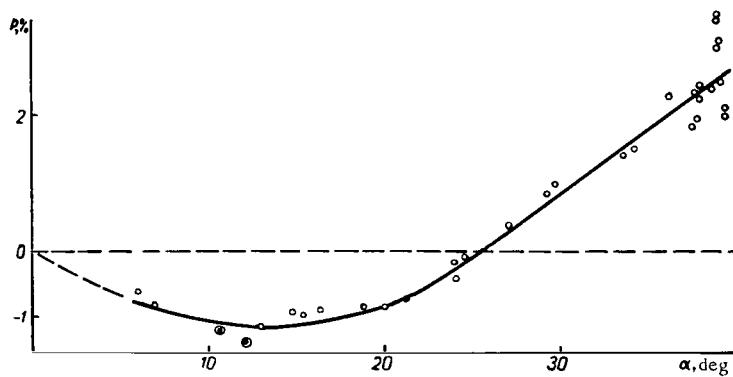


FIGURE 3f. Polarization-phase curve for $\lambda = 510 \text{ m}\mu$

threshold sensitivity of our apparatus at $355\text{ m}\mu$ was 0.5%, it would be better to say that the negative polarization in this spectral region was less than 0.5%. Below we give the inversion angles for each of the filters; for the $\lambda = 355\text{ m}\mu$ filter, we give the angle at which the polarization vanishes.

$\lambda, \text{ m}\mu$	355	390	420	450	475	510	560	600
α_{neg}	$16^{\circ}.0$	19.5	22.2	23.0	24.4	25.2	26.5	27.0

Note that anomalously high negative polarizations were observed at long wavelengths on 21 and 23 January. In Figure 3 (a-h) points corresponding to polarization readings on these days are marked by dotted open circles; a lower weight was assigned to these points in fitting the curves.

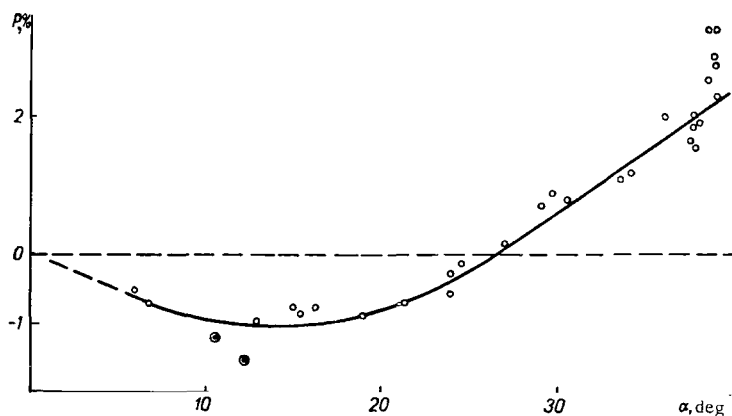


FIGURE 3g. Polarization-phase curve for $\lambda = 560\text{ m}\mu$

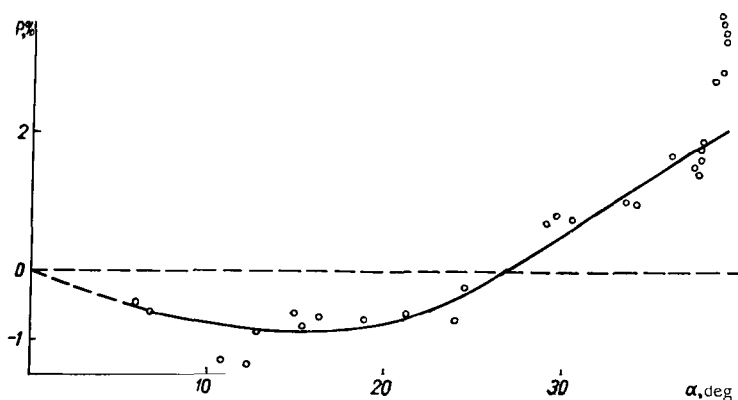


FIGURE 3h. Polarization-phase curve for $\lambda = 600\text{ m}\mu$

The maximum negative polarizations, as read from the phase curves, were the following:

$\lambda, \text{ m}\mu$	355	390	420	450	475	510	560	600
$P_{\text{neg}}, \% \angle$	0.50	0.90	1.05	1.15	1.15	1.12	1.05	0.95

We see that the maximum negative polarizations show a well-defined

spectral variation. The negative polarization slightly increases as the wavelength decreases to $475\text{ m}\mu$. It remains constant in the $475\text{--}450\text{ m}\mu$ range, and then starts decreasing with further decrease of wavelength.

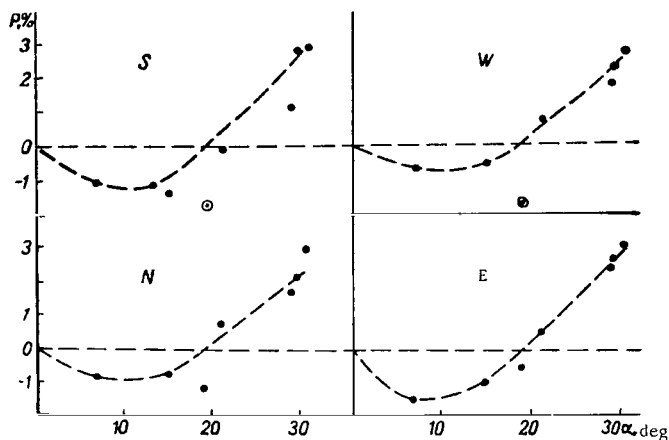


FIGURE 4a. Polarization-phase curves of Martian features at $\lambda = 390\text{ m}\mu$
(N)—northern region, (S)—southern region, (E)—eastern limb, (W)—western limb

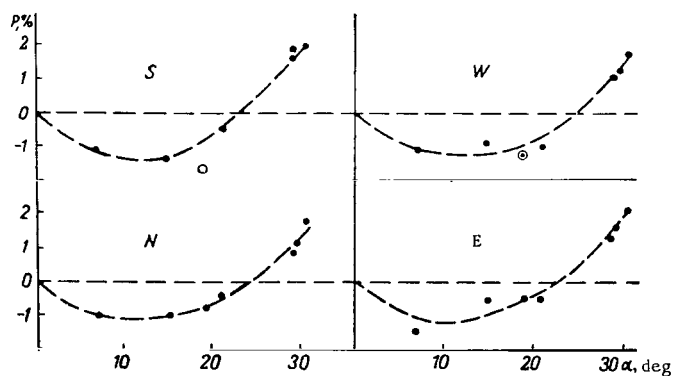


FIGURE 4b. Polarization-phase curves of Martian features at $\lambda = 420\text{ m}\mu$

Let us try to interpret the observed spectral variation of polarization. According to Dollfus's experiments, the degree of negative polarization for various powdered materials increases with the absorptivity of the material. Spectrophotometric investigations of Mars show that its apparent albedo decreases toward the ultraviolet. This is also corroborated by the spectral variation of positive polarization that we have obtained: the polarization increases at shorter wavelengths. If we assume that the spectral variation of positive polarization is governed by the free surface of Mars, the negative polarization should also increase toward the ultraviolet. However,

according to our measurements, this applies only for wavelengths above $475\text{m}\mu$, while for $\lambda \leq 450\text{m}\mu$ the polarization decreases. Hence it follows

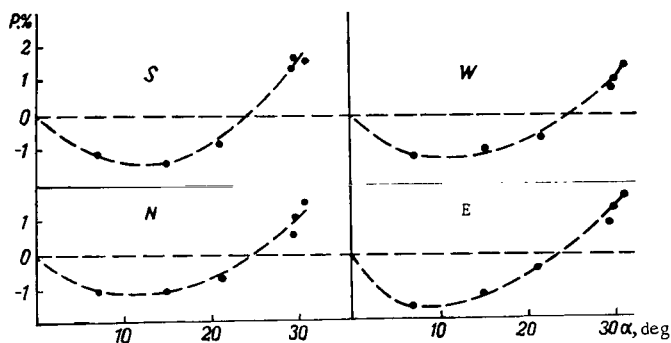


FIGURE 4c. Polarization-phase curves of Martian features at $\lambda = 450\text{m}\mu$

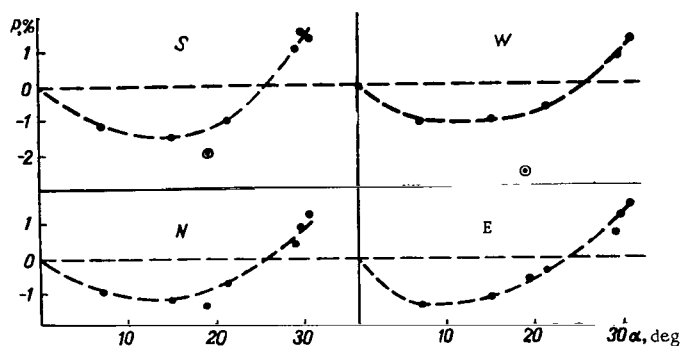


FIGURE 4d. Polarization-phase curves of Martian features at $\lambda = 475\text{m}\mu$

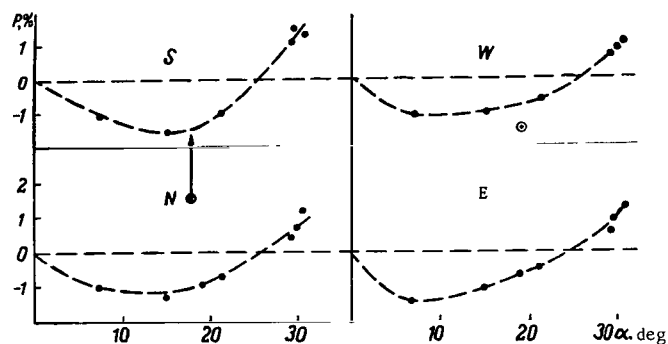


FIGURE 4e. Polarization-phase curves of Martian features at $\lambda = 510\text{m}\mu$

that for $\lambda \leq 450\text{m}\mu$ the atmospheric component is felt, which is positive at all phase angles, and whose influence on the measured degree of polarization grows as the wavelength decreases. The sharp drop of the degree of

negative polarization, and also the considerable shift of the inversion point at $\lambda = 355\text{ m}\mu$ indicate that at these wavelengths the Martian atmosphere has a high optical density.

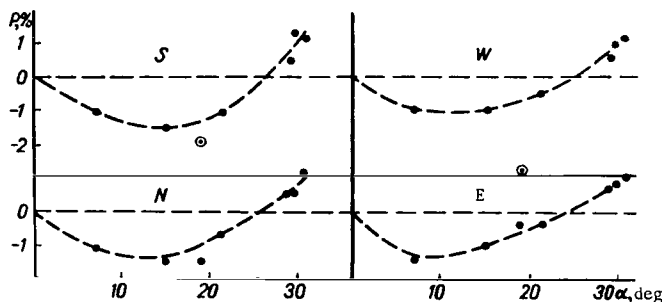


FIGURE 4f. Polarization-phase curves of Martian features at $\lambda = 560\text{ m}\mu$

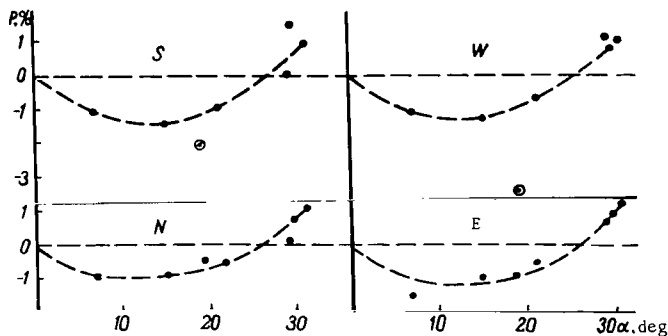


FIGURE 4g. Polarization-phase curves of Martian features at $\lambda = 600\text{ m}\mu$

At times of particularly good visibility we were able to examine the polarization of the Martian polar regions, and also of Wright clouds on the eastern and the western limbs. This applies to the period of February-March 1963 ($\alpha = 7-30^\circ.5$). Figure 4 (a-g) shows the polarization-phase curves for those features (no observations were made at $355\text{ m}\mu$). Owing to the considerable scatter and the paucity of measurements, it was difficult to compare those data with the corresponding figures for the center of Mars and to bring out the peculiar features of the variation of polarization with phase angle and wavelength. We shall therefore confine ourselves to some remarks which follow from an examination of the measured data for these features.

1. The variation of polarization with phase angle for all features is close to that observed for the center of the disk.
2. The spectral variation of positive polarization for these features is less steep than for the center, in keeping with a difference in the spectral variation of their apparent albedo.
3. The polarization of the southern polar region is consistently lower

than that of the northern, which is apparently due to peculiarities of their structure.

4. The degree of polarization of all the features widely fluctuates from day to day. On 28 February 1963 ($\alpha = 18^\circ.9$), an anomalously high negative polarization was observed for the southern and the western regions (see Table 2) at most wavelengths. In Figure 4 (a-g) the corresponding points are marked by dotted open circles.

REFERENCES

1. UMOFF, N.A.—Phys. Zs., 6:674, 1905.
2. UMOFF, N.A.—Phys. Zs., 8:258, 1909.
3. UMOFF, N.A.—Phys. Zs., 13:962, 1912.
4. ROZENBERG, G.V.—Sbornik, posvyashchennyi pamyati akademika P.P. Lazareva, p.132. Izdatel'stvo AN SSSR, 1956.
5. DOLLFUS, A.—Ann. d'Astroph., Vol.19, No.2, 1956.
6. LYOT, B.—Ann. Obs. Meudon, Vol.8, 1929.
7. TIKHANOVSKII, I.I.—Izvestiya Krymskogo Pedagogicheskogo Instituta im. M.V. Frunze, Vol.2, 1928.
8. CHANDRASEKHAR, S.—Nature, 167(4237):51, 1951.
9. LANGE, Z.—Meteorol, 6(11):339, 1952.
10. COULSON, K.L.—Dep. of Met., Sci. Rep. 4, Contract AF 19(122):239.
11. BOIKO, P.N.—Izvestiya Astrofizicheskogo Instituta AN KazSSR, 11:89-96, 1961.
12. BOIKO, P.N.—Izvestiya Astrofizicheskogo Instituta AN KazSSR, 10:83-93, 1960.
13. BOIKO, P.N. Rasseyaniye i polarizatsiya sveta v zemnoi atmosfere (In: Scattering and Polarization of Light in the Atmosphere), p.149.—Izdatel'stvo AN KazSSR, 1962. [English translation by the Israel Program for Scientific Translations, Jerusalem, 1965, TT 65-50005.]
14. TOROPOVA, T.P.—Izvestiya Astrofizicheskogo Instituta AN KazSSR, 11:105-110, 1961.
15. TOROPOVA, T.P. Rasseyaniye i polarizatsiya sveta v zemnoi atmosfere (In: Scattering and Polarization of Light in the Atmosphere), p.144.—Izdatel'stvo AN KazSSR, 1962. [English translation by the Israel Program for Scientific Translations, Jerusalem, 1965, TT 65-50005.]
16. SHIFRIN, K.E. Rasseyaniye sveta v mutnoi srede (Scattering of Light in a Turbid Medium).—GITTL, 1951.
17. DOFFLUS, A.—Ann. d'Astroph., Suppl. No.4, p.1177, 1957.
18. GEHRELS, and TESKA.—Astroph. J., 64:332, 1959.
19. SOBIESKI.—Astroph. J., Vol.66, No.10, 1961.

A. V. Morozhenko and E. G. Yanovitskii

DETERMINATION OF OPTICAL PARAMETERS OF THE ATMOSPHERE AND SURFACE OF MARS

To determine the optical parameters of the atmosphere and the surface of Mars from absolute photometric data, we start with a known brightness distribution of the planetary disk, which is specified by the values of the brightness factor $\bar{\rho}(\eta, \zeta)$, where ζ and η are the cosines of the angle of incidence and of the angle of reflection, respectively. The theory of radiative transfer gives an approximate expression for $\bar{\rho}$ as a function of the optical parameters of the surface and the atmosphere of the planet; these parameters can be determined by the method of least squares. The formulas used generally allow for first-order scattering only, assuming small optical thickness of the Martian atmosphere. This assumption ($\tau_0 \leq 0.1$), however, is not always valid, particularly not for wavelengths $\lambda < 400 \text{ m}\mu$. Moreover, during dust storms, as observed, e. g., during the great opposition of 1956, the optical thickness of the Martian atmosphere substantially increased even in the visible spectrum (see, e. g., /1, 2/). In these cases more accurate formulas must be applied, and the treatment becomes correspondingly more complicated.

It is more convenient to tabulate the brightness distribution and to find the optical parameters by comparing the observed brightness distribution with the theoretical. A. V. Kurchakov /3/, for example, used this method: he also took into consideration the possibility of true absorption in the atmosphere of Mars. However, tabulation of the three unknown parameters τ_0 , λ , and A , where λ is the photon survival probability, and A the surface albedo, also demands tedious computations. Moreover, determining the optical parameters τ_0 and λ by the method of comparison involves considerable relative errors. This is so because the component of $\bar{\rho}$ due to the light reflected directly from the surface of Mars is considerably greater than ρ , i. e., the component of $\bar{\rho}$ due to diffuse reflection of light by the atmosphere alone (in any case, in the long-wavelength region). This point

TABLE 1

$\lambda, \text{ m}\mu$	380	430	560	630	730
τ_0	0.20	0.17	0.10	0.08	0.05
$\bar{\rho}$	0.100	0.119	0.184	0.236	0.280
ρ	0.056	0.047	0.027	0.021	0.013

is illustrated by Table 1, which gives the values of $\bar{\rho}$ for the center of the Martian disk ("highland") obtained by N. N. Sytinskaya /4/ during the 1939

opposition, and also the exact values of the atmospheric component ρ , obtained by applying the tables /5/ for the values of τ_0 given in /4/.

In the present paper we offer a computational procedure and give auxiliary tables which enable one to calculate, relatively simply and with fair certainty, the optical parameters of the atmosphere and the surface of Mars for $0.01 \leq \tau_0 \leq 1.0$ and $0.5 \leq \lambda \leq 1$. The procedure presented is applied to some of the absolute photometric data of Mars published in various sources.

In what follows we shall make use of the following assumptions:

1. The Martian "highlands" are orthotropically reflecting (for $\eta \geq \frac{1}{2}$).

Special investigations seem to support this (see, e.g., /4, 6, 7/).

2. The optical parameters of the atmosphere and the surface of Mars are constant for all the scanned points of the highland from which the brightness distribution curve is plotted. This assumption is never strictly true, so that the resulting optical parameters represent certain averages.

3. The atmosphere of Mars does not absorb selectively in the entire range of wavelengths used in Martian photometry. In /8/ and /9/ (say) we find indications of selective absorption in the atmosphere of Mars, but this result still lacks satisfactory physical explanation.

It was shown by V. V. Sobolev /10/, and independently by van de Hulst /11/, that the brightness factor in the case of orthotropic reflection (assumption 1 above) and a spherical scattering indicatrix is given by

$$\bar{\rho}(\eta, \zeta) = \rho(\eta, \zeta) + \frac{A}{1-AC} \mu(\eta) \mu(\zeta), \quad (1)$$

where $\pi S \mu(\zeta) \zeta$ and C are the illuminance of the planetary surface due to diffuse atmospheric radiation and the spherical albedo of the planet, respectively, in the absence of a reflecting surface ($A=0$); πS is the illuminance of a surface element located at the upper boundary of the atmosphere perpendicular to the incident rays.

For the center of the planetary disk as observed from the Earth we have, instead of (1),

$$\bar{\rho}(1, \zeta_0) = \rho(1, \zeta_0) + \frac{A}{1-AC} \mu(1) \mu(\zeta_0), \quad (2)$$

where ζ_0 is the cosine of the angle of incidence of radiation striking the planetary surface at the center of the disk.

From (1) and (2) we find

$$\frac{\bar{\rho}(\eta, \zeta) - \rho(\eta, \zeta)}{\bar{\rho}(1, \zeta_0) - \rho(1, \zeta_0)} = k(\eta, \zeta), \quad (3)$$

where

$$k(\eta, \zeta) = \frac{\mu(\eta)}{\mu(1)} \cdot \frac{\mu(\zeta)}{\mu(\zeta_0)}. \quad (4)$$

For true opposition of Mars ($\eta = \zeta$), expression (3) takes the form

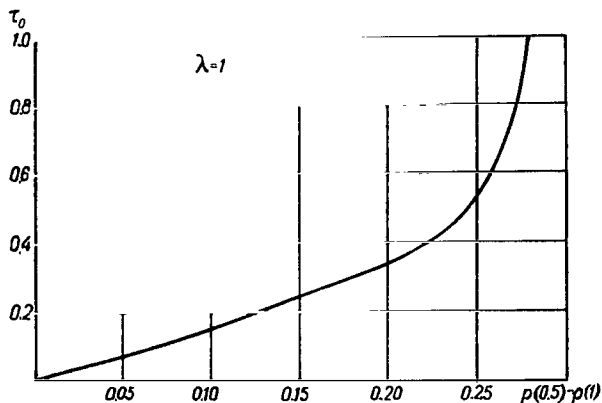
$$\frac{\bar{\rho}(\eta) - \rho(\eta)}{\bar{\rho}(1) - \rho(1)} = k(\eta), \quad (5)$$

where

$$k(\eta) = \frac{\mu^2(\eta)}{\mu^2(1)}. \quad (6)$$

It is assumed here that the scattering indicatrix of the Martian atmosphere

is spherical, which is evidently untrue. Hence, the optical parameters determined from these formulas are in error. For an extremely elongated indicatrix, formulas (1)–(6) have the same form [12].



Let us analyze expression (5) (the results will apply to any phase angle, i. e., to (3)). The right-hand side of (5) is found theoretically. On the left-hand side $\bar{\rho}(\eta)$ and $\bar{\rho}(1)$ are the observed values, while $\rho(\eta)$ and $\rho(1)$ are theoretically calculated. The main point, however, is that (5) does not contain A , i. e., we have entirely eliminated the influence of the surface and, consequently, this formula gives much more accurate values of the optical parameters τ_0 and λ .

The procedure based on equality (5) clearly reduces to the determination of τ_0 and λ for which the difference between the right- and the left-hand sides of (5) is minimum (theoretically, zero) for all $\eta = \xi$.

TABLE 2

$\lambda=1$

τ_0	0.01		0.03		0.05		0.10		0.15		0.20		0.25		0.50		1.00	
	ρ	k	ρ	k	ρ	k	ρ	k	ρ	k	ρ	k	ρ	k	ρ	k	ρ	k
1	0.003	1.000	0.008	1.000	0.013	1.000	0.027	1.000	0.041	1.000	0.056	1.000	0.071	1.000	0.148	1.000	0.297	1.000
0.95	0.003	1.000	0.009	0.999	0.015	0.997	0.030	0.995	0.046	0.993	0.060	0.991	0.077	0.988	0.160	0.979	0.314	0.964
0.90	0.003	0.999	0.010	0.997	0.016	0.994	0.033	0.989	0.051	0.984	0.068	0.980	0.085	0.975	0.172	0.956	0.332	0.928
0.85	0.004	0.999	0.011	0.995	0.018	0.991	0.037	0.984	0.056	0.976	0.075	0.969	0.094	0.961	0.187	0.932	0.352	0.890
0.80	0.004	0.998	0.012	0.993	0.021	0.988	0.042	0.976	0.062	0.966	0.084	0.956	0.104	0.946	0.204	0.906	0.374	0.849
0.75	0.004	0.997	0.014	0.992	0.023	0.984	0.047	0.969	0.070	0.954	0.093	0.942	0.117	0.930	0.224	0.878	0.400	0.808
0.70	0.005	0.996	0.016	0.989	0.026	0.980	0.053	0.960	0.079	0.942	0.105	0.926	0.131	0.911	0.246	0.847	0.427	0.765
0.65	0.006	0.995	0.018	0.986	0.030	0.974	0.061	0.950	0.091	0.929	0.120	0.909	0.148	0.890	0.272	0.814	0.457	0.720
0.60	0.007	0.992	0.021	0.982	0.036	0.968	0.070	0.942	0.104	0.912	0.134	0.890	0.163	0.866	0.303	0.778	0.491	0.673
0.55	0.008	0.990	0.025	0.976	0.042	0.962	0.083	0.927	0.122	0.894	0.159	0.867	0.194	0.840	0.340	0.739	0.530	0.625
0.50	0.010	0.988	0.030	0.972	0.050	0.953	0.098	0.910	0.144	0.873	0.186	0.840	0.225	0.810	0.393	0.696	0.574	0.576
0.40	0.016	0.983	0.046	0.958	0.076	0.931	0.147	0.871	0.210	0.819	0.266	0.775	0.316	0.735	0.499	0.600	0.682	0.477
0.30	0.027	0.976	0.080	0.935	0.131	0.895	0.242	0.810	0.334	0.740	0.412	0.684	0.476	0.635	0.678	0.487	0.836	0.377
0.20	0.061	0.960	0.172	0.893	0.273	0.831	0.470	0.707	0.614	0.616	0.719	0.549	0.796	0.496	0.984	0.361	1.096	0.287
0.10	0.232	0.915	0.600	0.781	0.876	0.677	1.278	0.505	1.470	0.409	1.572	0.352	1.628	0.316	1.722	0.246	1.785	0.209

TABLE 3

 $\lambda=0.95$

τ_0	0.05		0.10		0.15		0.20		0.25		0.50		1.00	
	ρ	k	ρ	k	ρ	k	ρ	k	ρ	k	ρ	k	ρ	k
1	0.012	1.000	0.025	1.000	0.039	1.000	0.049	1.000	0.061	0.000	0.122	1.000	0.223	1.000
0.95	0.014	0.997	0.028	0.995	0.042	0.992	0.054	0.990	0.067	0.989	0.132	0.977	0.237	0.960
0.90	0.015	0.994	0.031	0.989	0.047	0.984	0.059	0.979	0.074	0.975	0.143	0.952	0.253	0.918
0.85	0.017	0.991	0.034	0.983	0.052	0.974	0.066	0.967	0.082	0.961	0.156	0.926	0.271	0.875
0.80	0.019	0.987	0.039	0.975	0.059	0.963	0.073	0.952	0.091	0.944	0.171	0.897	0.290	0.830
0.75	0.022	0.983	0.044	0.967	0.066	0.951	0.082	0.938	0.101	0.926	0.188	0.866	0.312	0.784
0.70	0.025	0.978	0.050	0.958	0.074	0.939	0.092	0.921	0.114	0.906	0.207	0.833	0.336	0.736
0.65	0.029	0.972	0.057	0.948	0.085	0.924	0.105	0.902	0.129	0.883	0.230	0.797	0.363	0.686
0.60	0.034	0.965	0.065	0.936	0.098	0.907	0.119	0.881	0.147	0.858	0.257	0.758	0.393	0.636
0.55	0.040	0.959	0.078	0.922	0.114	0.888	0.139	0.857	0.169	0.830	0.288	0.716	0.427	0.584
0.50	0.047	0.948	0.092	0.906	0.134	0.865	0.163	0.830	0.197	0.798	0.326	0.671	0.465	0.532
0.40	0.072	0.927	0.138	0.863	0.197	0.808	0.233	0.760	0.276	0.718	0.426	0.568	0.561	0.428
0.30	0.123	0.890	0.228	0.800	0.314	0.725	0.361	0.663	0.417	0.613	0.582	0.450	0.697	0.328
0.20	0.258	0.819	0.443	0.692	0.576	0.595	0.632	0.523	0.698	0.463	0.851	0.323	0.930	0.243
0.10	0.826	0.659	1.202	0.481	1.382	0.381	1.385	0.322	1.431	0.284	1.508	0.212	1.546	0.175

TABLE 4

 $\lambda=0.90$

τ_0	0.05		0.10		0.15		0.20		0.25		0.50		1.00	
	ρ	k	ρ	k	ρ	k	ρ	k	ρ	k	ρ	k	ρ	k
1	0.012	1.000	0.024	1.000	0.036	1.000	0.048	1.000	0.061	1.000	0.118	1.000	0.208	1.000
0.95	0.013	0.997	0.026	0.995	0.040	0.991	0.053	0.989	0.067	0.988	0.128	0.975	0.222	0.954
0.90	0.014	0.994	0.029	0.989	0.044	0.982	0.058	0.977	0.073	0.972	0.138	0.948	0.237	0.909
0.85	0.016	0.991	0.032	0.982	0.049	0.972	0.065	0.964	0.081	0.956	0.151	0.919	0.255	0.860
0.80	0.018	0.986	0.037	0.974	0.055	0.959	0.072	0.953	0.090	0.939	0.165	0.888	0.273	0.811
0.75	0.020	0.981	0.041	0.964	0.061	0.947	0.081	0.933	0.100	0.920	0.182	0.855	0.294	0.760
0.70	0.023	0.977	0.047	0.956	0.070	0.933	0.091	0.915	0.112	0.898	0.201	0.819	0.319	0.708
0.65	0.027	0.971	0.054	0.944	0.079	0.916	0.103	0.896	0.127	0.874	0.223	0.780	0.342	0.654
0.60	0.032	0.965	0.062	0.932	0.092	0.898	0.118	0.872	0.145	0.848	0.249	0.740	0.371	0.600
0.55	0.037	0.957	0.073	0.918	0.106	0.877	0.147	0.848	0.166	0.817	0.280	0.695	0.403	0.545
0.50	0.044	0.948	0.087	0.900	0.126	0.852	0.161	0.818	0.194	0.783	0.316	0.646	0.439	0.490
0.40	0.068	0.922	0.130	0.856	0.184	0.790	0.231	0.745	0.275	0.700	0.414	0.538	0.532	0.382
0.30	0.116	0.884	0.214	0.789	0.293	0.700	0.357	0.642	0.411	0.589	0.605	0.415	0.665	0.284
0.20	0.242	0.812	0.416	0.676	0.550	0.561	0.625	0.498	0.689	0.440	0.774	0.288	0.896	0.204
0.10	0.778	0.643	1.120	0.456	1.292	0.337	1.374	0.293	1.475	0.255	1.485	0.182	1.516	0.145

τ_0 can be found by a different method if we know that $\lambda=1$. Then, for $\eta=\xi$, we have from (1)

$$\rho(0.5) - \rho(1) = \bar{\rho}(0.5) - \bar{\rho}(1) + \frac{A}{1-AC} \cdot [\mu^2(1) - \mu^2(0.5)]. \quad (7)$$

The figure shows the curve of the difference $\rho(0.5) - \rho(1)$, as calculated for ($\lambda=1$) from Chandrasekhar's exact tables of the functions X and Y /5/.

In the zero approximation

$$\rho(0.5) - \rho(1) = \rho(0.5) - \rho(1).$$

Whence we find, using the figure, the value of τ_0 in this approximation.* Then applying the tables of /5/ to this τ_0 , we find the third term on the

* Note that the optical thickness τ_0 found in this way is the minimum optical thickness for any λ . Hence, the curve in the figure can be used to obtain a rough estimate of the lower boundary of τ_0 .

TABLE 5

 $\lambda=0.80$

τ_0	0.05		0.10		0.15		0.20		0.25		0.50		1.00	
	ρ	k	ρ	k	ρ	k	ρ	k	ρ	k	ρ	k	ρ	k
1	0.010	1.000	0.021	1.000	0.031	1.000	0.042	1.000	0.052	1.000	0.098	1.000	0.162	1.000
0.95	0.011	0.996	0.023	0.994	0.034	0.991	0.046	0.988	0.057	0.985	0.106	0.958	0.176	0.947
0.90	0.013	0.993	0.026	0.987	0.038	0.982	0.050	0.975	0.062	0.969	0.115	0.928	0.188	0.891
0.85	0.014	0.990	0.028	0.979	0.042	0.970	0.056	0.961	0.069	0.950	0.125	0.896	0.201	0.834
0.80	0.016	0.986	0.032	0.971	0.047	0.957	0.062	0.945	0.076	0.931	0.137	0.861	0.215	0.777
0.75	0.018	0.980	0.036	0.962	0.053	0.944	0.070	0.928	0.085	0.909	0.151	0.824	0.232	0.718
0.70	0.020	0.975	0.041	0.951	0.060	0.931	0.079	0.908	0.096	0.885	0.166	0.783	0.250	0.658
0.65	0.024	0.969	0.047	0.940	0.069	0.911	0.089	0.886	0.108	0.859	0.185	0.741	0.270	0.598
0.60	0.028	0.962	0.054	0.925	0.079	0.891	0.102	0.862	0.124	0.829	0.206	0.695	0.293	0.537
0.55	0.033	0.953	0.064	0.909	0.092	0.869	0.127	0.834	0.142	0.796	0.232	0.646	0.320	0.477
0.50	0.040	0.943	0.078	0.890	0.109	0.843	0.138	0.802	0.166	0.758	0.263	0.593	0.359	0.418
0.40	0.060	0.916	0.113	0.842	0.159	0.776	0.199	0.722	0.233	0.667	0.344	0.475	0.426	0.307
0.30	0.102	0.873	0.186	0.768	0.254	0.681	0.307	0.613	0.352	0.547	0.473	0.351	0.539	0.212
0.20	0.213	0.794	0.362	0.645	0.466	0.535	0.538	0.458	0.590	0.388	0.698	0.225	0.738	0.142
0.10	0.685	0.613	0.989	0.414	1.112	0.307	1.188	0.249	1.220	0.204	1.269	0.131	1.285	0.099

TABLE 6

 $\lambda=0.50$

τ_0	0.05		0.10		0.15		0.20		0.25		0.50		1.00	
	ρ	k	ρ	k	ρ	k	ρ	k	ρ	k	ρ	k	ρ	k
1	0.006	1.000	0.012	1.000	0.018	1.000	0.024	1.000	0.029	1.000	0.051	1.000	0.076	1.000
0.95	0.007	0.996	0.014	0.992	0.020	0.988	0.026	0.984	0.032	0.981	0.055	0.962	0.082	0.926
0.90	0.008	0.991	0.015	0.984	0.022	0.976	0.029	0.967	0.035	0.959	0.060	0.921	0.085	0.849
0.85	0.009	0.986	0.017	0.974	0.025	0.961	0.032	0.948	0.038	0.936	0.065	0.877	0.094	0.773
0.80	0.010	0.980	0.019	0.963	0.027	0.945	0.035	0.930	0.043	0.911	0.071	0.831	0.101	0.696
0.75	0.011	0.973	0.021	0.951	0.031	0.928	0.040	0.905	0.048	0.883	0.078	0.782	0.109	0.619
0.70	0.013	0.965	0.024	0.936	0.035	0.908	0.044	0.880	0.054	0.859	0.087	0.730	0.116	0.544
0.65	0.014	0.957	0.028	0.922	0.040	0.899	0.051	0.852	0.060	0.819	0.096	0.672	0.127	0.470
0.60	0.017	0.947	0.032	0.905	0.046	0.862	0.058	0.820	0.069	0.782	0.108	0.617	0.139	0.398
0.55	0.020	0.936	0.038	0.885	0.054	0.833	0.066	0.785	0.080	0.740	0.121	0.556	0.152	0.330
0.50	0.024	0.922	0.045	0.862	0.061	0.800	0.079	0.744	0.093	0.693	0.137	0.492	0.168	0.267
0.40	0.036	0.886	0.067	0.800	0.092	0.718	0.113	0.646	0.130	0.582	0.181	0.357	0.208	0.158
0.30	0.062	0.828	0.111	0.710	0.147	0.603	0.175	0.514	0.197	0.440	0.248	0.221	0.268	0.082
0.20	0.124	0.725	0.215	0.563	0.271	0.432	0.308	0.336	0.332	0.267	0.377	0.106	0.386	0.041
0.10	0.415	0.494	0.586	0.288	0.656	0.188	0.688	0.127	0.701	0.093	0.715	0.042	0.718	0.025

right-hand side of (7) (it is found using (1) and the tables of /5/). Taking the new value of the difference $\rho(0.5) - \rho(1)$ and again using the graph, we find the next approximation for τ_0 , etc. The convergence is quite rapid, particularly for small τ_0 .

To facilitate the processing of the results of observations using (5), Tables 2-6 give the exact values of $\rho(\eta)$ and $k(\eta)$, calculated from the tables of /5/. In Table 2 for $\tau_0 = 0.01$ and 0.03 , $\rho(\eta)$ and $k(\eta)$ were calculated using Chandrasekhar's method /13/ proposed for low optical thicknesses. Analogous tables can easily be obtained for $\eta \neq \zeta$.

In a subsequent work we intend to publish tables of $\rho(\eta)$ and $k(\eta)$ for scattering indicatrices of various elongation. The calculations will be made using the tables of /14/, obtained from the approximate formulas of /15/.

Experience shows that the determination of the optical parameters τ_0 and λ from (5) with the aid of Tables 2-6 is very fast and fairly reliable. Also note that the determination of τ_0 and λ can be considerably simplified by operating with the graphs of the quantities tabulated in Tables 2-6.

We now proceed with an analysis of some results of absolute photographic photometry of Mars published in various sources.

The first work in this field is due to N. N. Sytinskaya /4/, during the 1939 opposition. Applying our procedure to these results for the Martian highland, we find the optical parameters listed in Table 7.

TABLE 7

$\tilde{\lambda}, m\mu$	630	560	420	380
τ_0	0.04	0.08	0.17	0.70
λ	1.00	1.00	1.00	0.54
A	0.232	0.168	0.084	0.086

TABLE 8

$\tilde{\lambda}, m\mu$	640	580	520	460
τ_0	0.05	0.08	0.12	0.15
λ	1.00	1.00	1.00	1.00
A	0.244	0.198	0.151	0.098

We should first emphasize that the brightness factor curve for $\lambda = 730 m\mu$ was not used due to the high scatter of points. This also applies, though to a lesser degree, to the curve for $\lambda = 630 m\mu$. This scatter is apparently due to inhomogeneities of the Martian surface which, at lower wavelengths, are masked by the atmosphere.

It is noteworthy that in the ultraviolet region the atmosphere is strongly absorbing. It has been repeatedly stated (see, e. g., /16, 17/) that the "ultraviolet layer" of the Martian atmosphere also has considerable true absorption. We obtained numerical estimates of the degree of absorption.

We further applied our procedure to the absolute photometric data obtained by I. K. Koval' /18/ during the 1954 opposition. The results are arranged in Table 8. It was found that in the 460-640 $m\mu$ range the atmosphere of Mars is purely scattering. The optical thickness given in Table 8 is somewhat higher than that in /18/.

TABLE 9

η	$\tilde{\lambda}, m\mu$			
	840	750	530	430
1.00	0.420	0.323	0.162	0.113
0.90	441	336	173	119
80	475	355	192	128
75	496	368	203	132
70	518	383	216	136
65	546	403	231	142
60	578	428	248	148
55	612	457	270	155
50	648	492	292	162

We could not process completely the extensive material on the absolute photometry of Mars obtained during the 1956 opposition /19/. We therefore limited our analysis to two dates: 27/28 September for $\lambda = 840 m\mu$ and $\lambda = 750 m\mu$, and 26/27 September for $\lambda = 530 m\mu$ and $\lambda = 430 m\mu$; the

corresponding brightness curves were sufficiently smooth. The brightness coefficients found from these curves are listed in Table 9.

Also note that dust storms were observed at these dates in the atmosphere of Mars /19/.

The results are listed in Table 10. For $\tilde{\lambda} = 430 \text{ m}\mu$, with $\tau_0 \leq 1$ and $0.5 \leq \lambda \leq 1$, no solution was obtained.

TABLE 10

$\tilde{\lambda}, \text{m}\mu$	840	750	530
τ_0	1.0	0.48	0.32
λ	1	1	0.9
A	0.251	0.264	0.121

In the infrared, the optical thickness of the atmosphere of Mars was fairly large, increasing with the increase of wavelength. This can be attributed to the presence of coarse particles in the atmosphere of Mars /2/, in keeping with the electrophotometric observations carried out at the Main Astronomical Observatory of the Academy of Sciences of the Ukrainian SSR in 1963 /20/.

On the other hand, this sharp variation of optical thickness with wavelength in the infrared (see Table 9) raises some doubts. In all probability, this is due to errors in the observational data. For the 1939 and 1954 oppositions, smoothed tables of brightness distribution over the disk of Mars were available, while for 1956 we used observations made on particular days, which might clearly be distorted by random errors. However, the presence of coarse dust particles at all times in the atmosphere of Mars seems to have been firmly established.

Also note that in the infrared the surface albedo does not vary much with wavelength (see Table 9).

The results of processing of the 1956 data /19/ are inconclusive and require further analysis. We should eventually be able to arrive at more certain conclusions concerning the physical properties of the surface and the atmosphere of Mars.

Moreover, as we have already observed, the elongation of the scattering indicatrix of the Martian atmosphere should be taken into consideration; this will be done in a subsequent work. However, the following preliminary conclusions have been reached.

From $\lambda \approx 450 \text{ m}\mu$ to $\lambda \approx 850 \text{ m}\mu$ the atmosphere of Mars is purely scattering. For $\lambda \leq 450 \text{ m}\mu$, true absorption is felt: in this range it increases with decreasing wavelength, and for $\lambda \approx 350 \text{ m}\mu$, $\lambda \sim 0.5$ for the Martian atmosphere.

During dust storms, the optical thickness of the Martian atmosphere in the infrared increases with increasing wavelength, owing to the presence of coarse dust particles. Apparently, dust is always present in some quantity in the atmosphere /20/.

REFERENCES

1. SYTINSKAYA, N.N.—In: Rezul'taty nablyudenii Marsa vo vremya velikogo protivostoyaniya 1956 g. v SSSR, p.166. Izdatel'stvo AN SSSR, 1959.
2. KOVAL', I.K. and A.V. MOROZHENKO.—AZh, 39: 65. 1962.
3. KURCHAKOV, A.V.—Vestnik Leningradskogo Universiteta, 7: 154. 1960.
4. SYTINSKAYA, N.N.—Trudy yubileinoi nauchnoi sessii Leningradskogo universiteta, astronomiya, p.25. 1948.
5. CHANDRASEKHAR, S., D. ELBERT, and A. FRANKLIN.—Astroph. J. 115: 244. 1952.
6. BARABASHOV, N.P.—Tsirkulyar Khar'kovskoi Observatorii, No. 9, p.3. 1952.
7. BARABASHOV, N.P. and V.I. GARAZHA.—AZh, 37: 501. 1960.
8. KOZYREV, N.A.—Izv. Kr. AO, 15: 147. 1955.
9. ÖPIK, E.J.—J. Geophys. Res., 65: 3057. 1960.
10. SOBOLEV, V.V. —DAN SSSR, 61: 803. 1948.
11. VAN DE HULST, U.—Astroph. J., 107: 220. 1948.
12. SOBOLEV, V.V. Perenos luchistoi energii v atmosferakh zvezd i planet (Radiative Transfer in Stellar and Planetary Atmospheres).—GITTL. 1957.
13. CHANDRASEKHAR, S. Radiative Transfer.—Oxford Univ. Press. 1950.
14. MOROZHENKO, O.V. and E.G. YANOVITS'KII. Tablitsi dlya rozrakhunku intensivnosti viprominyuvannya atmosfer planet.—Vid-vo AN URSR, 1964. [In Ukrainian.]
15. YANOVITSKII, E.G.—This volume.
16. DE VAUCOULEURS, G. Physics of the Planet Mars. [Russian translation. 1956.]
17. KELLOGG, W. and C. SAGAN. The Atmospheres of Mars and Venus.—National Academy of Sciences, National Research Council, Washington, D.C. 1961.
18. KOVAL', I.K.—AZh., Vol. 34, No. 3. 1957.
19. BARABASHOV, N.P. and I.K. KOVAL'. Fotograficheskaya fotometriya Marsa so svetofil'trami v 1956 godu (Photographic Photometry of Mars with Light Filters in 1956).—Izdatel'stvo KhGU, Khar'kov. 1959.
20. BUGAENKO, L.A., O.I. BUGAENKO, I.K. KOVAL', and A.V. MOROZHENKO.—This volume.

E. G. Yanovitskii

**APPROXIMATE SOLUTION OF THE PROBLEM OF DIFFUSE
REFLECTION AND TRANSMISSION OF LIGHT IN
PLANETARY ATMOSPHERES WITH AN ARBITRARY
SCATTERING INDICATRIX**

Introduction

At the hands of V. A. Ambartsumyan, V. V. Sobolev, S. Chandrasekhar, and others, the theory of radiative transfer has become a standard tool for the investigation of physical conditions in stellar and planetary atmospheres. However, the exact methods of the theory of radiative transfer are often unwieldy in application, since in spite of the considerable development of computational techniques, there is still a notable shortage of the requisite tables for comparison of theoretical and experimental data. Approximate methods of transfer theory are therefore still very useful in reducing the solutions to explicit expressions.

Let us consider the approximate methods of solution of the equation of radiative transfer in planetary atmospheres.

Without going into the detailed treatment, we shall discuss those results which have been applied for the interpretation of planetary observations.

One of the earliest calculations of the intensity of radiation diffusely reflected by a half-space ($\tau_0 = \infty$) is that of V. G. Fesenkov /1/. He obtained by successive approximation an expression for the diffusely-reflected radiation, allowing for first- and second-order scattering. A Rayleigh scattering indicatrix was assumed.

Somewhat later, and by essentially the same method, expressions for the intensity of the diffusely reflected and the transmitted radiation for a layer of finite optical thickness were obtained by E. Schönberg /2/. Since his formulas were accompanied by detailed tables, they were often used by planetologists.

However, the method of successive approximations has several shortcomings, the main being the complexity of the final formulas and their low accuracy; the accuracy further decreases with increasing optical thickness /3/.

Transfer theory has attained its greatest success with the development by V. A. Ambartsumyan of exact methods, which were subsequently developed by V. V. Sobolev, S. Chandrasekhar, and others.

A detailed discussion of Ambartsumyan's exact solution of diffuse reflection and transmission of light in planetary atmosphere can be found in Sobolev's paper /3/, and also in his book /4/. Some pages in Chandrasekhar's book /5/ also deal with this question.

In 1943, Sobolev /6/, using Eddington's approximation, derived formulas for the brightness factors of diffusely-reflected and diffusely-transmitted radiation in the case of pure scattering (photon survival probability $\lambda=1$). First-order scattering was allowed for exactly, and higher-order scattering approximately, by retaining for the scattering indicatrix the first two terms of the expansion in Legendre polynomials:

$$\chi(\gamma) = 1 + x_1 \cos \gamma, \quad (1)$$

where γ is the scattering angle, and

$$x_1 = \frac{3}{2} \int_0^\pi \chi(\gamma) \sin \gamma \cos \gamma d\gamma. \quad (2)$$

Scattering of all orders was thus allowed for approximately, and Sobolev's formulas therefore give sufficient accuracy for any optical thickness. Moreover, they are much simpler than, say, Schönberg's formulas /2/, and they are therefore often used by astronomers and geophysicists. The accuracy of these formulas evidently becomes poorer as the indicatrix lengthens. A detailed analysis of the accuracy of Sobolev's formulas is given in /7/.

Somewhat later Sobolev /4, 8/ generalized his solution to the case of true absorption for atmospheres of infinite optical thickness. This made him the first to derive the scattering indicatrix of the Venusian atmosphere.

However, the application of Sobolev's method /6/ to a medium of finite optical thickness in the presence of true absorption leads to highly complicated formulas. Moreover, Sobolev's formulas for higher-order scattering do not contain the term which allows for the dependence of the intensity of diffusely-reflected and diffusely-transmitted radiation on the azimuth. On the other hand, it was shown in /9/ that the intensity of radiation in higher-order scattering varies appreciably with azimuth: e.g., for $\tau_0 = 0.4$ and a fairly elongate indicatrix, it increases by 75% when the azimuth changes through 180° . This variation obviously becomes less pronounced for a rounded indicatrix.

V. A. Ambartsumyan /10, 11/ showed that the intensity of diffusely-reflected and diffusely-transmitted radiation in a plane layer can be simply expressed in terms of certain functions of one variable. These functions satisfy certain nonlinear integral equations. Therefore, having found approximate formulas for these functions, we shall considerably facilitate the calculation of diffusely-reflected and diffusely-transmitted radiation.

These formulas for the case of a spherical scattering indicatrix were derived by A. M. Samson /12/ and, using a somewhat different method, by A. V. Kurchakov /13/.

However, in planetary atmospheres the scattering indicatrix is always elongated in front to a certain extent. The problem therefore arises of finding analytical expressions for Ambartsumyan's functions in the case of a simple nonspherical scattering indicatrix of the form (1). When expressions for brightness factors are found, the terms corresponding to first-order scattering for the indicatrix (1) should be subtracted and analogous terms for an arbitrary scattering indicatrix should be introduced; the result will be analogous to Sobolev's formulas /6,8/, but more general.

In what follows we present in detail the derivation of these relations for $\tau_0 = \infty$ /14/, and then for any τ_0 /15/. The accuracy is estimated in the last section.

Besides previous results of the author /14, 15/, several new relations are given here which may be used in the treatment of planetary observations.

The formulas for brightness factors are derived by a method which differs from that used in /12, 13/; it is based on certain relations due to Chandrasekhar /5/.

1. Medium of infinite optical thickness

Let $\rho(\eta, \zeta, \varphi - \varphi_0)$ be the brightness factor of diffusely-reflected radiation in a plane layer of $\tau_0 = \infty$. Here η and ζ are respectively the cosines of the angles of reflection and incidence of light on the upper surface, $(\varphi - \varphi_0)$ is the azimuth difference between the reflected and incident rays. Then /5/, with a scattering indicatrix of the form (1),*

$$\rho(\eta, \zeta, \varphi - \varphi_0) = \frac{\lambda}{4} \frac{1}{\eta + \zeta} [\Phi_0^0(\eta) \Phi_0^0(\zeta) - x_1 \Phi_1^0(\eta) \Phi_1^0(\zeta) + x_1 \Phi_1^1(\eta) \Phi_1^1(\zeta) \cos(\varphi - \varphi_0)], \quad (3)$$

where

$$\left. \begin{aligned} \Phi_0^0(\eta) &= (1 - c\eta) \varphi(\eta), \\ \Phi_1^0(\eta) &= q\eta \varphi(\eta), \\ \Phi_1^1(\eta) &= \sqrt{1 - \eta^2} \varphi_1(\eta), \end{aligned} \right\} \quad (4)$$

$$c = \lambda x_1 (1 - \lambda) \frac{\alpha_1}{2 - \lambda \alpha_0}, \quad (5)$$

$$q = \frac{2(1 - \lambda)}{2 - \lambda \alpha_0}, \quad (6)$$

$$\alpha_n = \int_0^1 \varphi(\eta) \eta^n d\eta. \quad (7)$$

The functions $\varphi(\eta)$ and $\varphi_1(\eta)$ are defined by the nonlinear integral equation

$$\varphi(\eta) = 1 + \eta \varphi(\eta) \int_0^1 P(\eta') \frac{\varphi(\eta')}{\eta + \eta'} d\eta'; \quad (8)$$

here, with a scattering indicatrix of the form (1), the characteristic function is

$$P(\eta) = a + b\eta^2, \quad (9)$$

where for the function $\varphi(\eta)$

$$a = \frac{1}{2} \lambda, \quad b = \frac{1}{2} \lambda x_1 (1 - \lambda), \quad (10)$$

and for $\varphi_1(\eta)$

$$a = -b = \frac{1}{4} \lambda x_1. \quad (11)$$

In what follows we shall assume that the functions in question

* We use here the notation customary in Soviet work on the radiative transfer /4, 11, 12/.

approximately satisfy relations of the form

$$\begin{aligned}\int_0^1 f(\eta) \eta d\eta &\approx \frac{1}{2} \int_0^1 f(\eta) d\eta, \\ \int_0^1 f(\eta) \eta^2 d\eta &\approx \frac{1}{4} \int_0^1 f(\eta) d\eta.\end{aligned}\tag{12}$$

Let us use (12) to obtain approximate expressions for $\varphi(\eta)$ and $\varphi_1(\eta)$ and compare them with the exact expressions to obtain an idea of the usefulness of these approximations.

We shall apply Chandrasekhar's theorems /5/, which give for a characteristic function of the form (9) the equalities

$$\int_0^1 \frac{\varphi(\eta')}{\eta + \eta'} d\eta' = \frac{\varphi(\eta) - 1}{\varphi(\eta) P(\eta) \eta} - \frac{b(\alpha_1 - \eta \alpha_0)}{P(\eta)},\tag{13}$$

$$\alpha_0 = 1 + \frac{1}{2}(a\alpha_0^2 - b\alpha_1^2).\tag{14}$$

Applying (9) and (12), we can write equation (8) in the approximate form

$$\varphi(\eta) = 1 + \frac{1}{4} \varphi(\eta) \eta (4a + b) \int_0^1 \frac{\varphi(\eta')}{\eta + \eta'} d\eta'.\tag{15}$$

Then from (13) and (15) we have

$$\varphi(\eta) = \frac{2(4\eta^2 - 1)}{2(4\eta^2 - 1) + (4 - k_{0,1}^2)(\alpha_1 - \eta \alpha_0) \eta},\tag{16}$$

where

$$k_{0,1}^2 = 2(2 - 4a - b),\tag{17}$$

here the subscripts 0 and 1 correspond to a and b as defined by (10) and (11), respectively.

From (7) and (12), approximately,

$$\alpha_0 = 2\alpha_1,\tag{18}$$

and then from (14)

$$\alpha_0 = \frac{4}{2 + k_{0,1}}.\tag{19}$$

Inserting (19) in (16), we may write

$$\varphi(\eta) = \frac{1 + 2\eta}{1 + k_0 \eta}.\tag{20}$$

The function $\varphi_1(\eta)$ can clearly be obtained from (20) by substituting k_1 for k_0 . From (10), (11), and (17) we have

$$k_0^2 = (1 - \lambda)(4 - \lambda x_1),\tag{21}$$

$$k_1^2 = 4 - \frac{3}{2} \lambda x_1.\tag{22}$$

Note that the function (20) conveniently serves as the first approximation in the solution of equation (8) by successive approximations. Inserting (20) in (8), we obtain in the second approximation

$$\varphi(\eta) = \left[1 - \frac{\eta}{1 - k_{0,1} \eta} F(\eta) \right]^{-1},\tag{23}$$

where

$$F(\eta) = (1-2\eta)P(\eta) \ln \left(1 + \frac{1}{\eta}\right) + \\ + \frac{(2-k_{0,1})(ak_{0,1}^2+b)}{k_{0,1}^3} \ln(1+k_{0,1}) - \frac{2b}{k_{0,1}^2} [k_{0,1}^2(1-\eta)\eta + (1-k_{0,1})]. \quad (24)$$

Inserting (20) in (4) and applying (5), (6), (18), and (19), we finally obtain

$$\left. \begin{aligned} \Phi_0^0(\eta) &= \frac{[(1-\lambda)(2-\lambda x_1 \eta) + k_0](1+2\eta)}{[2(1-\lambda) + k_0](1+k_0 \eta)}, \\ \Phi_1^0(\eta) &= \frac{(1-\lambda)(2+k_0)(1+2\eta)\eta}{[2(1-\lambda) + k_0](1+k_0 \eta)}, \\ \Phi_1^1(\eta) &= \frac{(1+2\eta)(1-\eta^2)^{1/2}}{1+k_1 \eta}. \end{aligned} \right\} \quad (25)$$

From (3) and (25), we find the approximate brightness factor of diffusely reflected radiation in a plane turbid medium of infinite optical thickness with scattering indicatrix of the form (1). Here $|x_1| \leq 1$.

To pass from the indicatrix (1) to an arbitrary indicatrix $\chi(\gamma)$ we subtract, following Sobolev /6/, the quantity $\frac{\lambda}{4} \frac{(1+x_1 \cos \gamma)}{\eta+\zeta}$ from the right-hand side of (3) and add $\frac{\lambda}{4} \frac{\chi(\gamma)}{\eta+\zeta}$; then, since

$$\cos \gamma = -\gamma \zeta + \sqrt{(1-\gamma^2)(1-\zeta^2)} \cos(\varphi - \varphi_0), \quad (26)$$

we have

$$\rho(\eta, \zeta, \varphi - \varphi_0) = \frac{\lambda}{4} \frac{1}{\eta+\zeta} \left\{ \Phi_0^0(\eta) \Phi_0^0(\zeta) - 1 + x_1 [\gamma \zeta - \Phi_1^0(\eta) \Phi_1^0(\zeta)] + \right. \\ \left. + x_1 [\Phi_1^1(\eta) \Phi_1^1(\zeta) - \sqrt{(1-\eta^2)(1-\zeta^2)}] \cos(\varphi - \varphi_0) \right\} + \frac{\lambda}{4} \frac{\chi(\gamma)}{\eta+\zeta}, \quad (27)$$

where $|x_1| < 3$ and is obtained from condition (2).

Expression (27) is analogous to Sobolev's formula /4, 8/, but it is more convenient for calculations.

Let us now consider some particular cases of formulas (25). For a purely scattering medium ($\lambda=1$), we have from (25)

$$\left. \begin{aligned} \Phi_0^0(\eta) &= 1+2\eta, \\ \Phi_1^0(\eta) &= 0, \\ \Phi_1^1(\eta) &= \frac{(1+2\eta)(1-\eta^2)^{1/2}}{1+k_1 \eta}, \end{aligned} \right\} \quad (28)$$

where

$$k_1^2 = 4 - \frac{3}{2} x_1. \quad (29)$$

If the atmosphere is slightly absorbing (as the atmosphere of Venus /8/), then expanding (25) in powers of $\sqrt{1-\lambda}$ and retaining first order terms relative to $\sqrt{1-\lambda}$, we find

$$\begin{aligned} \Phi_0^0(\eta) &= (1+2\eta) \left(1 - 4\eta \sqrt{\frac{1-\lambda}{4-x_1}}\right), \\ \Phi_1^0(\eta) &= \frac{2\sqrt{1-\lambda}(1+2\eta)\eta}{\sqrt{4-x_1}}. \end{aligned} \quad (30)$$

The function $\Phi_1^1(\eta)$ is determined here as in (28).

The spherical albedo A_s of a planet with $\tau_0 = \infty$ and a scattering indicatrix of the form (1) is given by /4/

$$A_s = 1 - 2 \int_0^1 \varphi_1^0(\eta) d\eta. \quad (31)$$

Inserting $\varphi_1^0(\eta)$ from (25) and applying (18), (19), and (20), we obtain

$$A_s = \frac{\sqrt{4-\lambda x_1} - 2\sqrt{1-\lambda}}{\sqrt{4-\lambda x_1} + 2\sqrt{1-\lambda}}, \quad (32)$$

whence the obvious result: for $\lambda=1$ (pure scattering), $A_s=1$.

Let us consider another particular case of (23). If $\lambda=1$ and $x_1=0$, then

$$\varphi(\eta) = \frac{2}{2(1-\eta) - (1-2\eta)\eta \ln\left(1 + \frac{1}{\eta}\right)}, \quad (33)$$

and this simple expression is accurate to within 1%. V. A. Ambartsumyan /16/ showed that the function $\varphi(\eta)$ specifies, up to a constant factor, the distribution of luminance over the solar disk.

2. Atmosphere of finite optical thickness

As before, we start from Chandrasekhar's results /5/. In this case the brightness factor of diffusely reflected radiation $\rho(\eta, \zeta, \varphi - \varphi_0)$ and of diffusely transmitted radiation $\sigma(\eta, \zeta, \varphi - \varphi_0)$ for a scattering indicatrix of the form (1) are given by the expressions

$$\begin{aligned} \rho(\eta, \zeta, \varphi - \varphi_0) = & \frac{\lambda}{4} \{ \varphi_0^0(\eta) \varphi_0^0(\zeta) - \psi_0^0(\eta) \psi_0^0(\zeta) - \\ & - x_1 [\varphi_1^0(\eta) \varphi_1^0(\zeta) - \psi_1^0(\eta) \psi_1^0(\zeta)] + x_1 [\varphi_1^1(\eta) \varphi_1^1(\zeta) - \\ & - \psi_1^1(\eta) \psi_1^1(\zeta)] \cos(\varphi - \varphi_0) \}, \end{aligned} \quad (34)$$

$$\begin{aligned} \sigma(\eta, \zeta, \varphi - \varphi_0) = & \frac{\lambda}{4} \frac{1}{\zeta - \eta} \{ \varphi_0^0(\eta) \psi_0^0(\zeta) - \varphi_0^0(\zeta) \psi_0^0(\eta) + \\ & + x_1 [\varphi_1^0(\eta) \psi_1^0(\zeta) - \varphi_1^0(\zeta) \psi_1^0(\eta)] + x_1 [\varphi_1^1(\eta) \psi_1^1(\zeta) - \\ & - \varphi_1^1(\zeta) \psi_1^1(\eta)] \cos(\varphi - \varphi_0) \}, \end{aligned} \quad (35)$$

where

$$\left. \begin{aligned} \varphi_0^0(\eta) &= (1 - c_1\eta) \varphi(\eta) - c_2\eta\psi(\eta), \\ \varphi_1^0(\eta) &= [q\varphi(\eta) + p\psi(\eta)] \eta, \\ \varphi_1^1(\eta) &= (1 - \eta^2)^{1/2} \varphi_1(\eta), \end{aligned} \right\} \quad (36)$$

$$\left. \begin{aligned} \psi_0^0(\eta) &= (1 + c_1\eta) \psi(\eta) + c_2\eta\varphi(\eta), \\ \psi_1^0(\eta) &= [p\varphi(\eta) + q\psi(\eta)] \eta, \\ \psi_1^1(\eta) &= (1 - \eta^2)^{1/2} \psi_1(\eta). \end{aligned} \right\} \quad (37)$$

$$\left. \begin{aligned} c_1 &= \lambda x_1 \frac{(2 - \lambda \alpha_0) \alpha_1 - \lambda \beta_0 \beta_1}{4 - \lambda^2 x_1 (\alpha_1^2 - \beta_1^2)}, \\ c_2 &= \lambda x_1 \frac{-(2 - \lambda \alpha_0) \beta_1 + \lambda \beta_0 \alpha_1}{4 - \lambda^2 x_1 (\alpha_1^2 - \beta_1^2)}, \end{aligned} \right\} \quad (38)$$

$$\left. \begin{aligned} q &= \frac{2(2-\lambda\alpha_0)}{4-\lambda^2x_1(\alpha_1^2-\beta_1^2)}, \\ p &= \frac{2\lambda\beta_0}{4-\lambda^2x_1(\alpha_1^2-\beta_1^2)}, \end{aligned} \right\} \quad (38)$$

$$\beta_a = \int_0^1 \psi(\eta) \eta^a d\eta. \quad (39)$$

The functions $\varphi(\eta)$, $\varphi_1(\eta)$ and $\psi(\eta)$, $\psi_1(\eta)$ are determined from the system of nonlinear integral equations

$$\begin{aligned} \varphi(\eta) &= 1 + \eta \int_0^1 \frac{P(\eta')}{\eta + \eta'} [\varphi(\eta) \varphi(\eta') - \psi(\eta) \psi(\eta')] d\eta', \\ \psi(\eta) &= e^{-\frac{\tau_0}{\eta}} + \eta \int_0^1 \frac{P(\eta')}{\eta - \eta'} [\psi(\eta) \varphi(\eta') - \psi(\eta') \varphi(\eta)] d\eta', \end{aligned} \quad (40)$$

where $P(\eta)$ is defined by (9); the functions $\varphi_1(\eta)$ and $\psi_1(\eta)$ are determined from equations (40), if a and b are defined by (11).

We also borrow the following relations from Chandrasekhar /5/:

$$\begin{aligned} P(\eta) \eta \int_0^1 [\varphi(\eta) \varphi(\eta') - \psi(\eta) \psi(\eta')] \frac{d\eta'}{\eta + \eta'} = \\ = \varphi(\eta) - 1 - b\eta [(\alpha_1 - \eta\alpha_0) \varphi(\eta) - (\beta_1 - \eta\beta_0) \psi(\eta)], \end{aligned} \quad (41)$$

$$\begin{aligned} P(\eta) \eta \int_0^1 [\psi(\eta) \varphi(\eta') - \varphi(\eta) \psi(\eta')] \frac{d\eta'}{\eta - \eta'} = \\ = \psi(\eta) - e^{-\frac{\tau_0}{\eta}} - b\eta [(\beta_1 + \eta\beta_0) \varphi(\eta) - (\alpha_1 + \eta\alpha_0) \psi(\eta)], \end{aligned} \quad (42)$$

$$\alpha_0 = 1 + \frac{1}{2} [a(\alpha_0^2 - \beta_0^2) + b(\alpha_1^2 - \beta_1^2)]. \quad (43)$$

Clearly, expressions (3), (4), (5), (6), (8), (13), and (14) are particular cases of (34), (36)–(41), respectively.

As in the case of a semi-infinite medium, we use the approximation (12). Then, applying (9), we write equations (40) in the form

$$\begin{aligned} \varphi(\eta) &= 1 + \frac{4a+b}{4} \eta \int_0^1 \frac{\varphi(\eta) \varphi(\eta') - \psi(\eta) \psi(\eta')}{\eta + \eta'} d\eta', \\ \psi(\eta) &= e^{-\frac{\tau_0}{\eta}} + \frac{4a+b}{4} \eta \int_0^1 \frac{\varphi(\eta') \psi(\eta) - \varphi(\eta) \psi(\eta')}{\eta - \eta'} d\eta'. \end{aligned} \quad (44)$$

But the second terms on the right-hand sides of (44) are determined by (41) and (42). Hence, from (42), (43), and (44) we obtain a system of two linear algebraic equations which can be solved for $\varphi(\eta)$ and $\psi(\eta)$:

$$\begin{aligned} \varphi(\eta) &= \frac{(4\eta^2 - 1) \{ (4\eta^2 - 1) - (4a+b) \eta [\alpha_1 - \beta_1 e^{-\frac{\tau_0}{\eta}} + \eta(\alpha_0 + \beta_0 e^{-\frac{\tau_0}{\eta}})] \}}{[(4\eta^2 - 1) - (4a+b) \alpha_0 \eta^2]^2 - (4a+b)^2 \alpha_1^2 \eta^2 + (4a+b)^2 (\beta_1^2 - \eta^2 \beta_0^2) \eta^2}, \\ \psi(\eta) &= \frac{(4\eta^2 - 1) \{ (4\eta^2 - 1) e^{-\frac{\tau_0}{\eta}} + (4a+b) \eta [\alpha_1 e^{-\frac{\tau_0}{\eta}} - \beta_1 - \eta(\alpha_0 e^{-\frac{\tau_0}{\eta}} + \beta_0)] \}}{[(4\eta^2 - 1) - (4a+b) \alpha_0 \eta^2]^2 - (4a+b)^2 \alpha_1^2 \eta^2 + (4a+b)^2 (\beta_1^2 - \eta^2 \beta_0^2) \eta^2}. \end{aligned} \quad (45)$$

The only unknowns in (45) are α_0 , β_0 , α_1 , and β_1 . To find these unknowns, two additional formulas are required, besides (18) and (43). One is

obtained directly from (39), in view of (12):

$$\beta_0 = 2\beta_1. \quad (46)$$

To derive the second formula, we see that $\varphi(\eta)$ and $\psi(\eta)$, considered as functions of τ_0 (this follows directly from (40)), satisfy the following differential equation /5/:

$$\eta \frac{\partial \psi(\eta, \tau_0)}{\partial \tau_0} \psi(\zeta, \tau_0) + \psi(\eta, \tau_0) \psi(\zeta, \tau_0) = \eta \frac{\partial \varphi(\zeta, \tau_0)}{\partial \tau_0} \varphi(\eta, \tau_0). \quad (47)$$

Multiplying (47) by $d\eta d\zeta$ and integrating with respect to η and ζ from 0 to 1, and also applying the approximate relations (18), (46), and equation (43), we obtain

$$\frac{d\alpha_0(\tau_0)}{d\tau_0} - \frac{1}{2} (4a+b) \alpha_0^2(\tau_0) = 4[1 - \alpha_0(\tau_0)]. \quad (48)$$

Solving this differential equation for the condition

$$\alpha_0(\tau_0)|_{\tau_0=0} = 1, \quad (49)$$

and applying (18), (46), and (43), we find

$$\alpha_0 = \frac{4[(2+k_{0,1}) - (2-k_{0,1})e^{-2k_{0,1}\tau_0}]}{(2+k_{0,1})^2 - (2-k_{0,1})^2 e^{-2k_{0,1}\tau_0}}, \quad (50)$$

$$\beta_0 = \frac{8k_{0,1}e^{-k_{0,1}\tau_0}}{(2+k_{0,1})^2 - (2-k_{0,1})^2 e^{-2k_{0,1}\tau_0}},$$

where $k_{0,1}$ is defined by (17) or (21), (22); the subscripts 0 and 1, as before, correspond to a and b defined by (10) and (11), respectively. It follows from (50) that α_0 and β_0 are related by the simple expression

$$k_{0,1} \alpha_0 = \beta_0 (2 \operatorname{sh} k_{0,1} \tau_0 + k_{0,1} \operatorname{ch} k_{0,1} \tau_0).$$

Applying (17), (18), and (46), we find after simple manipulations that (45) can be written

$$\varphi(\eta) = \frac{4(4\eta^2 - 1) - (4 - k_0^2)[\alpha_0(1+2\eta) - \beta_1(1-2\eta)e^{-\frac{\tau_0}{\eta}}]}{4(k_0^2\eta^2 - 1)} \eta, \quad (51)$$

$$\psi(\eta) = \frac{4(4\eta^2 - 1)e^{-\frac{\tau_0}{\eta}} - (4 - k_0^2)[\beta_0(1+2\eta) - \alpha_0(1-2\eta)e^{-\frac{\tau_0}{\eta}}]}{4(k_0^2\eta^2 - 1)} \eta.$$

The functions $\varphi_1(\eta)$ and $\psi_1(\eta)$ are clearly also found from (51) if k_1 is substituted for k_0 . For $x_1=0$, equations (51) coincide with the corresponding formulas of /12/.

Note that the dependence of the functions $\varphi(\eta)$ and $\psi(\eta)$ (as given by (50) and (51)) on the optical parameters of the medium λ and x_1 reduces to a dependence on the single parameter $k_{0,1}$. Also note that, as for a semi-infinite medium, expressions (51) can be applied as the first approximation in solving the system of integral equations (40) by successive approximations. However, in contrast to the semi-infinite case, already the second approximation involves integral-exponential functions.

Formulas (50), (51), and also (34)–(38) thus give approximate analytical expressions for the brightness factors of diffusely reflected and diffusely transmitted radiation in a plane-parallel atmosphere of optical thickness τ_0 illuminated by parallel rays and having a nonspherical scattering indicatrix (1).

To pass to an arbitrary scattering indicatrix, we respectively subtract from the right-hand sides of (34) and (35) the following quantities:

$$\frac{\lambda}{4} \{1 - x_1 [\eta \zeta - V(1 - \eta^2)(1 - \zeta^2) \cos(\varphi - \varphi_0)]\} \frac{1 - e^{-\tau_0(\frac{1}{\eta} + \frac{1}{\zeta})}}{\eta + \zeta}, \quad (52)$$

$$\frac{\lambda}{4} \{1 + x_1 [\eta \zeta + V(1 - \eta^2)(1 - \zeta^2) \cos(\varphi - \varphi_0)]\} \frac{e^{-\frac{\tau_0}{\eta}} - e^{-\frac{\tau_0}{\zeta}}}{\eta - \zeta} \quad (53)$$

and respectively add

$$\frac{\lambda}{4} \chi(\gamma) \frac{1 - e^{-\tau_0(\frac{1}{\eta} + \frac{1}{\zeta})}}{\eta + \zeta}, \quad (54)$$

$$\frac{\lambda}{4} \chi(\gamma) \frac{e^{-\frac{\tau_0}{\eta}} - e^{-\frac{\tau_0}{\zeta}}}{\eta - \zeta}, \quad (55)$$

where in (54)

$$\cos \gamma = -\eta \zeta + V(1 - \eta^2)(1 - \zeta^2) \cos(\varphi - \varphi_0), \quad (56)$$

and in (55)

$$\cos \gamma = \eta \zeta + V(1 - \eta^2)(1 - \zeta^2) \cos(\varphi - \varphi_0), \quad (57)$$

where $\chi(\gamma)$ represents an arbitrary scattering indicatrix.

Finally we obtain

$$\begin{aligned} \rho(\eta, \zeta, \varphi - \varphi_0) = & \frac{\lambda}{4} \frac{1}{\eta + \zeta} \{ \varphi_0^0(\eta) \varphi_0^0(\zeta) - \psi_0^0(\eta) \psi_0^0(\zeta) - \\ & - 1 + e^{-\tau_0(\frac{1}{\eta} + \frac{1}{\zeta})} - x_1 [\varphi_1^0(\eta) \varphi_1^0(\zeta) - \psi_1^0(\eta) \psi_1^0(\zeta) - \\ & - \eta \zeta (1 - e^{-\tau_0(\frac{1}{\eta} + \frac{1}{\zeta})})] + x_1 [\varphi_1^1(\eta) \varphi_1^1(\zeta) - \psi_1^1(\eta) \psi_1^1(\zeta) - \\ & - V(1 - \eta^2)(1 - \zeta^2)(1 - e^{-\tau_0(\frac{1}{\eta} + \frac{1}{\zeta})})] \cos(\varphi - \varphi_0) \} + \\ & + \frac{\lambda}{4} \chi(\gamma) \frac{1 - e^{-\tau_0(\frac{1}{\eta} + \frac{1}{\zeta})}}{\eta + \zeta}, \end{aligned} \quad (58)$$

$$\begin{aligned} \sigma(\eta, \zeta, \varphi - \varphi_0) = & \frac{\lambda}{4} \frac{1}{\eta - \zeta} \{ \varphi_0^0(\zeta) \psi_0^0(\eta) - \varphi_0^0(\eta) \psi_0^0(\zeta) - \\ & - e^{-\frac{\tau_0}{\eta}} + e^{-\frac{\tau_0}{\zeta}} + x_1 [\varphi_1^0(\zeta) \psi_1^0(\eta) - \varphi_1^0(\eta) \psi_1^0(\zeta) - \eta \zeta (e^{-\frac{\tau_0}{\eta}} - e^{-\frac{\tau_0}{\zeta}})] + \\ & + x_1 [\varphi_1^1(\zeta) \psi_1^1(\eta) - \varphi_1^1(\eta) \psi_1^1(\zeta) - V(1 - \eta^2)(1 - \zeta^2)(e^{-\frac{\tau_0}{\eta}} - e^{-\frac{\tau_0}{\zeta}})] \times \\ & \times \cos(\varphi - \varphi_0) \} + \frac{\lambda}{4} \chi(\gamma) \frac{e^{-\frac{\tau_0}{\eta}} - e^{-\frac{\tau_0}{\zeta}}}{\eta - \zeta}. \end{aligned} \quad (59)$$

In (58) and (59) $|\kappa_i| < 3$, and is related with $\chi(\gamma)$ through (2).

Expressions (58) and (59) resemble the formulas derived by V. V. Sobolev /6/, but have the following advantages.

1. Expressions (58) and (59) are valid if the atmosphere is truly absorbing ($\lambda \neq 1$).

2. For higher-order scattering, the dependence of the brightness factor on azimuth is (approximately) taken into consideration.

3. Since the brightness factors are expressed only in terms of Ambartsumyan's functions φ and ψ , which depend on a single variable (λ , x_1 , and τ_0 are parameters), their calculation is simplified.

We shall now assume that the atmosphere is bounded by an isotropically reflecting surface of albedo A . In this case, as was shown by Sobolev /17/ and independently by van de Hulst /18/, the brightness factors of diffusely reflected radiation $\bar{\rho}(\eta, \zeta, \varphi - \varphi_0)$ and of diffusely transmitted radiation $\bar{\sigma}(\eta, \zeta, \varphi - \varphi_0)$ are given by

$$\bar{\rho}(\eta, \zeta, \varphi - \varphi_0) = \rho(\eta, \zeta, \varphi - \varphi_0) + \frac{A}{1 - AC} \mu(\eta) \mu(\zeta), \quad (60)$$

$$\bar{\sigma}(\eta, \zeta, \varphi - \varphi_0) = \sigma(\eta, \zeta, \varphi - \varphi_0) + \frac{A}{1 - AC} \mu(\zeta) \nu(\eta), \quad (61)$$

where, according to /5/,

$$\mu(\eta) = p\varphi(\eta) + q\psi(\eta), \quad (62)$$

$$\nu(\eta) = 1 - q\varphi(\eta) - p\psi(\eta), \quad (63)$$

$$C = 1 - 2(q\alpha_1 + p\beta_1). \quad (64)$$

Here p and q are defined by (38).

Let us establish the physical meaning of the functions $\mu(\eta)$ and $\nu(\eta)$. Denoting by πS the illuminance of a surface element perpendicular to the solar rays on the upper boundary of the atmosphere, the quantity $\pi S \mu(\zeta) \zeta$ will give the illuminance of the planetary surface when the upper boundary of the atmosphere is illuminated by parallel rays, while $\pi S \nu(\zeta) \zeta$ will give the illuminance of the upper atmospheric boundary from below when it is illuminated from above (nonreflecting surface, i.e., $A=0$). The quantity C is then the spherical albedo of the planet.

Applying $\mu(\zeta)$ and expression (61), we can easily obtain the quantity E , which is highly important in geophysics; this quantity gives the illuminance of the Earth's surface (due to both direct sunlight and to diffuse atmospheric light).

Multiplying the second term in (61) by $2\pi\eta d\eta$ and integrating with respect to η from 0 to 1, and also applying (63) and (64), we find that the illuminance of the Earth's surface by the diffuse atmospheric light due to the presence of a reflecting surface is equal to

$$\frac{\pi S A C}{1 - AC} \mu(\zeta) \zeta,$$

while the illuminance due to diffuse atmospheric light and direct sunlight (with $A=0$) is equal, as we have seen, to $\pi S \mu(\zeta) \zeta$.

Hence,

$$E = \frac{\pi S \mu(\zeta) \zeta}{1 - AC}. \quad (65)$$

An analogous formula for the case of pure scattering was previously obtained by V. V. Sobolev /6/, but expression (65) is more general, since it allows for true absorption.

The fractional contribution of direct sunlight to the total illuminance of

the Earth's surface is

$$\frac{\pi S e^{-\frac{\tau_0}{\zeta}}}{E} = \frac{1-AC}{\mu(\zeta)} e^{-\frac{\tau_0}{\zeta}}. \quad (66)$$

In /19/, among other tables, there are also tables of $\mu(\eta)$ and C for various values of τ_0 , λ , η , and x_1 , which considerably simplifies calculations using (65). Also note that formulas (65) and (66) are exact for a scattering indicatrix of the form (1).

Let us now consider some particular cases.

1. Semi-infinite medium ($\tau_0=\infty$). The formulas clearly reduce to those obtained in the previous section.

2. Pure scattering ($\lambda=1$). Passing in (50) and (51) to the limit for $\lambda \rightarrow 1$, we obtain

$$\alpha_0 = \frac{1+2\tau_0}{1+\tau_0}, \quad \beta_0 = \frac{1}{1+\tau_0}, \quad (67)$$

$$\begin{aligned} \varphi(\eta) &= [\alpha_0(1+2\eta) - \beta_0(1-2\eta) e^{-\frac{\tau_0}{\eta}}] \eta - 4\eta^2 + 1, \\ \psi(\eta) &= [\beta_0(1+2\eta) - \alpha_0(1-2\eta) e^{-\frac{\tau_0}{\eta}}] \eta - (4\eta^2 - 1) e^{-\frac{\tau_0}{\eta}}. \end{aligned} \quad (68)$$

The functions $\varphi_1(\eta)$ and $\psi_1(\eta)$ are determined from (50) and (51) when k_0 is replaced by

$$k_1 = \left(4 - \frac{3}{2} x_1\right)^{1/2}. \quad (69)$$

Since in this case $\alpha_0 + \beta_0 = 2$, it follows from (38) that $c_1 = c_2$ and $p = q$, and, consequently, from (36) and (37) we find that $\Phi_1^0(\eta) = \Psi_1^0(\eta)$. Expressions (34) and (35) for the brightness factors (also (58) and (59)) thus do not contain the functions $\Phi_1^0(\eta)$ and $\Psi_1^0(\eta)$.

3. Evaluating the accuracy of the formulas

The author has previously shown /14/ that for a medium of infinite optical thickness with a scattering indicatrix (1), the approximations (25) for the functions $\Phi_0^0(\eta)$, $\Phi_1^0(\eta)$, and $\Phi_1^1(\eta)$ are accurate to within 5%.

The approximate relations (27) for an arbitrary scattering indicatrix are somewhat less accurate. This is so because only the first two terms in the Legendre expansion of the scattering indicatrix are used for higher-order scattering. Hence, the more elongated the indicatrix, the greater the error in (27). This also applies to media of finite optical thickness. We again remind the reader that an estimate of the accuracy for an arbitrary scattering indicatrix is given in /7/.

To estimate the accuracy of the present formulas for a plane layer of finite optical thickness, we applied the tabulated exact values X and Y of the functions (20) calculated for a spherical scattering indicatrix and various values of the parameters τ_0 , λ , and η . Comparison was made with the results of /19/ for the approximate formulas (68). Figures 1 and 2 show the graphs of

$$\Delta\varphi = \left| \frac{\varphi_T - \varphi}{\varphi_T} \right| \cdot 100\%, \quad \Delta\psi = \left| \frac{\psi_T - \psi}{\psi_T} \right| \cdot 100\% \quad (70)$$

for $0.2 \leq \eta \leq 1$, where φ_T and ψ_T are the exact values of the functions φ and ψ . Note that for $\eta=0$, we have $\Delta\varphi=\Delta\psi=0$.

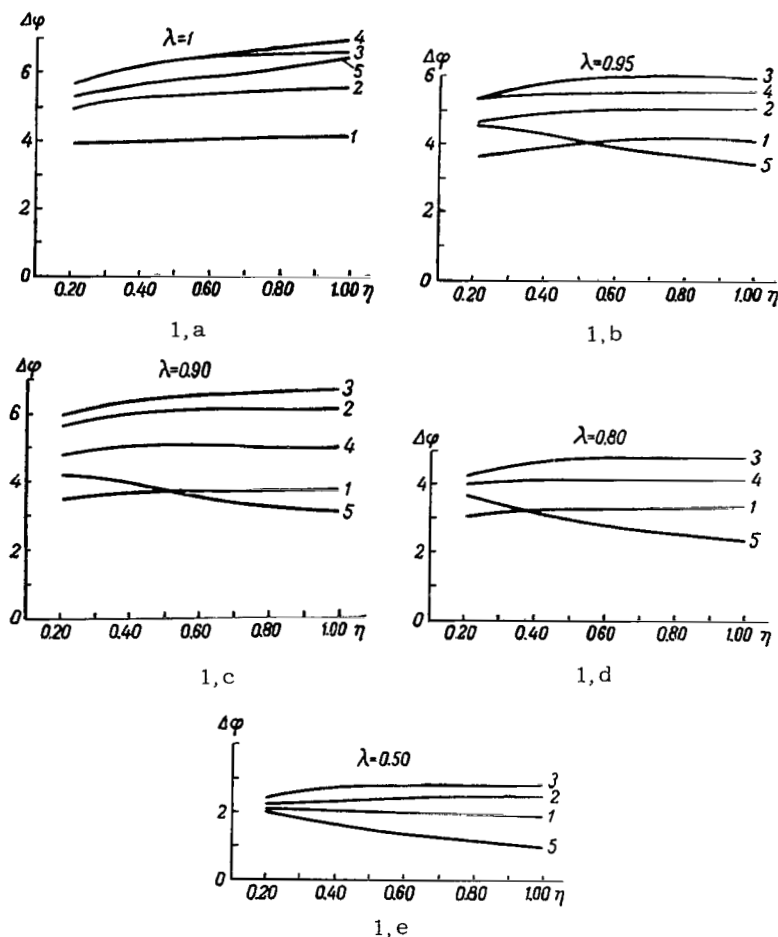


FIGURE 1. Graphs of $\Delta\varphi$:

1—for $\tau_0 = 0.05$; 2—for $\tau_0 = 0.1$; 3—for $\tau_0 = 0.2$; 4—for $\tau_0 = 0.5$; 5—for $\tau_0 = 1.0$

Figures 1-2 show that:

1. For any τ_0 , $\Delta\varphi < 10\%$.
2. For $\tau_0 \leq 0.50$, $\Delta\psi < 10\%$. For these τ_0 , $\Delta\varphi$ and $\Delta\psi$ do not vary much with η .
3. As λ decreases for $\tau_0 \leq 0.50$, the errors $\Delta\varphi$ and $\Delta\psi$ decrease.
4. As the true absorption increases (λ decreases) and the optical thickness becomes greater, $\Delta\psi$ sharply increases with decreasing η , reaching 20% for $\tau_0 \sim 1$. However, for $\tau_0 \sim 1$, we have $\varphi(\eta) \gg \psi(\eta)$, and therefore, the error will be mainly due to $\Delta\varphi$.

Comparable errors in brightness factors may be expected for $x_1 \neq 0$, i. e., a scattering indicatrix of the form (1).

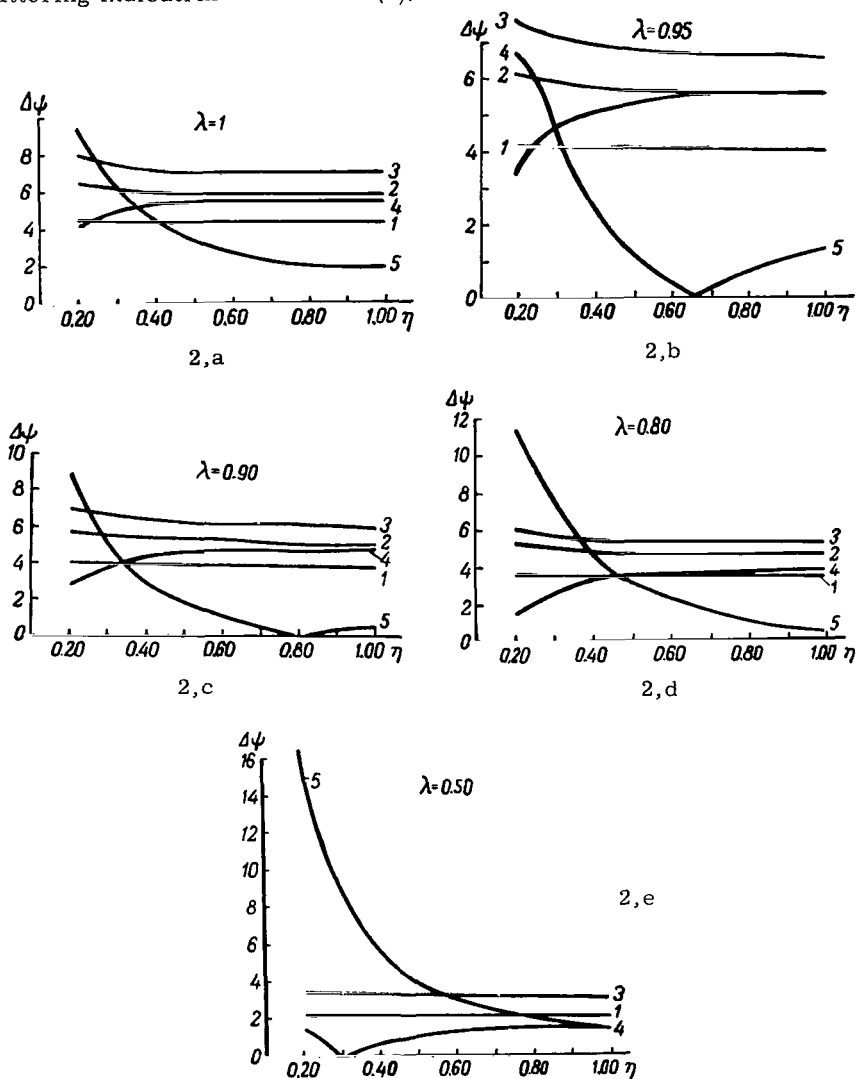


FIGURE 2. Graphs of $\Delta\psi$:

1—for $\tau_0 = 0.05$; 2—for $\tau_0 = 0.1$; 3—for $\tau_0 = 0.2$; 4—for $\tau_0 = 0.5$; 5—for $\tau_0 = 1.0$

The error in the calculation of the functions φ and ψ from the approximate formulas derived here thus does not exceed 10% for the simplest non-spherical indicatrix (1). An exception is the value of the function ψ for high true absorption, when $\tau_0 \geq 1$. In all probability [7], this estimate in the great majority of cases also applies to brightness factors of the diffusely reflected and diffusely transmitted radiation.

In conclusion we note that numerical calculation of brightness factors, both in the presence and in the absence of an isotropically reflecting surface, is greatly simplified by the tables /19/ where the values of φ_0^0 ; φ_1^0 ; φ_1^1 ; φ_0^0 ; φ_1^0 ; φ_1^1 ; μ , ν , and C calculated from the approximate formulas are given for $\tau_0=0.03$; 0.05; 0.10; 0.15; 0.20; 0.30; 0.40; 0.50; 0.75; 1.0; 2.0; 3.0; $\lambda=1$; 0.95; 0.90; 0.80; 0.70; 0.60; 0.50; 0.40; 0.30; 0.20 and $\eta=1.0$; 0.90; 0.80; 0.70; 0.65; 0.60; 0.55; 0.50; 0.45; 0.40; 0.35; 0.30; 0.25; 0.20.

REFERENCES

1. FESENKOV, V.G.—Izvestiya Russkogo Astronomicheskogo Obshchestva, Vol.22, No.3, 1916.
2. SCHÖNBERG, E.—Handbuch der Astrophysik, II(1):208, Berlin, 1929.
3. SOBOLEV, V.V.—UAN, No.6, p. 250, 1954.
4. SOBOLEV, V.V. Perenos luchistoi energii v atmosferakh zvezd i planet (Transfer of Radiative Energy in Stellar and Planetary Atmospheres).—GITTL, 1956.
5. CHANDRASEKHAR, S. Radiative Transfer.—Oxford Univ. Press, 1950.
6. SOBOLEV, V.V.—AZh, Vol.20, No.5-6, 1943.
7. ATROSHENKO, V.S., K.E. GLAZOVA, M.E. MALKEVICH, and E.M. FEIGEL'SON. Raschet yarkosti sveta v atmosfere pri anizotropnom rasseyanii (Calculation of Brightness of Light in the Atmosphere due to Anisotropic Scattering), Part 2.—Trudy Instituta Fiziki Atmosfery, No.3, 1962.
8. SOBOLEV, V.V.—AZh, Vol.21, No.5, 1944.
9. FEIGEL'SON, E.M.—Izv. AN SSSR, Geofizika, No.10, 1958.
10. AMBARTSUMYAN, V.A.—DAN SSSR, 38:257, 1943.
11. AMBARTSUMYAN, V.A.—ZhETF, 13(9-10):224, 1943.
12. SAMSON, A.M.—Inzhinerno-Fizicheskii Zhurnal, 1:65, 1958.
13. KURCHAKOV, A.V.—Vestnik LGU, No.7, p.154, 1960.
14. YANOVITSKII, E.G.—Izvestiya Vysshikh Uchebnykh Zavedenii, Fizika, No.1, p.98, 1962.
15. YANOVITSKII, E.G.—UFZh, 7(3):297, 1962.
16. AMBARTSUMYAN, V.A.—AZh, No.5, p.30, 1942.
17. SOBOLEV, V.V.—DAN SSSR, 61:803, 1948.
18. VAN DE HULST, U.—Astroph. J., 107:220, 1948.
19. MOROZHENKO, O.V. and E.G. YANOVITS'II J. Tablitsi dlya rozrakhunku intensivnosti viprominyuvannya atmosfer planet.—Vid—vo AN URSR, 1964. [In Ukrainian.]
20. CHANDRASEKHAR, S., D. ELBERT, and A. FRANKLIN.—Astroph. J., 115:244, 1952.

O.I. Bugaenko

**DIRECT-READING RECORDING ELECTROPOLARIMETER OF
THE MAIN ASTRONOMICAL OBSERVATORY OF
THE ACADEMY OF SCIENCES OF THE UKRAINIAN SSR**

In this paper we describe the recording electropolarimeter designed and built at the Main Astronomical Observatory of the Ukrainian Academy of Sciences for polarimetric investigation of the Moon and the planets. It is known that polarimetry makes it possible to obtain valuable information on the physical nature of celestial objects. Moreover, remarkable relations have recently been discovered between the degree of polarization and other physical characteristics, which are less accessible to measurement. For example, a unique dependence has been found between the degree of polarization of lunar surface features and their absolute reflectivity at full moon [1].

However, the polarimetric instruments available are inconvenient for long runs of observations, require lengthy processing of the direct results of observation to obtain the final data, and give distorted readings for weakly polarized objects. In view of the increasing importance of polarimetry it was found desirable to design a special high-speed accurate recording apparatus answering modern needs. A first instrument of this kind was constructed at Abastumani [2] by L. V. Ksanfomaliti and it immediately demonstrated its advantages over conventional polarimeters. This instrument, however, has complicated circuitry, which makes it difficult to copy by other observatories.

The recording polarimeter designed at Khar'kov [3] has certain advantages in this respect, although there still remain some difficulties involved in the manufacture of certain mechanical units. In particular, imperfection of the perforated disk of the optical modulator may give rise to specious polarization of as much as 1 %.

In designing our device, we freely drew upon the experience of the workers of the Khar'kov Observatory.

Astronomical polarimeters are usually based on the "flicker" principle, also employed in recording polarimeters. The light being studied is received on an analyzer rotated by a synchronous motor at an angular velocity ω . If the incident light is polarized, with degree of polarization P , then upon emerging from the polaroid its brightness will be modulated as

$$I = I_0 [1 + P \cos (2\omega t + 2\Omega)]. \quad (1)$$

Here I_0 is the mean intensity of the transmitted light, Ω the angle between the planes of polarization of the incident light and of the polaroid at the time $t=0$, 2ω the optical frequency of rotation of the analyzer.

The modulated light is directed to a photomultiplier, where it is converted into a proportional electric signal. The signal is amplified by a power amplifier and recorded on a loop oscilloscope or an electronic recording voltmeter.

To fix the plane of polarization, a contact is provided at the rim of the analyzer which briefly breaks the recorder circuit. One such trace is shown in Figure 1.

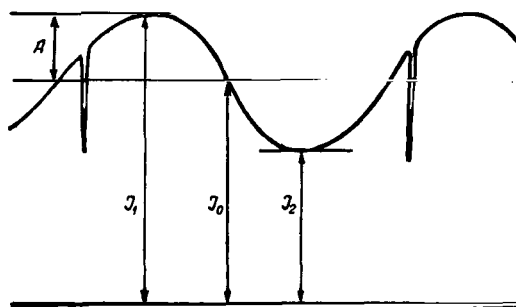


FIGURE 1

The degree of polarization is determined from the trace by taking the ratio

$$\frac{I_1 - I_2}{I_1 + I_2} = \frac{\frac{I_1 - I_2}{2}}{\frac{I_1 + I_2}{2}} = \frac{A}{I_0} = P, \quad (2)$$

where I_1 and I_2 are respectively the maximum and the minimum output signal, I_0 the d. c. component of the signal, A the amplitude of the a. c. component. The plane of polarization is determined from the position of the breaks in the trace relative to the instantaneous zero level of the sine curve. The distance between two successive maxima corresponds to a polarization angle of 180° . In principle, one optical revolution of the analyzer (equal to half a mechanical revolution) suffices to measure the degree and the angle of polarization. However, because of atmospheric turbulence and instrument noise, the time of observation must be extended. The rate of rotation of the analyzer is generally chosen taking into consideration the inertia of the recorder. With a loop oscilloscope, the analyzer may rotate at a rate of several hundred r. p. m. In practice, however, such high rates are undesirable owing to great broadening of the noise frequency spectrum. Moreover, the results of observations become accessible only when the film has been developed. With a recording voltmeter the angular velocity of the analyzer should not exceed a few r. p. m., so that the minimum time of observation is in the neighborhood of one minute.

The main shortcoming of the old polarimetric devices is the necessity for much processing of their output. The automatic recording electropolarimeter enables us to read the degree of polarization and orientation of the plane of polarization directly in the course of observation. The apparatus also gives a rough estimate of the stellar magnitude of the object. The

duration of a measuring cycle depends on the brightness of the object, and varies between 2 and 3 seconds.

The operating principle of the automatic polarimeter is clarified by its block-diagram (Figure 2). The light being studied passes through the rotating analyzer 1 to the FEU-2 cathode. The plate current of the photomultiplier, proportional to the instantaneous luminous intensity, produces a potential difference on the load resistor R , which is measured with a special electrometric amplifier 3. A system of filters provided at the amplifier output separates the constant component of the signal I_0 , which is proportional to the mean brightness of the object, and the harmonic component $A \cos(\omega t + \Omega)$, whose frequency is the optical modulation frequency of the light. The degree of polarization is determined from (2). The d. c. component is compared with a standard voltage source. The difference between them is fed to the input of a system of automatic amplification control AAR 4 which regulates the voltage of the photomultiplier 5. The AAR system is so effective that when the luminous flux increases by a factor of 10^4 , the gain factor of the multiplier drops by a factor of $0.995 \cdot 10^4 \approx 10^4$.

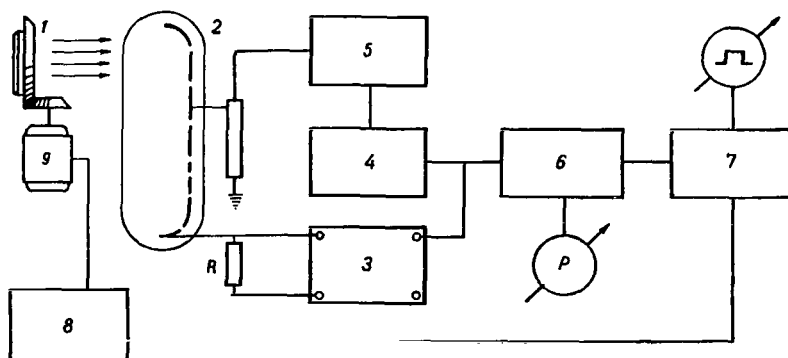


FIGURE 2

Upon such an extreme change (10 stellar magnitudes) in the luminous flux, the d. c. component of the photomultiplier input signal will change by no more than 0.5 %.

Since variation of the multiplier gain factor does not change the ratio $\frac{A}{I_0}$, and I_0 remains virtually constant regardless of the luminous flux (within the limits specified), the scale of the apparatus measuring the amplitude of the harmonic component $A \cos(2\omega t + \Omega)$ can be calibrated directly in percentage polarization.

The a. c. component $A \cos(2\omega t + \Omega)$ is amplified by amplifier 6. The plane of polarization is measured with phase meter 7. The latter measures the phase difference between the a. c. signal and a signal from the generator 8 which drives the synchronous motor 9. The orientation scale of the plane of polarization is calibrated in degrees of arc.

The circuitry of the principal unit of the apparatus is shown in Figure 3.

An EMI 6256 B photomultiplier is used as a radiation detector: spectral sensitivity range, 300–600 $m\mu$. Cathode sensitivity, $70 \mu A/\text{lumen}$, dark

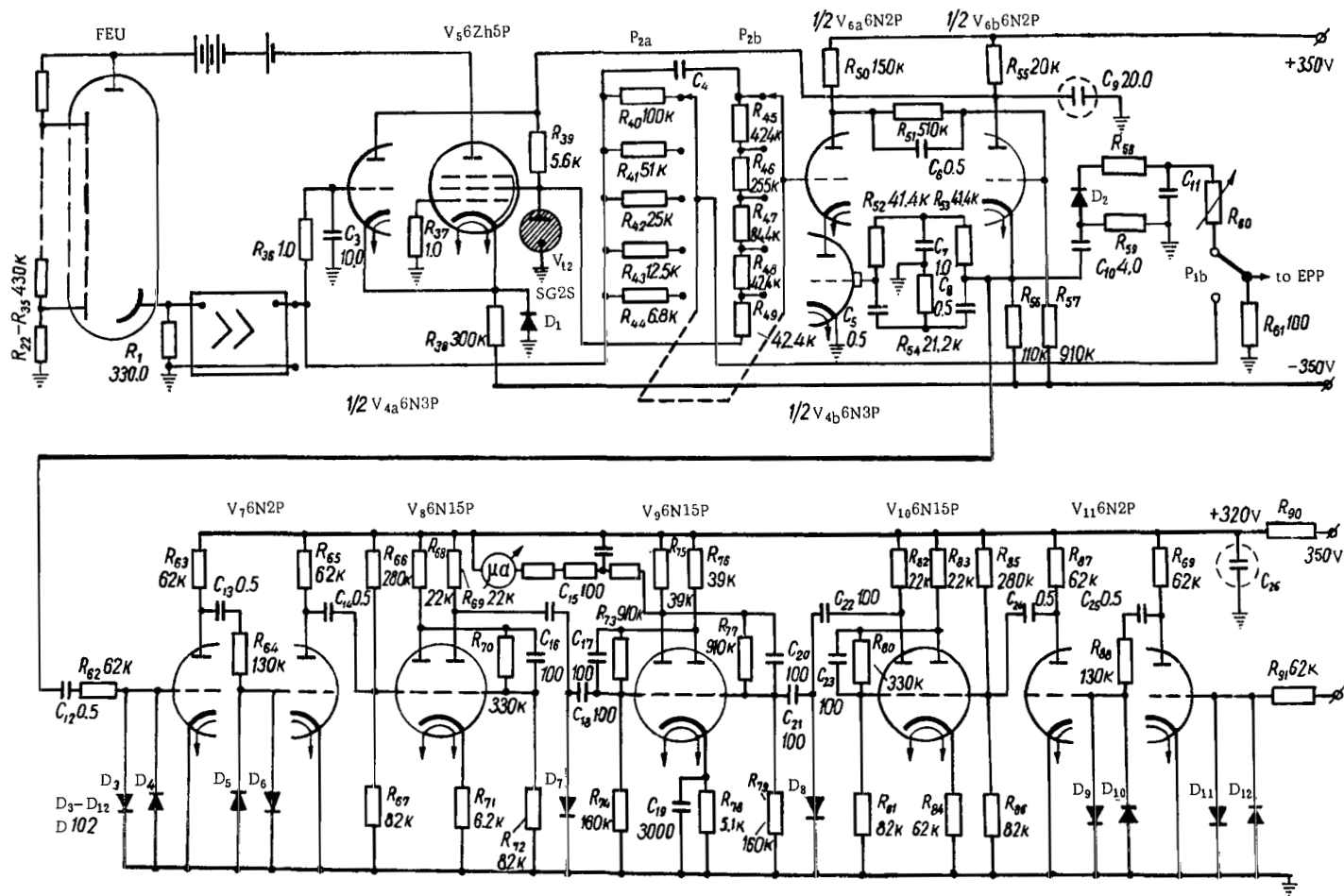


FIGURE 3

current 10^{-9} A with anode sensitivity of 2000 A/lumen and feed voltage of 1650 V.

When no signal is produced by the multiplier, the preamplifier voltage is 75 V. This voltage is taken as the standard potential in the AAR system, and its value is rigidly fixed by appropriately choosing the regime of the amplifier circuit. A signal in the circuit corresponds to an increase of the output voltage of the amplifier. The AAR amplifier is assembled around V_{4a} and V_5 valves which, together with the photomultiplier voltage divider and feed source, constitute a cathode coupling with plate load. The photomultiplier high-voltage source (whose circuit is shown in Figure 7) is conventionally represented as a battery connected with appropriate polarity. The gain factor of the stage is close to 2000 for V_5 grid bias of 1.5–2 V (relative to the cathode) and photomultiplier voltage divider resistance of $5\text{ M}\Omega$. To stabilize the stage regime, the valve is current-regulated by a ballast resistor. The AAR system functions as follows. The valve V_5 connected in series with the photomultiplier voltage divider acts as a variable resistor, whose resistance depends on the grid bias. Before the signal is received, or when the signal is less than the standard voltage, the valve is fully conducting and the entire feed voltage is applied to the photomultiplier divider, which corresponds to maximum multiplier sensitivity. As the luminous flux increases, the input signal rises to the reference level and the resistance of the valve V_5 then starts increasing. The voltage across the photomultiplier divider drops and the gain factor of the amplifier correspondingly decreases. When the output signal exceeds the standard voltage by 0.5 volt, the photomultiplier voltage decreases by 1000 V. The gain factor of the EMI multiplier then drops by a factor of 10^4 . This change of the gain factor occurs if the luminous flux simultaneously increases by a factor of 10^4 (by 10^m). This follows from the fact that the output signal, proportional to the product of the luminous flux and the photomultiplier gain factor, remained constant to within 0.5% (relative to the geometric-mean brightness), which establishes the inverse proportionality between the gain factor and the output signal.

Only the d. c. input signal is fed into the AAR system. The a. c. component is blocked by the integrating circuit $R_{36} C_3$. The time constant of the circuit $\tau \approx 10$ sec. It is generally assumed that transient processes in reactive circuits decay within 5τ . For the AAR system the steadying time also depends on the initial amplitude of the input signal and is always less than 5τ . Indeed, as long as the voltage across the capacitor C_3 is less than the standard voltage (AAR switched off), the capacitor is charged according to

$$u = u_{st} (1 - e^{-\frac{t}{\tau}}),$$

where u_{st} is the photomultiplier signal for a given luminous flux and maximum gain factor. Clearly, the luminous flux should be greater than the threshold flux for the circuit in question. The charging virtually terminates when the voltage on the capacitor C_3 has reached 75 V. All subsequent processes increase the capacitor voltage by no more than 1%. If $\frac{u}{u_{st}} \ll 1$, which is always so in case of initial overamplification and sufficient dynamic range of preamplifier, the transients mostly terminate within $t \approx \frac{u}{u_{st}} \tau$. The dynamic range of the amplifier is 400 volt, whence it follows that the steady

regime is achieved in 2 sec ($\tau_{eq} = 0.4$ sec) virtually for any light flux, which is consistent with the results obtained with the polarimeter. The response time of the circuit to slight changes in light flux, e.g., when investigating polarization over the planetary disk, is somewhat shorter, which is due to the extremely small change of voltage at the AAR input. To prevent overloading of the V_5 grid, a diode D_1 is connected into the circuit, and the grid of the V_5 valve is earthed through the buffer resistor R_{37} . Since the photomultiplier feed source does not touch the housing of the apparatus, the photomultiplier divider may be acted upon by a considerable a. c. emf with a frequency of 50 cps. This is due to the resistance ($\sim 100 \text{ M}\Omega$) of the transformer leakage to the housing. The photomultiplier divider is therefore shunted with a condenser $C_{ph} = 1 \mu\text{F}$. The parasitic modulation of the signal by the 50 cps frequency does not exceed 0.5% and can easily be filtered off. On the other hand, increasing the nominal capacity of C_{ph} lowers the damping of the AAR system and may lead to excitation of the circuit (when the τ of the plate load of the AAR amplifier is comparable with or greater than the τ of the integrating circuit $R_{36}C_3$). The best solution for high-speed devices would apparently be the application of high-frequency voltage converters or dry batteries for feeding the photomultiplier. It is not essential that the high-voltage feed source of the photomultiplier be stabilized, since it is coupled to the circuit through the AAR system.

To measure the degree of polarization, the variable component of the signal is fed from the preamplifier output through a blocking capacitor C_4 and a voltage divider R_{45-49} to the input of a selective amplifier tuned to the optical frequency of polaroid rotation. From various considerations this frequency was taken equal to 37.5 cps. A selective amplifier is used since we must suppress the instrument noise and the turbulent scintillation over a wide frequency band, which lowers the accuracy of measurement. The output indicator of the degree of polarization has five full-scale ranges: 5, 10, 20, 50, and 100%. The scales are switched with the aid of the divider R_{45-49} .

Since the d. c. signal I_0 is equal to 75 volt, the amplitude of the a. c. signal due to a source of light with $P = 100\%$ is equal to 75 volt, by (2). Hence the full output scale corresponds to a 3.75 volt signal ($75 \text{ volt} \times 0.05$) at the input of the selective stage. Application of the diode detector at the stage output makes it impossible to measure signals with an amplitude of less than 0.3 volt, so that the signal must be amplified several times.

When choosing the selective amplifier, the following requirements were taken into consideration. High equivalent Q -factor, $Q_{eq} = \frac{f}{\Delta f}$, where f is the resonance frequency, Δf the transmission band of the amplifier. Negligible drift of the resonance frequency ($\Delta f_{dr} \ll \Delta f$), stable amplification, linear amplitude characteristic in the working range (15–20 volt). The best resonance properties are obtained with a twin T -bridge connected into the negative feedback circuit of the amplifier with an active load. The negative feedback functions at all frequencies, except at resonance, where the transmission factor is zero. With bridge parameters $R_{52} = R_{53} = 2R_{54} = R$ and $C_5 = C_6 = \frac{C_7}{2} = C$, the resonance frequency is obtained from

$$f = \frac{1}{2\pi RC}.$$

The Q -factor is $Q_{eq} = \frac{k_0}{4}$, where k_0 is the gain factor of the amplifier without the feedback. The twin T -bridge will remain stable and highly selective if the output stage resistance is much less than R , while the input resistance is much greater than R . With an ordinary amplifying stage, negligible output resistance is obtained only for low plate load, which precludes high amplification. The signal source moreover by-passes the bridge at the output.

The bridge output is not coupled directly to the output of the selective amplifier assembled around valves V_{4b} , V_{6a} , V_{6b} . The valve V_{6b} acts as a cathode follower and ensures low output resistance of the amplifier. The input gain factor of V_{6a} is close to 4. Stability of amplification is ensured by providing strong current feedback. (The valve V_{4b} is connected as a cathode load of the valve V_{6a} .)

No blocking capacitors are provided in the amplifier. The cathode follower is connected through the divider $R_{51} R_{57}$ with the anode of V_{6a} , and the d. c. transmission factor of the bridge is 1. The valve V_{4b} acts as a feedback amplifier with a gain factor close to 30. The negative d. c. feedback thus stabilizes the amplifier regime. This simultaneously eliminates the necessity for automatic biasing of the valve V_{4b} , which results in high phase shifts at the frequency of 37.5 cps.

The gain factor of the valve V_{4b} relative to the amplifier output (without feedback) is equal to 120, which corresponds to $Q_{eq} = 30$ ($\Delta f = 1.25$ cps). The amplifier is thus linear in the ± 30 volt range. Bridge elements utilize high precision components to ensure stability of the resonance frequency of the amplifier.

The a. c. component is fed from the amplifier output through the blocking circuit $C_{10} R_{59}$ to the diode detector D_2 . The detected signal is averaged by the $R_{68} C_{11}$ circuit with $\tau = 0.5$ sec and is measured by an automatic electronic voltmeter EPP-09 calibrated in percent.

A provision has been made for using the apparatus as an ordinary photometer. The AAR system is then switched off (the anode of the valve V_5 is connected through a special switch to the housing). The EEP-09 recorder is connected through additional resistors $R_{40}-R_{44}$ (P_{2a}) to the preamplifier output (P_{1b}). Null output voltage of the amplifier (P_{1a}) is simultaneously established.

Measurements of the plane of polarization amount to measuring the phase difference between the phase of the polarized component of the signal and the phase of voltage driving the synchronous motor of the modulator. Indeed, the phase of the feed voltage uniquely specifies the position of the plane of polarization of the polaroid relative to the reference plane, which can be easily fixed, e. g., by observing the celestial meridian.

The phase difference is measured with a two-input trigger. A train of short pulses corresponding to the moment of the initial phase of the sine signal of the polarimeter is fed to one input, while the other input receives analogous pulses from reference-pulse generator. If the phase difference is φ , and the current through the freely conducting valve I_0 , then the average current through one trigger triode per period is equal to $I_{av} = I_0 \frac{\varphi}{2\pi}$. The orientation angle of the plane of polarization $\Phi = 2\varphi$ is proportional to I_{av} .

The triggering pulses are generated as follows. The sine wave from the output of the selective amplifier is fed through C_{12} to the bilateral limiter

$R_{62} D_3 D_4$. The diodes can be connected in this way, since their forward conductivity in the voltage range from 0 to +0.2 is still negligible.

The resistance of the $D_3 D_4$ circuit in the neighborhood of the null potential is much greater than R_{62} , sharply dropping for signals greater than 0.2 volt in absolute magnitude. Only silicon diodes have this property. If the signal amplitude is sufficiently large, the diode voltage will be close to a square wave. To increase the front steepness, the signal received, after amplification by the left triode of V_7 , is reshaped by the $R_{64} D_5 D_6$ circuit and is fed through an amplifier (the right triode of V_7) to the stage V_8 which shapes a strictly square signal. The stage is assembled as a trigger with cathode coupling. The left triode is normally cut off. The circuit switches into another stable state when a positive signal is fed to the stage input. Back switching occurs when the control signal drops below the forward triggering threshold. The difference of triggering thresholds is equal to 2–3 volts. The initial grid bias of the left triode is established by selecting the resistor R_{67} ; it is equal to the average value of the biases for forward and back switching. The square signal is fed from the resistor R_{69} to the differentiating circuit $C_{15} D_7$; pulses of positive polarity are blocked by the diode. The resulting signals correspond to the transition of the input sine signal through zero and are fed as triggering pulses to one of the inputs of the measuring trigger (valve V_9). The other input receives pulses

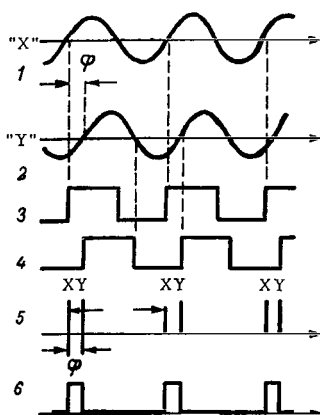


FIGURE 4

similarly shaped from the signal of the reference generator (V_{11} , V_{10}). A microammeter, whose scale reads the angle of polarization in degrees, is coupled in parallel to the plate load of one of the trigger triodes.

The voltage diagram in Figure 4 illustrates how the phase meter functions. Here 1, 2 are input signals of the polarimeter "X" and of the reference generator "Y" with a phase difference φ ; 3, 4 are the corresponding square pulses; 5—pulses formed from the square pulses; 6—trigger anode voltage. The phase meter is calibrated by successively switching off the input signals. The meter readings then correspond to 0 or 180°.

One of the most critical units in the polarimeter is the electrometric amplifier.

It should have a high current-gain factor with a transmission band of up to 200 cycles. The amplifier must be linear in a wide dynamic range of input voltages. It suffices to say that the total amplitude of the signal generated by the 100% polarized signal used in calibration is 150 volt. The null drift should not exceed tenths of a percent of the reference signal; otherwise the polarization measurement will be distorted. The requirements are met by the amplifier whose circuit is shown in Figure 5. The first stage is an electrometric valve, which makes it possible to operate with the high multiplier load resistances. A switch is provided (not shown in the figure) for varying the input resistance from $3 \cdot 10^5$ to $10^{10} \Omega$. The 330 M Ω resistance shown in the figure is generally used in polarization measurements. The second amplifier stage has a high

gain factor ($k = 60$) and acts as a coupling link between the electrometric valve and the output stage.

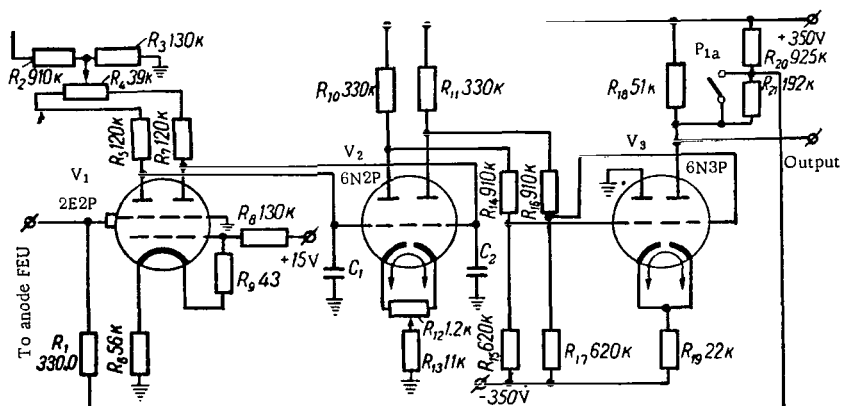


FIGURE 5

The first two stages are assembled on parallel-balance bridge and give a symmetric output. The output stage introduces a bias and has a gain factor close to 10 (taking into consideration the dividers $R_{14} R_{15}$ and $R_{16} R_{17}$). The amplifier is governed by rigid negative feedback. When the device is used as a polarimeter $\beta = 0.84$, and when as a photometer $\beta = 1$. The gain factor of the amplifier with feedback is

$$k = \frac{k_0}{1 + \beta k_0},$$

where k_0 is the gain factor without feedback ($k_0 = 600$). Since $k_0 \beta \gg 1$, we have $k = \frac{1}{\beta}$, equal to 1.2 and 1 for the polarimeter and the photometer, respectively. The divider $R_{20} R_{21}$ is used to set up the initial amplifier voltage (75 volt) in the polarimeter. To prevent high-frequency excitation of the amplifier, antioscillatory elements C_1, C_2 are provided in the grids of the second stage. Their strength is chosen while tuning the apparatus. The potentiometers R_4 and R_{12} are required for balancing the circuit in laboratory tuning. The amplifier drift is not greater than 20 mV, both while working with the device and while switching on repeatedly. The amplifier is linear in the input voltage range from -100 to $+250$ volt. The negative feedback substantially broadens the transmission band of the amplifier and makes it possible to obtain high input resistance in the desired frequency band. Here, although no voltage amplification occurs, the current gain factor is as high as 10^7 .

An analogous d. c. amplifier was used in a photometric investigation of Mars [4], where it demonstrated its good operational properties.

The measuring circuits of the polarimeter are fed from four stabilized voltage sources of $+350$, -350 , -2000 , and $+15$ volt. The ± 350 volt stabilizers are identical and differ only in the earthed terminal. The circuit is shown in Figure 6. The stabilization factor is of the order of 10^3 .

Output resistance for $I_{\max}=100$ mA not greater than 0.2 ohm. Variation of output voltage of the stabilizer circuit is mainly due to the drift of the working voltage of the SG4S stabilizer.

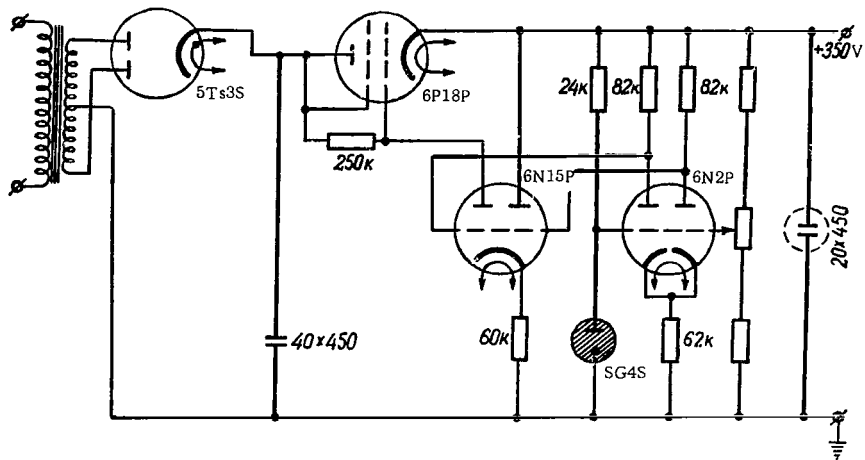


FIGURE 6

The high-voltage stabilizer (Figure 7) is assembled as a separate unit and is used in other photoelectric work. To increase the stabilization factor, the regulating valve (6Zh5P) was used in pentode coupling. (Screen

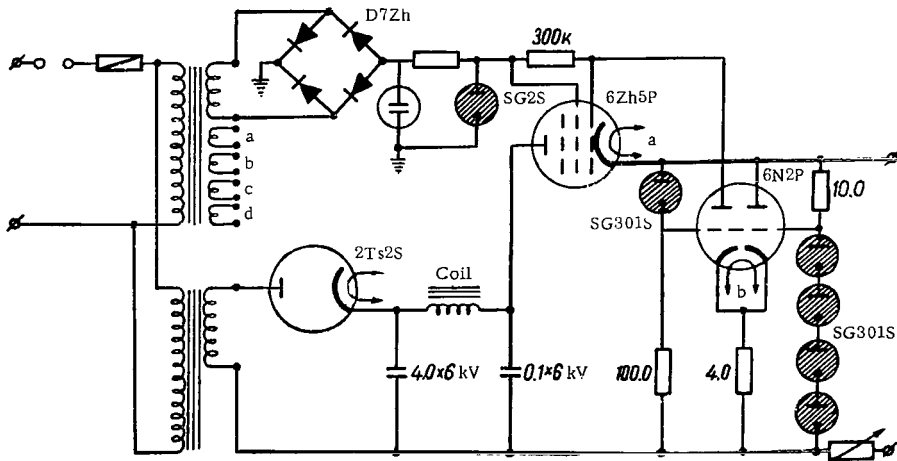


FIGURE 7

grid fed from a special stabilized source.) The total instability of the output voltage does not exceed 0.05 %.

The 15-volt source was stabilized with a semiconductor stabilizer (Figure 8) intended for feeding the circuits of the electrometric valve 2E2P. Stabilization factor, close to 30.

The apparatus described makes it possible to obtain reliable recording of 0.1–0.2 % polarization. The threshold stellar magnitude sensed by the polarimeter depends on the degree of polarization of the source. For a

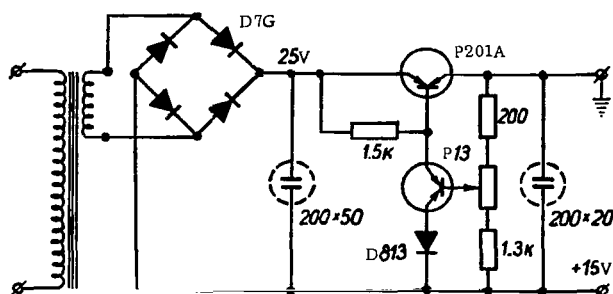


FIGURE 8

source with $P = 1\%$, the device will register a 10st object. The absolute error of measurements does not exceed 1 % in the scale employed for low polarizations and 0.5 % for high polarizations. The orientation of the plane of polarization is measured to within $\pm 0^\circ.5$.

The polarimeter was used in a long series of polarimetric observations of Mars with light filters. The results are given in this volume /5/.

REFERENCES

1. AVRAMCHUK, V. V.— This volume.
2. KSANFOMALITI, L. V.— Trudy Astronomicheskoi Observatorii KhGU, 14: 91, 1962.
3. DUDINOV, V. I. and O. I. BUGAENKO.— Trudy Astronomicheskoi Observatorii KhGU, 14: 100, 1962.
4. BUGAENKO, L. A. et al.— This volume.
5. MOROZHENKO, A. V.— This volume.

A. A. Demenko

TYPES OF COMETARY TAILS

The mechanical theory of cometary tails as laid down by F. A. Bredikhin, is based on the following two assumptions /1/:

1. Cometary tails consist of material particles impelled by forces of solar origin. In addition to Newtonian attraction, these particles are also repelled by the sun; the magnitude of these forces is inversely proportional to the square of the distance of the particles from the Sun.

2. Each individual particle of a cometary tail is acted upon by a characteristic force of repulsion whose magnitude varies only with the distance of the particle from the sun.

According to Assumption 1, the effect of the cometary nucleus on the motion of the tail particles, which is felt in the immediate vicinity of the nucleus only, is neglected. Studying the solar repulsion accelerations in cometary tails, F. A. Bredikhin in 1877 put forward the proposition that several types of cometary tails exist, depending on the mean magnitude of the solar repulsive acceleration /1/.

In 1878, F. A. Bredikhin laid down a classification of cometary forms. According to this classification, three types of cometary tails exist; they differ in mean solar repulsion accelerations $1+\mu$ (expressed in units of Newtonian attraction).

1. Type I tails, generally of irregular outline, situated close to the projection of the continuation of the radius-vector of the nucleus. Long, curving almost imperceptibly in a direction opposite to the motion of the comet. Well-developed tails show numerous streaks and ray systems of complex structure. These tails often include cloudy formations moving with tremendous velocities within the tail. A poorly developed type I tail appears as a faintly outlined luminous band parallel to the radius-vector. Type I tails have

$$1+\mu > 5.$$

2. Type II tails are characterized by accelerations of from 2.5 to 0.5; these tails curve greatly and veer from the radius-vector in the direction opposite to the motion of the comet. Near the head these tails are distinctly outlined, but as we move farther off the contour becomes blurred; in some large comets, the tails were observed to break into straight bands directed to the cometary nucleus; these formations were called by Bredikhin *synchrones*.

According to S. K. Vsekhsvyatskii, *synchrones* in type II tails are not swarms of particles "simultaneously" ejected from the cometary nucleus, but are of electromagnetic origin, tracing out the magnetic force lines in interplanetary space /2/.

3. In type III tails, $1+\mu$ ranges from 0 to 0.3. These tails sharply bend away from the radius-vector of the comet in the direction opposite to its motion; the tail issues directly from the head of the comet and is often straight. These tails can be regarded as synchronous formations.

Anomalous tails were treated by F. A. Bredikhin as a separate class.

4. Anomalous tails point toward the sun, generally leading the radius-vector of the comet. According to Bredikhin, anomalous tails form as follows: the particles flowing from the nucleus to form the normal tail entrain massive conerations which acquire initial sunward velocities. The force of repulsion acting on these particles is negligible, and they are accelerated by Newtonian attraction alone. Anomalous tails were investigated by S. K. Vsekhsvyatskii [3].

The geometric elements of cometary tails were taken by Bredikhin as syndynames and synchrones. A syndyname is a locus of idealized particles escaping from the sphere of the nucleus at different times, but under identical initial conditions, having all the same acceleration.

The set of all syndynames constitutes an ideal tail—the syndyname conoid.

A synchrone is a locus of idealized particles escaping at the same time, but having different $1+\mu$.

Since 1884, Bredikhin's classification has been repeatedly revised. In particular, in 1942, in the last classification of S. V. Orlov, type II and III tails are treated as subclasses of one type. S. V. Orlov maintained that types II and III consist of dust, in distinction from the tails of type I, which are gaseous. This arbitrary revision of the classification, reflecting current views on the nature of cometary tails, is in no way manifested in mechanical differences. Bredikhin's classification is apparently the most acceptable. The Moscow school (S. V. Orlov and others) classified or revised the classification of tails for 35 comets prior to 1930. No systematic classification of cometary tails was attempted after 1940. On the other hand, this classification is of unquestionable interest, since neither the reasons for the appearance of the different types of tails nor the mechanism of tail formation have ever been really classified. The entire available material must be reviewed and the results should be compiled into one comprehensive catalog.

The aim of this work was the compilation of a catalog of cometary tails. A cometary tail can be classified only after the apparent tail projections have been combined into projections on the comet's orbital plane. The apparent forms of tails in the sky must correspond to the actual forms, since the Earth may be variously positioned relative to the plane of the cometary orbit. This orientation is specified by the angle S between the celestial sphere and the plane of the cometary orbit, or, equivalently, by the angle between the line of sight and the perpendicular to the plane of the cometary orbit. If this angle is close to 90° , all tails are projected into a single band and there is no way to determine the tail curvature. If S is in the intervals $0^\circ < S < 85^\circ$ and $95^\circ < S < 180^\circ$, it is possible to determine the type of the tail. To determine the reliability of the projection, we must establish the apparent angle between the axes of the cometocentric coordinates $\xi'O\eta'$ [4]. The cometary tail can be effectively classified if this angle is greater than 20° . The greater the angle, the higher the reliability of the projection.

Bredikhin determined the types of cometary tails by the following technique: the points of the median line of the tail are projected onto the plane of the cometary orbit; then, using the exact formulas of hyperbolic motion /1/, the syndynames corresponding to various values of $1+\mu$ are calculated. The aim of the calculation is to determine the particular value of $1+\mu$ for which the curvature of the syndyname fits the median line of the tail.

This technique was applied in our work to the classification of cometary tails.

The syndynames of comets with large tails cannot be calculated from approximate formulas owing to the time elapsed since ejection of the particles from the nucleus. To determine the type of the tail, we must have a photograph or an accurate drawing of the tail against the field of the stars.

S. V. Orlov suggested that the cometary tail be drawn on the celestial map and the median line of the tail be then determined /4/. This involves inevitable errors. To improve the accuracy, we acted as follows: an epidiascope was used to project comet photographs with 20-30-fold magnification on a screen, and the stellar field and the cometary tail were traced on the screen. The celestial map was projected onto the same screen, the magnification being chosen so as to ensure coincidence of the corresponding stars; the coordinate mesh of the map was then drawn on the screen. It was thus possible to trace the median line of the tail quite accurately. Most comets have poorly developed tails. In this case our method cannot be applied, because the tail is too short. These tails are classified by utilizing the fact that the axis of type I tail projected on the orbital plane parallels the radius-vector. The axis of a type II tail, even near the head, noticeably departs from the prolonged radius-vector in a direction opposite to the comet's motion. The axes of type III tails depart from the prolonged radius-vector even more: these are possibly straight synchrones issuing from the cometary head.

As for large comets, an epidiascope was used to project images of the cometary tail and of the stellar field magnified to the same scale; the celestial coordinate mesh was then traced. The visibility conditions [parameters] of the comet were then calculated. If they were satisfactory, the calculated angle $\xi_0\eta'$, at which the rectangular cometocentric coordinates $\xi_0\eta$ are viewed from the Earth, was marked on the celestial map on the screen, with the origin placed at the comet head. In classifying the tail, we took into consideration its structure, physical peculiarities, and spectral characteristics, if known. In doubtful cases the syndynames were computed and then plotted on the same celestial map using the projection formulas /4, 6, 7/.

Tails of 112 comets were classified in this way. In addition to these comets, we included in the catalog those whose tail types had been determined by F. A. Bredikhin, S. V. Orlov, B. A. Vorontsov-Vel'yaminov, and others.

In our catalog we use the notation of S. K. Vsekhsvyatskii in his "Physical Characteristics of Comets" /8/. The maximum tail lengths are also borrowed from this book.

Catalog of cometary tails

[illegible]

* Classification uncertain

** First number identifies the source in the bibliography, the second gives the page.

Catalog of cometary tails (continued)

No.	Designation in Vsekhsvyatskii's catalog /8/	Old designation	Type of tail	Apparent l° and calcu- lated s (in A.U.) maximum tail length		Source
				l°	s	
35	1844 III	1844 c	II, III anom.	8		F.A. Bredikhin /10, 65/ A.A. Belopol'skii /9, 65/ S.K. Vsekhsvyatskii /3, 167/
36	1853 II	1853 b	III	10	0,02	F.A. Bredikhin /9, 37/
37	1853 III	1853 e	I, III	12	0,18	F.A. Bredikhin /23, 68-72/
38	1853 IV	1853 d	III	3°50'	0,05	F.A. Bredikhin /9, 37/
39	1854 II	1854 b	I, III	5	0,08	F.A. Bredikhin /21, 37/
40	1854 III	1854 c	II	1,5	0,03	F.A. Bredikhin /9, 38/
41	1857 III	1857 c	III	0,5	0,01	F.A. Bredikhin /21, 38/
42	1858 VI	1858 c	II, I	40	0,55	F.A. Bredikhin /15, 100-110/ /20, 104/
43	1860 III	1860 c	II	20	0,28	F.A. Bredikhin /9, 38/ /14, 79/
44	1861 II	1861 b	I, II	90	0,34	F.A. Bredikhin /16, 75-76/ /17, 203-205, 375-376/ Yu. V. Filippov /18, 202/
45	1862 III	1862 b	I, III anom.	25	0,17	F.A. Bredikhin /19, 17/ S.K. Vsekhsvyatskii /3, 166/
46	1865 I	1865 a	II, III	25	0,45	F.A. Bredikhin /20, 48/
47	1867 III	1867 c	I	0,25	0,004	The author
48	1868 II	1868 b	I	3	0,02	" "
49	1869 I	1869 a	anom. ejection		0,0005	" "
50	1870 I	1870 a	I	0,(3)	0,008	" "
51	1874 III	1874 c	I, II	36	0,29	F.A. Bredikhin /10, 39/
52	1877 II	1877 b	I, III anom.	2,6	0,05	F.A. Bredikhin /9, 41/ S.K. Vsekhsvyatskii /3, 174/ The author
53	1877 V	1877 f	I	5'	0,002	The author
54	1880 I	1880 a	II	50	1,0	F.A. Bredikhin /11, 58/
55	1881 III	1881 b	II, I	14	0,15	F.A. Bredikhin /13, 57-71/
56	1881 IV	1881 c	I, II	10	0,24	F.A. Bredikhin /13, 171/
57	1882 I	1882 b	II, III, I	5	0,94	F.A. Bredikhin /22, 24/
58	1882 II	1882 d	I, II, III, anom.	30	1,25	F.A. Bredikhin /7, 358/ /24, 129/ /25, 48/ T.V. Vodop'yanova /26, 187/
59	1883 I	1883 a	I, II	1	0,023 0,002	The author " "
60	1884 I	1883 b	I, II	20	0,25	F.A. Bredikhin /17, 374/ /27, 97-110/ (T. Bruhns) /28, 121/
61	1885 II	1885 b	III	4'	0,002	The author
62	1886 I	1885 f	II	6	0,07	F.A. Bredikhin /29, 4/
63	1886 II	1885 g	II or I, anom.	2,5		F.A. Bredikhin /30, 5/ (T. Bruhns) /31, 311/ S.K. Vsekhsvyatskii /3, 166/
64	1886 IX	1886 f	I, II, III	7°20'	0,19; 0,02	F.A. Bredikhin /32, 7/
65	1887 I	1887 a	III	41	0,35	F.A. Bredikhin /32, 29/
66	1889 I	1888 c	III	0,5	0,03	F.A. Bredikhin /33, 164/
67	1892 I	1892 a	I	4	0,56	B.A. Vorontsov-Vel'yaminov /34, 36/
68	1892 III	1892 h	I	0,5	0,13	F.A. Bredikhin /35, 539/ S.V. Orlov /36, 8/

Catalog of cometary tails (continued)

No.	Designation in Vsekhsvyatskii's catalog /8/	Old designation	Type of tail	Apparent l° and calcu- lated s (in A.U.) maximum tail length		Source
				l°	s	
69	1893 II	1893 a, c	I	18	0.25	F. A. Bredikhin /37/ Hussey /38/
70	1893 IV	1893 d	I, II	3.5	0.82	F. A. Bredikhin /17, 220, 422/ /37/, /39, 541/ B. A. Vorontsov-Vel'yaminov /40, 90/ Kopff /41, 213/ F. A. Bredikhin /17, 391/ F. A. Bredikhin /42, 501/ T. V. Vodop'yanova /26, 187/ F. A. Bredikhin /43, 451/ /44, 219/ N. D. Moiseev /45, 73/ S. V. Orlov /4/ G. Jaegermann /46, 279/ Kopff /47, 149/ S. V. Orlov /48/ T. V. Vodop'yanova /49, 177/ K. D. Pokrovskii /50, 233/ The author Kopff /51/ S. V. Orlov /52//63, 73//64, 193/ A. Ya. Orlov /53/ K. D. Pokrovskii /54, 3/ Eddington /55/ Carrington /56/ K. D. Pokrovskii /57/. /58/ S. K. Vsekhsvyatskii /3, 171/ I. F. Polak /59, 3/ S. K. Vsekhsvyatskii /60, 77/ N. Bobrovnikoff /61/ The author S. V. Orlov /62/ S. K. Vsekhsvyatskii /60, 13/ The author
71	1894 II	1894 b	II, III	6	0.035	
72	1899 I	1899 a	I, III		0.12	
73	1901 I	1901 a	I, II, III	30	0.26 0.48	
74	1903 IV	1903 c	I, III	17	0.08 0.014	
75	1905 V	1905 b	I	1.5	0.0097	
76	1907 IV	1907 d	I	17	0.22	
77	1908 III	1908 c	I	11	0.19	
78	1910 I	1910 a	II, III, I anom.	10	0.50	
79	1910 II	1909 c	I, II	27	1.5	
80	1911 II	1911 b	I	3	0.05	
81	1911 V	1911 c	I	30	0.4	
82	1912 II	1912 a	I, III	4*; 1.5	0.12 0.03	
83	1913 II	1913 c	III*	4'	0.007	" "
84	1913 IV	1913 b	I	4'	0.002	" "
85	1913 V	1913 e	I	30*	0.005	" "
86	1913 VI	1913 d	I	3.5	0.1	" "
87	1914 I	1914 b	I, III	1	0.126	" "
88	1914 II	1914 a	I	40'	0.017	" "
89	1914 V	1913 f	II, I	10; 4	0.68 0.32	S. V. Orlov /63, 72/ The author
90	1917 I	1917 a	I	2.5	0.11	" "
91	1917 III	1916 b	I	2'	0.001	" "
92	1918 V	1918 b	I		0.0004	" "
93	1919 III	1919 b	I			" "
94	1921 II	1921 a	I, III	17; 0.5	0.034 0.006	" "
95	1921 III	1921 b	anom. ejection		0.00017	" "
96	1922 II	1922 c	II, anom.	20'	0.0016 0.011	" "

Catalog of cometary tails (continued)

No.	Designation in Vsekhsvyatskii's catalog /8/	Old designation	Type of tail	Apparent l° and calcu- lated s (in A.U.) maximum tail length		Source
				l°	s	
97	1924 II	1924 c	I and III	4	0,11	The author
98	1924 III	1924 b	I, anom. ejection	20'	0,006	Yu. V. Filippov /65, 66/ The author
99	1925 I	1925 c	I, III, II		0,026 0,007 0,009	B. A. Vorontsov-Vel'yaminov /66, 57/
100	1925 III	1925 b	I	10'	0,40	B. A. Vorontsov-Vel'yaminov /66, 55/
101	1925 VII	1926 j	III	2	0,054	B. A. Vorontsov-Vel'yaminov /66, 59/
102	1925 IX	1925 g	I	1'	0,0005	The author
103	1925 XI	1925 d	I, anom.	17'	0,018	" "
104	1926 III	1925 d	III	1	0,03	B. A. Vorontsov-Vel'yaminov /66, 61/ B. A. Vorontsov-Vel'yaminov /66, 63/ The author
105	1926 VI	1926 e	I, III	1'		" "
106	1927 III	1926 f	Poss. incip. II *	2'		" "
107	1927 IV	1927 d	I, III	10'	0,03	" "
108	1927 IX	1927 k	II	35	0,61	B. A. Vorontsov-Vel'yaminov /67, 293/
109	1929 I	1929 a	I doubt.	1'	0,001	The author
110	1929 II	1929 c	III		0,0003	" "
111	1930 I	1930 a	incip. I sun- ward ejection		0,0002	" "
112	1930 II	1929 d	I, anom.	2	0,003	B. A. Vorontsov-Vel'yaminov /68, 229/
113	1930 III	1930 c	I	1	0,066	The author
114	1930 V	1930 e	II	3'	0,0008	" "
115	1930 VI	1930 d	I, anom.	30'; 15'	0,0017 0,0008	" "
116	1930 VIII	1930 f	anom.	2'	0,001	" "
117	1931 III	1931 b	I, anom.		0,041	" "
118	1931 IV	1931 c	anom.	2	0,031	" "
119	1932 V	1932 k	I	2	0,031	P. G. Kulikovskii /69, 497/ The author
120	1932 VI	1932 g	III		0,022	" "
121	1932 VII	1932 f	anom.	2'	0,0014	" "
122	1933 II	1933 b	anom. ejection		0,0002	" "
123	1933 V	1933 f	I			" "
124	1933 III	1933 c	I	5'	0,002	" "
125	1934 III	1934 a	I	3'	0,0012	" "
126	1935 I	1935 a	I	35'	0,0100	" "
127	1935 II	1934 b	III *	2'	0,0007	" "

Catalog of cometary tails (continued)

No.	Designation in Vsekhsvyatskii's catalog /8/	Old designation	Type of tail	Apparent l^* and calcu- lated s (in A.U.) maximum tail length		Source
				l^*	s	
128	1935 III	1934 c	III or anom.	3'	0.0006	The author
129	1935 IV	1935 c	I	10'	0.012	" "
130	1936 II	1936 a	I, II	5	0.056	" "
131	1937 II	1937 c	I	0.5	0.014	" "
132	1937 IV	1937 b	III	20'	0.008	" "
133	1937 V	1937 f	I, III anom.	20	0.195 0.0048	" "
134	1937 VI	1937 h	sunward pro- trusion		0.0006	" "
135	1939 III	1939 d	I	20	0.24	K. A. Voroshilov /70, 557/ The author
136	1939 IV	1939 b	I	1'	0.0004	" "
137	1939 VII	1939 g	I	2'	0.0006	" "
138		1939 h	anom. protru- sion			" "
139	1941 I	1940 c	I, II	20; 1	0.20; 0.012	" "
140	1941 IV	1941 c	I, II	7	0.10	" "
141	1941 VIII	1941 d	I, III	1	0.018	" "
142	1942 III	1942 e	anom.	1'	0.0004	" "
143	1942 IV	1942 a	II		0.014	" "
144	1943 I	1942 g	I	17	0.29	" "
145	1946 I	1946 a	II, I	35', 15'	0.011 0.004	" "
146	1946 III	1946 b	III	2'	0.0004	" "
147	1946 V	1946 c	I	25'	0.0027	" "
148	1946 VI	1946 h	II	1'		" "
149	1947 IV	1947 b	I	50'	0.067	" "
150	1947 IX	1947 f	I	4'	0.002	" "
151	1947 XII	1947 n	I	25	0.36	" "
152	1948 I	1947 k	I, III	5; 1	0.09 0.014	" "
153	1948 III	1948 j	III	10'	0.035	" "
154	1948 IV	1948 g	I, III	3; 10'	0.046 0.0015	" "
155	1948 V	1948 d	II	30'	0.039	" "
156	1948 IX	1948 i	I	10'	0.01	" "
157	1948 XII	1948 n	anom.		0.0006	" "
158		1948 h	anom. protrusion			" "
159	1949 IV	1949 c	I	4'	0.007	" "
160	1950 II	1950 a	anom.*		0.0005	" "
161	1950 V	1950 d	III	1'	0.0004	" "
162	1950 VII	1951 b	III	1'	0.0002	" "
163	1951 VIII	1951 d	III	5'	0.0035	" "
164	1951 X	1951 j	I	2'	0.0008	" "
165	1952 III	1951 l	II	2	0.011	" "
166	1953 V	1953 b	I	1'		" "
167	1954 X	1953 g	I, III	35'; 5'		" "

REFERENCES

1. BREDIKHIN, F.A. O khvostakh komet (On Cometary Tails). Moskva-Leningrad, 1934.
2. VSEKHSVYATSKII, S.K.—AZh, Vol.36, 1959.
3. VSEKHSVYATSKII, S.K.—AZh, Vol.9, Nos. 3-4, 1932.
4. ORLOV, S.Ya. Komety (Comets).—ONTI, Moskva, 1935.
5. JOUCOVSKY, N.E.—Ann. Mosc. Obs., Vol.X, No.2, 1884.
6. VSEKHSVYATSKII, S.K.—AZh, Vol.6, 1929.
7. MOISEEV, N.D.—AZh, Vol.1, 1924.
8. VSEKHSVYATSKII, S.K. Fizicheskie kharakteristiki komet (Physical Characteristics of Comets).—Fizmatgiz, Moskva, 1958. [English translation by the Israel Program for Scientific Translations, Jerusalem, 1964. OTS 62-11031.]
9. BREDIKHIN, F.A.—Ann. Mosc. Obs., Series 2, Vol.I, No.1, 1886.
10. BREDIKHIN, F.A.—Ann. Mosc. Obs., Vol.V, No.2, 1879.
11. BREDIKHIN, F.A.—Ann. Mosc. Obs., Vol.VII, No.1, 1880.
12. BREDIKHIN, F.A.—Ann. Mosc. Obs., Vol.VII, No.2, 1881.
13. BREDIKHIN, F.A.—Ann. Mosc. Obs., Vol.VIII, No.1, 1882.
14. BREDIKHIN, F.A.—Ann. Mosc. Obs., Vol.V, No.1, 1878.
15. BREDIKHIN, F.A.—Ann. Mosc. Obs., Vol.X, No.1, 1884.
16. BREDIKHIN, F.A.—Ann. Mosc. Obs., Vol.IV, No.1, 1878.
17. JAEGERMANN, G. Bredichin's mechanische Untersuchungen über Kometenformen, 1903.
18. FILIPPOV, Yu.V.—AZh, Vol.4, No.3, 1927.
19. BREDIKHIN, V.A.—Ann. Mosc. Obs., Vol.III, No.1, 1877.
20. BREDIKHIN, F.A.—Ann. Mosc. Obs., Vol.VI, No.1, 1879.
21. BREDIKHIN, F.A.—Ann. Mosc. Obs., Series 2, Vol.V, No.1, 1886.
22. BREDIKHIN, F.A.—Ann. Mosc. Obs., Vol.IX, No.1, 1883.
23. BREDIKHIN, F.A.—Ann. Mosc. Obs., Vol.V, No.2, 1878.
24. BREDIKHIN, F.A.—AN, Vol.105, 1883.
25. BREDIKHIN, F.A.—Ann. Mosc. Obs., Vol.IX, No.2, 1883.
26. VODOP'YANOVA, T.V.—AZh, Vol.10, No.2, 1933.
27. BREDIKHIN, F.A.—Ann. Mosc. Obs., Vol.X, No.2, 1884.
28. BRUHNS, T.—AN, Vol.122, 1889.
29. BREDIKHIN, F.A.—Ann. Mosc. Obs., Vol.V, No.2, 1888.
30. BREDIKHIN, F.A.—Ann. Mosc. Obs., Vol.I, No.2, 1888.
31. BRUHNS, T.—AN, Vol.123, 1890.
32. BREDIKHIN, F.A.—Ann. Mosc. Obs., Vol.II, No.2, 1888.
33. BREDIKHIN, F.A.—Ann. Mosc. Obs., Series 2, Vol.II, Nos. 1-2, 1890.
34. VORONTOV-VEL'YAMINOV, B.A.—AZh, Vol.4, No.1, 1927.
35. BREDIKHIN, F.A.—Bull. Acad. Pet., Vol.7, 1894.
36. ORLOV, S.V.—AZh, Vol.17, No.1, 1940.
37. BREDIKHIN, F.A.—Izv. AN, No.5, 1895.

\$ 4,00